VERLAG DER TECHNISCHEN UNIVERSITÄT GRAZ

Ishan Gupta

Modelling Growth and Formation of Thrombus: A Multiphasic Approach

CES 45

MONOGRAPHIC SERIES TU GRAZ
COMPUTATION IN ENGINEERING AND SCIENCE

Ishan Gupta

Modelling Growth and Formation of Thrombus: A Multiphasic Approach

Monographic Series TU Graz

Computation in Engineering and Science

Series Editors

Monographic Series TU Graz

Computation in Engineering and Science **Volume 45**

Ishan Gupta

Modelling Growth and Formation of Thrombus: A Multiphasic Approach

---

This work is based on the dissertation *"Modelling Growth and Formation of Thrombus: A Multiphasic Approach"*, presented at Graz University of Technology, Institute of Applied Mechanics in 2023.

Supervision / Assessment:

Martin Schanz (Graz University of Technology)
Bernd Markert (RWTH Aachen University)
Tim Ricken (University of Stuttgart)

Cover	Verlag der Technischen Universität Graz
Cover photo	Vier-Spezies-Rechenmaschine by courtesy of the Gottfried Wilhelm Leibniz Bibliothek Niedersächsische Landesbibliothek Hannover
Print	Buchschmiede (Dataform Media GmbH)

2023 Verlag der Technischen Universität Graz
www.tugraz-verlag.at

Print
ISBN 978-3-85125-964-3

E-Book
ISBN 978-3-85125-965-0
DOI 10.3217/978-3-85125-964-3

Abstract

Aortic Dissection (AD) has a high mortality rate. About 40% of the people with type B AD do not live for more than a month. Aortic Dissection begins when a tear occurs in the inner layer (intima) of the aortic wall. Moreover, a second blood-filled channel called a false lumen is created where thrombosis occurs. The prognosis of AD is quite challenging. Hence, we present a computational model for the formation and growth of thrombus. Because of the complex nature of biological systems, we use a macroscopic continuum-mechanical approach of the Theory of Porous Media.

The whole aggregate is divided into solid, liquid and nutrient constituents. The constituents are assumed to be materially incompressible and isothermal, and the whole aggregate is assumed to be fully saturated. Darcy's law describes the flow of fluid in the porous media. The volume fractions quantify the constituents. Therefore, the regions with thrombus formation are determined using the solid volume fraction. The balance equations of the constituents have coupling terms, which are responsible for the mass exchange and interactions between the phases. These terms play a crucial role in modelling the formation and growth of the thrombus.

We introduce the set of equations and numerical examples for thrombosis in type B AD. The equations are implemented in PANDAS, a finite element package designed to solve strongly coupled multiphase porous media problems. However, the problem description is quite complex due to the difficulty in quantitatively obtaining the data for biological processes and no possibility of performing experiments on living tissues. Therefore, we present computationally less expensive biphasic and more realistic triphasic models using an idealised 2d geometry. The simulations show that the thrombus grows in the low-velocity regions of the blood. Here we study the effects of different parameters and choose reasonable parameters for the thrombus growth in the false lumen. Thereafter, we use a realistic 2d geometry of false lumen to simulate thrombosis and present the model's usefulness in actual cases. The proposed model provides a reasonable approach for the numerical simulation of thrombosis.

Zusammenfassung

Die Aortendissektion (AD) hat eine hohe Sterblichkeitsrate. Etwa 40% der Menschen mit AD vom Typ B leben nicht länger als einen Monat. Eine Aortendissektion beginnt, wenn ein Riss in der inneren Schicht der Aortenwand (Intima) auftritt. Außerdem entsteht ein zweiter blutgefüllter Kanal, das so genannte 'false lumen', in dem sich eine Thrombose bildet. Die Prognose von AD ist sehr schwierig. Daher stellen wir ein Computermodell vor welches die Bildung und das Wachstum eines Thrombus modelliert. Aufgrund der komplexen Natur biologischer Systeme verwenden wir einen makroskopischen kontinuumsmechanischen Ansatz aus der Theorie Poröser Medien.

Das gesamte Kontinuum wird in feste, flüssige und nährstoffhaltige Bestandteile unterteilt. Die Bestandteile werden als materiell inkompressibel und isotherm angenommen. Weiters wird das gesamte Kontinuum als vollständig gesättigt vorausgesetzt. Das Darcysche Gesetz beschreibt den Flüssigkeitsstrom in den porösen Medien. Die Volumenanteile quantifizieren die Bestandteile. Daher werden die Regionen mit Thrombenbildung anhand des Feststoffvolumenanteils bestimmt. Die Bilanzgleichungen der Bestandteile enthalten Kopplungsterme, die für den Stoffaustausch und die Wechselwirkungen zwischen den Phasen verantwortlich sind. Diese Terme spielen eine entscheidende Rolle bei der Modellierung der Bildung und des Wachstums des Thrombus.

Nach Einführen der wesentlichen Grundgleichungen wird aufbauend auf der entsprechenden Variationsformulierung ein FE-code realisiert. Mit diesem werden numerische Beispiele für die Thrombose bei AD Typ B gezeigt. Die Gleichungen sind in PANDAS implementiert, einem Finite-Elemente-Paket, das für die Lösung stark gekoppelter mehrphasiger Probleme in porösen Medien entwickelt wurde. Die Problembeschreibung ist jedoch recht komplex, da es schwierig ist, die Daten für biologische Prozesse quantitativ zu erfassen und keine Möglichkeit besteht, Experimente an lebendem Gewebe durchzuführen. Daher stellen wir rechnerisch günstigere biphasische und realistischere triphasische Modelle vor, die eine idealisierte 2D-Geometrie verwenden. Es wird gezeigt, dass der Thrombus in den Bereichen mit niedriger Geschwindigkeit im Blut wächst. Wir untersuchen die Auswirkungen verschiedener Parameter und wählen angemessene Parameter für das Thrombuswachstum im 'false lumen'. Anschließend verwenden wir eine realistische 2d-Geometrie des 'false lumen' um die Thrombose zu simulieren und zeigen die Nützlichkeit des Modells in tatsächlichen Fällen. Das vorgeschlagene Modell bietet einen geeigneten Ansatz für die numerische Simulation von Thrombose.

CONTENTS

NOMENCLATURE

In this monograph, the notations follow the conventions commonly used in modern continuum mechanics, cf. Ehlers [1], Bonet & Wood [2], and Holzapfel [3]. In addition, the symbols used follows the established nomenclature given by Ehlers [4] and De Boer [5].

General conventions

$(\cdot)$			placeholder for arbitrary quantities
$a, b, ...$	or	ϕ, ψ,...	scalars
$\mathbf{a}$, $\mathbf{b}$, $\mathbf{A}$, $\mathbf{B}$,...	or	$\boldsymbol{\phi}, \boldsymbol{\psi}, \boldsymbol{\Phi}, \boldsymbol{\Psi}$,...	vectors and second-order tensors

Index and suffix conventions

i,j,k	indices as super- or subscripts
$(\cdot)_\alpha$	subscripts indicate kinematical quantities of a constituent within porous-media
$(\cdot)^\alpha$	superscripts indicate non-kinematical quantities of a constituent within porous-media
$(\cdot)^\alpha_{O\alpha}$	initial values of non-kinematical quantities with respect to the referential configuration of a constituent
$\dot{(\cdot)} = \mathrm{d}(\cdot)/\mathrm{d}t$	total time derivative with respect to the overall aggregate φ
$(\cdot)'_\alpha = \mathrm{d}_\alpha(\cdot)/\mathrm{d}t$	material time derivative following the motion of φ^α
$\tilde{(\cdot)}$	quantity in intermediate configuration (polar decomposition)
$(\cdot)_0$	quantity at time $t = 0$
$\mathbf{a} \cdot \mathbf{b} = a_i b_i = c$	single contraction of vectors $\mathbf{a}$ and $\mathbf{b}$
$\mathbf{A} : \mathbf{B} = A_{ij} B_{ij} = c$	double contraction of second-order tensors $\mathbf{A}$ and $\mathbf{B}$
$\mathbf{A}\mathbf{b} = A_{ij} b_j = c_i = \mathbf{c}$	matrix $\mathbf{A}$ and vector $\mathbf{b}$ multiplication
$\mathbf{A}\mathbf{B} = A_{ij} B_{jk} = C_{ik} = \mathbf{C}$	matrix-matrix multiplication of second-order tensors $\mathbf{A}$ and $\mathbf{B}$
$\mathbf{a} \otimes \mathbf{b} = a_i b_j = C_{ij} = \mathbf{C}$	tensor product of vectors $\mathbf{a}$ and $\mathbf{b}$

Symbol	Unit	Description
α		constituent identifier, i.e., $\alpha = \{S, L, N\}$
μ^S	$[N/m^2]$	Lam*é* constant
λ^S	$[N/m^2]$	Lam*é* constant
φ, φ^α		whole aggregate and constituent α
$\mathcal{A}^*, \mathcal{A}_*$		pull-back and push-forward operators
$\mathcal{B}, \mathcal{B}^\alpha$		aggregate body and constituent body
$\mathcal{B}_0$		aggregate body at time zero
$\mathcal{C}$	$[kg/m^3 s]$	maximum mass exchange
$\varepsilon, \varepsilon^\alpha$	$[J/kg]$	mass-specific internal energy of φ and φ^α
$\hat{\varepsilon}^\alpha$	$[J/m^3 s]$	volume-specific direct energy production of φ^α
$\hat{\zeta}^\alpha$	$[J/Km^3 s]$	volume-specific direct entropy production of φ^α
η, η^α	$[J/Kkg]$	mass-specific entropy of φ and φ^α
$\hat{\eta}, \hat{\eta}^\alpha$	$[J/Km^3 s]$	volume-specific total entropy production of φ and φ^α
$\sigma_\eta, \sigma_\eta^\alpha$		volume-specific external entropy supply of φ and φ^α
σ, σ^α		scalar-valued supply terms of mechanical quantities
$\boldsymbol{\sigma}, \boldsymbol{\sigma}^\alpha$		vector-valued supply terms of mechanical quantities
$\boldsymbol{\phi}, \boldsymbol{\phi}^\alpha$		general vector-valued mechanical quantities
$\boldsymbol{\phi}_\eta, \boldsymbol{\phi}_\eta^\alpha$	$[J/Km^2 s]$	entropy efflux vector of φ and φ^α
$\boldsymbol{\Phi}, \boldsymbol{\Phi}^\alpha$		general tensor-valued mechanical quantities
Θ, Θ^α	$[K]$	absolute Kelvin's temperature of φ and φ^α
ρ	$[kg/m^3]$	density of overall aggregate φ
$\rho^\alpha, \rho^{\alpha R}$	$[kg/m^3]$	partial and realistic density of φ^α
$\hat{\rho}^\alpha$	$[kg/m^3 s]$	volume-specific mass production of φ^α
$\mathcal{P}_0, \mathcal{P}_t$		subdomain at time zero and t
$\boldsymbol{\tau}, \boldsymbol{\tau}^\alpha, \boldsymbol{\tau}_E^\alpha$	$[N/m^2]$	Kirchhoff (extra- $(\cdot)_E$) stress tensors of φ and φ^α
λ_S^i		eigenvalues of $\mathbf{b}_S$ or $\mathbf{C}_S$
β_1, β_2		material parameters
$\gamma, \boldsymbol{\gamma}$		arbitrary scalar- and vector-valued field functions
ξ		local coordinates
Ω		spatial domain

Symbol	Unit	Description
ψ^α	$[J/kg]$	mass-specific Helmholtz free energy of φ^α
Ψ, Ψ^α		volume-specific densities of scalar mechanical quantities of φ and φ^α
$\hat{\Psi}, \hat{\Psi}^\alpha$		volume-specific productions of scalar mechanical quantities
$\overline{\Psi}^\alpha$		chemical potential of φ^α
$\boldsymbol{\Psi}, \boldsymbol{\Psi}^\alpha$		volume-specific densities of vector mechanical quantities of φ and φ^α
$\hat{\boldsymbol{\Psi}}, \hat{\boldsymbol{\Psi}}^\alpha$		volume-specific productions of vector mechanical quantities
$\chi_\alpha, \chi_\alpha^{-1}$		motion and inverse motion function of φ^α
$\mathcal{L}_\mathbf{v}$		Lie derivative
$\mathbf{b}_S$		left Cauchy-Green solid deformation tensor
$\mathbf{b}$	$[m/s^2]$	mass-specific volume force vector
$\mathbf{C}_S$		right Cauchy-Green solid deformation tensor
$\mathbf{d}_S$	$[1/s]$	symmetric part of spatial velocity gradient of solid
$\mathrm{d}a$	$[m^2]$	area element of φ in current configuration
$\mathrm{d}A_\alpha$	$[m^2]$	area element of φ^α in reference configuration
$\mathrm{d}v$	$[m^3]$	bulk volume element of φ in current configuration
$\mathrm{d}v^\alpha$	$[m^3]$	partial volume element of φ^α in current configuration
$\mathrm{d}V_\alpha$	$[m^3]$	volume element of φ^α in reference configuration
$\mathrm{d}\mathbf{x}$	$[m]$	line element of φ in current configuration
$\mathrm{d}\mathbf{X}_\alpha$	$[m]$	line element of φ^α in reference configuration
$\hat{e}^\alpha$	$[J/m^3 s]$	volume-specific total energy production of φ^α
$\mathbf{e}_S$		Almansi solid strain tensor
$\mathbf{f}^\alpha$	$[N]$	force vector of φ^α
$\mathbf{E}_S$		Green-Lagrangean solid strain tensor
$\mathbf{F}_\alpha$		material deformation gradient of φ^α
$\mathbf{h}_S$		arbitrary spatial tensor field
$\hat{\mathbf{h}}^\alpha$	$[N/m^2]$	volume-specific total angular momentum production of φ^α

Symbol	Unit	Description
$\mathbf{H}_S$		pull-back of $\mathbf{h}_S$ to the reference configuration
I_S, II_S, III_S		principal invariants of $\mathbf{C}_S$ and $\mathbf{b}_S$
J_α		Jacobian determinant of φ^α
$\mathbf{J}_n$		jacobian tangent matrix at time t_n
k^F	$[m/s]$	Darcy's permeability
K^F	$[m^4/Ns]$	specific permeability
K^S	$[m^2]$	intrinsic permeability
$\boldsymbol{l}_S$	$[1/s]$	spatial velocity gradient of solid
$\mathbf{L}_S$	$[1/s]$	material velocity gradient of solid
m^α	$[kg]$	mass of the constituent φ^α
n^α		volume fraction of φ^α
$\hat{\mathbf{n}}_S^i$		eigenvectors of $\mathbf{b}_S$ in the current configuration
N_e		total number of elements
N_n		number of nodes in each element
N_N		total number of nodes
$\hat{\mathbf{N}}_S^i$		eigenvectors of $\mathbf{C}_S$ in the reference configuration
$\mathbf{n}$		outward-oriented unit surface normal vector
O		origin of Euclidean space
p	$[N/m^2]$	Lagrangean multiplier
p^α	$[N/m^2]$	Lagrangean multiplier of φ^α
$\hat{\mathbf{p}}^\alpha, \hat{\mathbf{p}}_E^\alpha$	$[N/m^3]$	volume-specific (extra- $(\cdot)_E$) momentum production of φ^α
P^α		material points of φ^α
$\mathbf{P}^\alpha$	$[N/m^2]$	1^{st} Piola-Kirchhoff stress tensor of φ^α
$\mathbf{q}, \mathbf{q}^\alpha$	$[J/m^2s]$	heat influx vector of φ and φ^α
r, r^α	$[J/kgs]$	mass- specific external heat supply
$\mathbf{R}_S$		solid rotation tensor
$\mathbf{S}^\alpha$	$[N/m^2]$	2^{nd} Piola-Kirchhoff Piola stress tensor of φ^α
t	$[s]$	time
t_0	$[s]$	initial time

Symbol	Unit	Description
$\mathbf{t}^\alpha$	$[N/m^2]$	surface traction vector of φ^α
$\mathbf{T}, \mathbf{T}^\alpha, \mathbf{T}_E^\alpha$	$[N/m^2]$	Cauchy (extra- $(\cdot)_E$) stress tensors of φ and φ^α
$\mathbf{u}_S$	$[m]$	solid displacement vector
$\mathbf{U}_S$		right solid stretch tensor
$\mathbf{v}_\alpha$	$[m/s]$	diffusion velocity of φ^α
V, V^α	$[m^3]$	Volume of $\mathcal{B}$ and partial volume of $\mathcal{B}^\alpha$
$\mathbf{V}_S$		left solid stretch tensor
$\mathbf{w}_S$	$[1/s]$	skew-symmetric part of solid spatial velocity gradient
$\mathbf{w}_{FS}$	$[m/s]$	seepage velocity
$\mathbf{x}$	$[m]$	current position vector
$\mathbf{x}'_\alpha$	$[m/s]$	velocity vector of φ^α
$\mathbf{x}''_\alpha$	$[m/s^2]$	acceleration vector of φ^α
$\dot{\mathbf{x}}$	$[m/s]$	velocity of overall aggregate φ
$\ddot{\mathbf{x}}$	$[m/s^2]$	acceleration of overall aggregate φ
$\mathbf{X}_\alpha$	$[m]$	reference position vector of φ^α

1 INTRODUCTION AND OVERVIEW

1.1 Motivation

Aorta is the largest blood vessel in the body and is the main artery that carries blood from the heart to the whole body. The heart pumps the blood from the left ventricle into the aorta via the aortic valve, which opens and closes with each heartbeat to allow a one-way blood flow. One of the most common forms of the acute aortic syndrome is Aortic Dissection (AD). It begins when a tear occurs in the inner layer (intima) of the aortic wall. This tear allows the blood to flow between the inner and middle layers causing them to separate (dissect). This second blood-filled channel is called the false lumen. It can lead to aortic rupture or decreased blood flow to the organs and cause short- or long-term damage. AD is a serious condition and may be fatal if not treated early. The risk and nature of the Aortic Dissection complication depend strongly on the affected area of the aorta. There are two types of AD depending on the location of the dissection. In type A AD, the dissection happens in the ascending part of the aorta, where the expansion of the false lumen can push other aorta branches and reduce blood flow. In contrast, the dissection occurs in the descending part of the aorta in type B AD, which may extend into the abdomen, cf. Figure 1.1 [6, 7].

Complete or partial thrombosis in the false lumen is a significant predictor of mortality in patients [9, 10]. Thrombosis is the process which prevents excessive bleeding by forming a spatial structure called a thrombus (blood clot). The formation of a thrombus involves a complex sequence of biochemical reactions. Humans possess an inbuilt system by which blood remains fluid and protects against the dangers of haemorrhage (bleeding). However, an injury to a blood vessel initiates haemostasis. Haemostasis is a mechanism which prevents and stops bleeding from a blood vessel by forming a thrombus. Haemostasis involves three major processes: constriction of blood vessels, primary hemostasis, and secondary hemostasis [6, 11, 12]. We briefly overview these three processes as follows:

• The blood vessel constricts at the site as soon as an injury occurs. The constriction happens due to the reflex neurogenic mechanism and secretion of endothelin, a vasoconstrictor. This effect helps to decrease the blood flow/loss and begin the clotting process. However, this effect is transient and occurs for a brief period.

• The next step is the activation of platelets and the coagulation cascade (clotting factors). The small blood cells (platelets) and various clotting factors (I to XIII) are always in the blood in their inactive form, ready to be activated within seconds of an injury. Once the blood is exposed to components of the injured wall (collagen, subendothelial collagen, von Willebrand factor), the platelets are activated. The von Willebrand factor acts as a glue and mediates the linking of platelets to collagen. As a result, the activated platelets

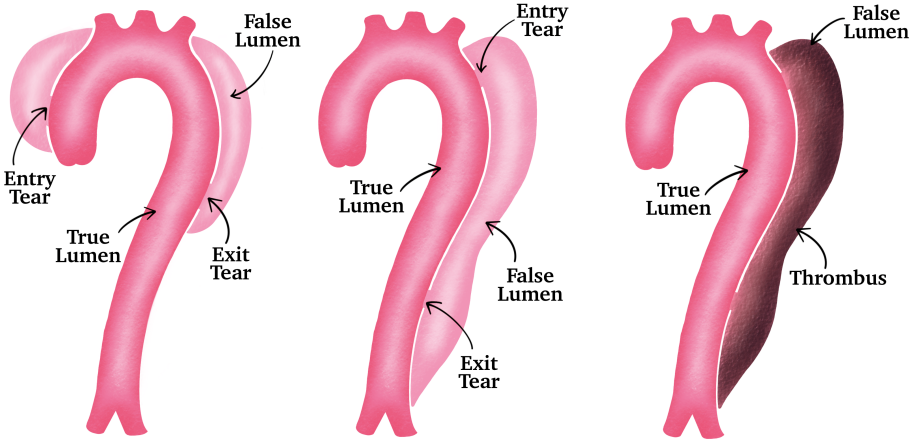

(a) Type A (b) Type B (c) Thrombosis

Figure 1.1: Illustrations of the entry tear, exit tear, true lumen, and false lumen in (a) type A Aortic Dissection, (b) type B Aortic Dissection, and (c) formation of thrombus in type B Aortic Dissection [8].

change their shape dramatically (from small rounded disks to flat plates with a moderately increased surface area). As the platelets accumulate at the injury site, they form a platelet plug. This is the process of primary haemostasis.

• In addition, the activated platelets release prothrombotic molecules leading to an increase in platelet aggregation. Moreover, the clotting factors interact in a complicated series of chemical reactions leading to thrombin formation. Thrombin converts the fibrinogen, a blood clotting factor, into long, insoluble fibrin fibre. The fibrin forms a mesh, and it entraps more platelets essential for developing a stable clot. This is the process of secondary haemostasis. It lasts longer than the initial platelet plug. Fibrin and platelets then form a permanent plug to prevent further blood loss.

Coagulation, a part of secondary hemostasis, is a complex chain reaction where one clotting factor activates the next in a multistep pathway. Coagulation has two activation pathways: extrinsic and intrinsic, cf. Figure 1.2. The intrinsic pathway activates when blood comes in contact with an abnormal surface and responds to the endothelial collagen, which is exposed when endothelial damage occurs. It leads to the activation of factor XII and the sequential activation of factors XI and IX. The activated IX combines with VIII in the presence of calcium ions and platelet factor three (PF_3) to form a complex that activates factor X. The extrinsic pathway starts due to tissue damage. The endothelial cells release the tissue factor (factor III) or thromboplastin on the damage. Factor VII and tissue factor

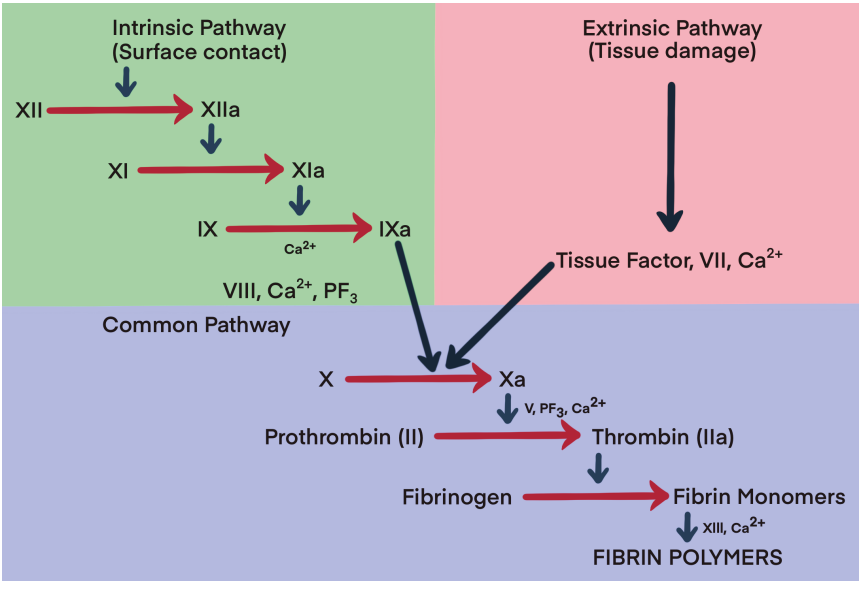

Figure 1.2: Schematic representation of the coagulation mechanism's intrinsic, extrinsic, and common pathways [11].

form a complex called TF-VIIa. Finally, intrinsic and extrinsic pathways converge to a common pathway, and the complexes formed in the respective pathways activate factor X. The activated factor X leads to the activation of prothrombin (factor II) to thrombin (factor IIa) in the presence of factor V, PF_3, and calcium ions. It further converts the fibrinogen (factor I) to fibrin monomers. Monomeric fibrin is then polymerised to form fibrin fibre by activating factor XIII [13]. The fibrin fibres, along with the platelets, create a stable, permanent plug called a thrombus. This process continues leading to the growth of thrombus. However, a negative feedback mechanism is in place to prevent over-coagulation. The reader is referred to Mohan [11] for a detailed explanation of thrombosis.

Furthermore, Virchow's triad describes three physiological factors that can result in thrombosis. These factors are endothelial injury, hypercoagulability of blood and stasis of blood flow [14, 15]. As mentioned earlier, endothelial injury stimulates the platelets and coagulation process. The thrombus consists of small blood cells (platelets) and fibrous protein (fibrin) that stop the bleeding at the injury site. Hypercoagulability means an increased tendency of coagulation in the body due to inherited or acquired disorders. Finally, stasis of the blood flow refers to the condition of slow blood flow. In such a situation, the natural anticoagulation properties are affected, and the possibility of the formation of thrombus increases. Though all three factors are essential, blood stasis is considered the most con-

sequential of the three factors [16].

Aortic Dissection is a catastrophic disease. AD can occur due to high blood pressure leading to increased stress on the aortic wall, weakening of the wall, pre-existing aneurysm or defects in the aortic valve [17, 18]. It occurs principally in two epidemiologic groups. The first group is men aged 40 to 60 years with pre-existing hypertension, and the second is younger patients with systemic or localised connective tissue abnormalities affecting the aorta. The estimated occurrence of AD is 5 to 30 cases per million people annually. Among these, the acute cases are 2 to 3.5 cases per 100,000 people per year, accounting for 6,000 to 10,000 cases in the United States alone [19]. To understand the gravity of Aortic Dissection, in the case of a ruptured aortic aneurysm, approximately 75% of patients make it to the emergency department alive, whereas 40% of the patients die immediately from AD [19]. The speed of lethality and the mode of death for acute cases often involves severe physiologic disorders from complications such as myocardial infarction, malperfusion syndromes to the brain, kidney, spinal cord and gut or bleeding from aortic rupture. This has boosted the importance of early diagnosis and treatment, which is critical for survival. [20]. Also, the mortality rate for AD is high, especially in acute cases. In the case of type B AD, the mortality rate is excessive in the first seven days due to severe complications, such as malperfusion or rupture in the aorta. Even though a general agreement exists regarding the need for immediate surgical repair for patients with acute ascending Aortic Dissection (type A dissection), the optimal treatment of type B dissection stays a matter of debate [21–25]. The short-term and long-term diagnosis for AD remains unclear, leading to an interest in computational methods to help with the decision-making process for the treatment. In addition, understanding the mechanics of growth in such chronic conditions can open new directions in medical device design, personalised medicine, and controlling disease progression [26].

1.2 Scope, Aims and State of the Art

Modelling of thrombus is a continuum-mechanical problem that cannot be uniquely classified within well-known solid or fluid mechanics disciplines. Instead, one has to consider multiphasic aggregate and the associated characteristics of the constituents. Therefore, this thesis aims to develop a thermodynamically consistent model that is as simple as possible but simultaneously captures the relevant properties of the thrombus.

In the last decades, hard and soft biological tissues have been extensively modelled by using continuum mechanics. In addition, there has been an increase in interest in modelling the growth of biological tissues. The developments in the biomechanics of the growth and remodelling of the biological tissues are given by Tabler [27], Fung [28,29], and Humphery [30]. Different methods have been introduced and developed to describe the remodelling and growth process from the continuum mechanics point of view. Cowin & Hegedus [31]

presented the first continuum theory for describing growth in hard tissues like bones. They introduced the open system theory, where the fluid constituents are neglected, and the solid matrix is assumed to influence the overall mechanical behaviour. This model was then further extended by various researchers, such as Nackenhorst [32], Kuhl et al. [33,34], and Epstein & Maugin [35]. Ambrosi & Mollica [36,37] introduced a model for the growth of tumour spheroids with nutrient-concentration triggered growth.

For biological tissues, it is clear that the internal structure and properties of the growing tissue change other than its shape and size. It consists of many constituents such as different cell types, fibres, and extracellular matrix (ECM) [38]. Therefore, the growth process can alter the amount of these components and their mechanical properties. During thrombosis, as platelets cohere into a platelet aggregate, they do not immediately form a solid mass. Instead, they create a porous network with voids and channels. After many reactions, the thrombus changes to a gel-like structure and finally to a stiff solid state (cf. Section 1.1). Therefore, we use a macroscopic continuum-mechanical approach of the Theory of Porous Media (TPM) which provides an excellent framework to describe the overall behaviour of the multiphasic thrombus.

Woltmann first attempted to model binary mixtures when he introduced the concept of volume fractions [39,40]. After that, many scientists like Biot [41] and Heinrich & Desoyer [42] used this concept to model consolidation problems. The TPM was developed based on the Theory of Mixtures. The Theory of Mixtures describes multicomponent continua, including the interactions between the constituents. The reader is referred to work by Bowen [43], Truesdell & Toupin [44], Truesdell & Noll [45], and Truesdell [46]. After that, Bowen [47,48] restricted the Theory of Mixtures by the concept of volume fractions to incorporate microscopic information. Therein, Bowen discusses all the kinematics and balance relations valid for mixtures by considering the partial quantities and relations. This was continuously improved and further developed by de Boer [5, 49], de Boer & Ehlers [50], Ehlers [39, 51], and Ehlers & Bluhm [4] to the current understanding of the TPM. De Boer [5] has presented an excellent insight into the historical development of TPM in his book.

Based on TPM, various models have been proposed to model the mechanical behaviour and the growth and remodelling process of the biological tissues. A biphasic model has been proposed by Ehlers & Markert [52] for describing the mechanical behaviour of hydrated soft tissues and by Wagner & Ehlers [53] for describing the behaviour of brain tissue. Furthermore, a biphasic model has been proposed by Karajan [54] to describe the mechanical behaviour of the Intervertebral Disc (IVD). Ricken et al. [55] presented a biphasic model for liver perfusion remodelling. Moreover, multiphasic models for growth and remodelling have been proposed by Ricken & Bluhm [56] and Ricken et al. [57,58] for isotropic and transversely isotropic biological tissues. They have introduced stress-dependent growth processes. Preziosi & Tosin [59] have presented multiphasic tumour growth models. Krause [60] presented a tumour growth model, and Krause et al. [61]

proposed a bone remodelling model where the growth energy concept is used. Certainly, TPM has been used to describe the behaviour and growth of soft biological tissues [62], but it has not appeared in literature with application to thrombosis. Therefore, the recent works using TPM for modelling biological growth motivate the use of this approach in the presented work. However, modelling the growth of living tissues has its challenges, which is very well summarised by Ambrosi et al. [63].

As mentioned earlier, chemical, mechanical and metabolic factors drive the growth process of the thrombus. Because of the multiphasic structure of the thrombus, we present a triphasic model. The porous body is divided into three phases: solid, liquid and nutrients. All three phases simultaneously occupy each material point. We assume that all the constituents are materially incompressible and isothermal, and the whole aggregate is fully saturated. The balance equations of the constituents have coupling terms which take care of the interactions between them. The essential coupling term for the growth process is the mass exchange term in the volume balances. Due to the need for detailed knowledge and parameters to quantify the influence of different factors, the model description is more challenging. However, the effects of the blood velocity and the nutrients on the growth of thrombus are well-researched [64,65]. The dependence of thrombus growth rate on the blood velocity was found experimentally by Begent & Born [66]. Therefore, we present a velocity- and nutrient-concentration-induced growth model based on TPM. We treat the highly coupled set of differential equations within the framework of the standard Galerkin procedure and implement the weak forms in the nonlinear finite element solver PANDAS.

1.3 Outline of the Thesis

After the introduction and overview, Chapter 2 presents the fundamentals of continuum mechanics needed to model the growth of porous thrombus. First, we briefly introduce the Theory of Porous Media. Then, to describe the mechanical behaviour of the thrombus, we model the whole aggregate as multiphase continua consisting of superimposed and interacting solid, liquid and nutrient phases. Thereafter, we introduce the essential kinematical relations for non-linear formulation. As a next step, the overall and constituent balance equations are introduced.

The objective of Chapter 3 is to introduce suitable assumptions following the characteristics of the model and thrombosis, and reformulate the balance equations accordingly. After this, the fundamentals of the material theory, like determinism, equipresence, local action, and material frame indifference, are introduced. Then, the entropy inequality is evaluated to obtain the necessary restrictions to formulate the missing constitutive equations and develop a thermodynamically consistent model. Finally, the principle of isotropic elasticity is discussed, and the Helmholtz free energy function is formulated.

Chapter 4 deals with the numerical treatment of the governing equations. Firstly, the weak forms are formulated in the framework of the standard Galerkin procedure (Bubnov-Galerkin). The system of equations is discretised in space using mixed finite elements. Then, the concept of geometry transformation and numerical integration is introduced. The system of equations is discretised in time using the implicit Euler scheme. Thereafter, the Newton-Raphson scheme is introduced briefly to solve the system of non-linear equations.

In Chapter 5, the presented model is applied to the problem of thrombosis. At first, the implementation of a computationally less expensive biphasic model is presented using a 2-d idealised geometry. After that, the triphasic model is implemented, and its features are discussed. Then, we use a 2-d realistic geometry of the false lumen while drawing an analogy to the process of thrombosis. Finally, Chapter 6 presents the summary and outlook of the presented work.

2 FUNDAMENTALS OF THEORY OF POROUS MEDIA

This section briefly overviews the continuum-mechanical fundamentals needed to understand the modelling using the Theory of Porous Media framework. The kinematical relations, polar and spectral decomposition concepts, and strain and stress measures are introduced in this context. Furthermore, we give a concise description of the balance equations from the TPM point of view. This approach can be applied in fields where the material's porous structure needs to be considered for suitable modelling, such as geotechnical problems and biomechanics. The book by de Boer [5] provides excellent insight into the historical development and the current state of the Theory of Porous Media. The reader is referred to Ehlers [39], Truesdell & Noll [45], and Markert [67] for more details on TPM. Bonet & Wood [2] and Holzapfel [3] comprehensively describe the fundamentals of non-linear continuum mechanics for single-phase materials.

2.1 The Theory of Porous Media

A thrombus is a multiphasic porous material formed by several interacting components. Hence, we use the modelling approach of the TPM as it provides an excellent framework to describe the multiphasic microstructure of the thrombus (cf. Section 1.2). Moreover, it allows us to model the thrombus without detailed knowledge of its microstructure, which would be almost impossible to know quantitatively. In this regard, we define a local representative elementary volume (REV) and consider all the individual constituents of the whole aggregate to be in a state of ideal disarrangement. Following this, we smear out (homogenise) the actual microstructure through the considered domain by applying the real or virtual averaging process, yielding a macroscopic substitute for the overall aggregate. Therefore, all the geometric and physical quantities on the macroscale are understood as statistical mean values of the microscale quantities. This process leads to a model with superimposed and interacting continua [5, 39].

We obtain a macro-scale model on applying the homogenisation procedure over a REV of the thrombus. The immiscible parts lead to a triphasic model φ consisting of the constituents φ^α

$$\varphi = \bigcup_\alpha \varphi^\alpha = \varphi^S \cup \underbrace{\varphi^L \cup \varphi^N}_{\varphi^F}, \tag{2.1}$$

where $\alpha = \{S, L, N\}$, cf. Figure 2.1. The solid phase φ^S consists of subendothelial collagen, activated platelets, fibrin and wall cells, which is saturated by fluid φ^F. The fluid itself consists of nutrient phase φ^N, which are deactivated platelets and clotting factors, and liquid phase φ^L, which represents blood minus the nutrients and activated platelets (cf. Section 1.1).

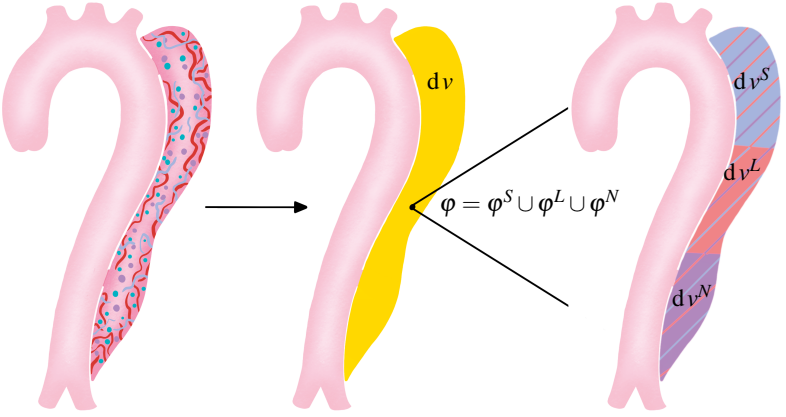

Figure 2.1: Illustration of the microstructure of the porous false lumen (left), macro-model obtained by volumetric homogenisation process (center), and superimposed continua (right).

2.2 The Concept of Volume Fractions

To account for the microstructure of the model φ, the sum of the constituent's partial volumes V^α gives the volume V of the multiphasic body $\mathcal{B}$

$$V = \int_{\mathcal{B}} \mathrm{d}v = \sum_{\alpha} V^\alpha, \qquad \text{where} \qquad V^\alpha = \int_{\mathcal{B}^\alpha} \mathrm{d}v = \int_{\mathcal{B}} \mathrm{d}v^\alpha =: \int_{\mathcal{B}} n^\alpha \, \mathrm{d}v. \tag{2.2}$$

Following this, the volume fractions n^α are defined as the local ratio of the respective partial volume element $\mathrm{d}v^\alpha$ with respect to the bulk volume element $\mathrm{d}v$ of the overall aggregate φ reading

$$n^\alpha := \frac{\mathrm{d}v^\alpha}{\mathrm{d}v}. \tag{2.3}$$

Furthermore, the equations (2.2) and (2.3) lead to the saturation condition

$$\sum_{\alpha} n^\alpha = n^S + n^L + n^N = 1, \tag{2.4}$$

which has to be permanently fulfilled to prevent the development of vacant space in the overall aggregate φ. In the case of injury (Aortic Dissection), the nutrients are available in large quantities involving complex biochemical reactions. Therefore in the presented monograph, the saturated porous medium is treated as a combination of immiscible phases

φ^α, described by their volume fractions n^α. For miscible components, the approach of molar concentrations should be used [60, 68]. Following the definition of the volume fractions n^α, partial and realistic densities are introduced. The partial density ρ^α is the ratio of the constituent's mass $\mathrm{d}m^\alpha$ to the bulk volume element $\mathrm{d}v$. The realistic density $\rho^{\alpha R}$ is the ratio of the constituent's mass $\mathrm{d}m^\alpha$ to the constituent's volume element $\mathrm{d}v^\alpha$ yielding

$$\rho^\alpha = \frac{\mathrm{d}m^\alpha}{\mathrm{d}v} \qquad \text{and} \qquad \rho^{\alpha R} = \frac{\mathrm{d}m^\alpha}{\mathrm{d}v^\alpha}. \tag{2.5}$$

Inserting equation (2.3) in (2.5), we get the following relation between the densities

$$\rho^\alpha = n^\alpha \rho^{\alpha R}. \tag{2.6}$$

From the above equation, it is clear that the partial density ρ^α of a constituent can change due to changes in its realistic density $\rho^{\alpha R}$ or volume fraction n^α. That means that the material incompressibility ($\rho^{\alpha R} = \text{const.}$) of any constituent does not lead to the property of bulk incompressibility ($\rho^\alpha = \text{const.}$) because the volume fraction can change due to deformation or mass exchange between the phases. Finally, the summation of all the partial densities ρ^α yields the density ρ of the overall aggregate $\mathcal{B}$.

$$\rho = \sum_\alpha \rho^\alpha = \sum_\alpha n^\alpha \rho^{\alpha R}. \tag{2.7}$$

2.3 Kinematics

The following section gives a brief overview of the kinematic relations needed to study the motion and deformation of the continua and to describe the nonlinear model of a porous material. First, we focus on providing the fundamentals and introducing the kinematic relations for the multi-constituent modelling approach. After that, we briefly overview the balance relations for the multiphasic materials. The reader is referred to Ehlers [39], de Boer [5], and Markert [67] for multiphasic materials. Moreover, Bonet & Wood [2] and Holzapfel [3] give a comprehensive introduction to the kinematical quantities.

2.3.1 Motion of a Porous Material

In the context of the superimposed and interacting porous continua, particles P^α of all the constituents φ^α simultaneously occupy each spatial point $\mathbf{x}$ of the current configuration at any time t, cf. Figure 2.2. Since the particles at $\mathbf{x}$ proceed from the different reference positions $\mathbf{X}_\alpha$ at time t_0, each constituent is assigned its own motion function

$$\mathbf{x} = \boldsymbol{\chi}_\alpha(\mathbf{X}_\alpha, t). \tag{2.8}$$

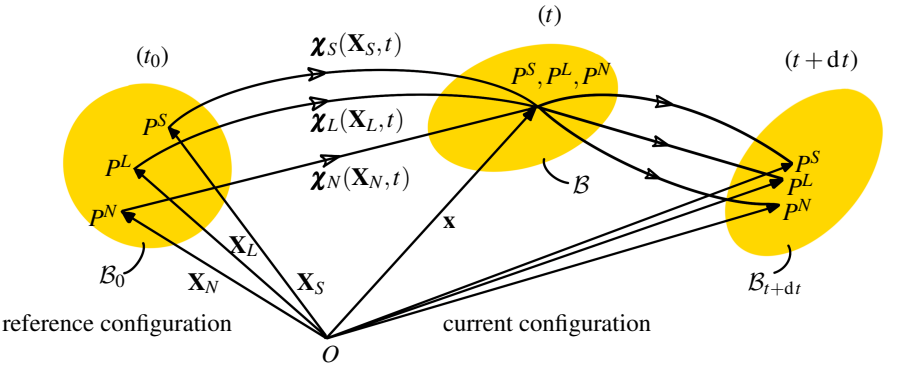

Figure 2.2: Motion of a triphasic aggregate.

Each point $\mathbf{x}$ in the current configuration is occupied by only one material point P^α of each constituent φ^α. A unique inverse motion function $\boldsymbol{\chi}_\alpha^{-1}$ must exist to have a unique reference position $\mathbf{X}_\alpha$ at time t_0 for each material point P^α at $\mathbf{x}$. The necessary and sufficient condition for this is the existence of non-singular Jacobian J_α

$$\mathbf{X}_\alpha = \boldsymbol{\chi}_\alpha^{-1}(\mathbf{x},t), \qquad \text{if} \qquad J_\alpha := \det \frac{\partial \boldsymbol{\chi}_\alpha}{\partial \mathbf{X}_\alpha} \neq 0, \tag{2.9}$$

where $\det(\cdot)$ denotes the determinant operator. Following this, equation (2.8) represents the Lagrangean (material) description because it is expressed in terms of reference positions $\mathbf{X}_\alpha$. On the other hand, equation (2.9) represents the Eulerian (spatial) description since it is expressed in terms of the current positions $\mathbf{x}$.

2.3.2 Velocity and Acceleration Fields

Since all the particles proceed from different reference positions, each constituent has its own velocity $\mathbf{x}'_\alpha$ and acceleration $\mathbf{x}''_\alpha$ fields. These are introduced in the Lagrangean setting using the material time derivative as follows

$$\mathbf{x}'_\alpha(\mathbf{X}_\alpha,t) = \frac{\mathrm{d}\boldsymbol{\chi}_\alpha(\mathbf{X}_\alpha,t)}{\mathrm{d}t} \qquad \text{and} \qquad \mathbf{x}''_\alpha(\mathbf{X}_\alpha,t) = \frac{\mathrm{d}^2\boldsymbol{\chi}_\alpha(\mathbf{X}_\alpha,t)}{\mathrm{d}t^2}. \tag{2.10}$$

We can obtain the Eulerian representation of velocity and acceleration by inserting the inverse motion function (2.9) in equation (2.10)

$$\mathbf{x}'_\alpha(\mathbf{x},t) = \mathbf{x}'_\alpha[\boldsymbol{\chi}_\alpha^{-1}(\mathbf{x},t),t] \qquad \text{and} \qquad \mathbf{x}''_\alpha(\mathbf{x},t) = \mathbf{x}''_\alpha[\boldsymbol{\chi}_\alpha^{-1}(\mathbf{x},t),t]. \tag{2.11}$$

In addition, the mixture velocity $\dot{\mathbf{x}}$ of the aggregate φ and the diffusion velocity $\mathbf{v}_\alpha$ of the constituent φ^α is given by

$$\dot{\mathbf{x}} = \frac{1}{\rho}\sum_\alpha \rho^\alpha \mathbf{x}'_\alpha, \tag{2.12}$$

and

$$\mathbf{v}_\alpha = \mathbf{x}'_\alpha - \dot{\mathbf{x}} \qquad \text{with} \qquad \sum_\alpha \rho^\alpha \mathbf{v}_\alpha = 0. \tag{2.13}$$

All the time derivatives $(\cdot)'_\alpha$ and $\dot{(\cdot)}$ are the material time derivatives. In the case of the Lagrangean description, the material time derivative reduces to the partial time derivative because the reference positions $\mathbf{X}_\alpha$ are fixed in time. On the other hand, one must be careful with the Eulerian description because the current positions $\mathbf{x}$ depend on time. Therefore, one must include the inner (implicit) derivatives in the material time derivative. For example, consider γ and $\boldsymbol{\gamma}$ as arbitrary scalar- and vector-valued field functions that are steady and sufficiently steady differentiable. Then, the material time derivatives of γ and $\boldsymbol{\gamma}$ following the motion of the constituents φ^α and the barycentric motion of the aggregate φ are defined as follows

$$\begin{aligned}
\gamma'_\alpha(\mathbf{x},t) &= \frac{\mathrm{d}_\alpha \gamma}{\mathrm{d}t} = \frac{\partial \gamma}{\partial t} + \frac{\partial \gamma}{\partial \mathbf{x}}\frac{\partial \mathbf{x}}{\partial t} = \frac{\partial \gamma}{\partial t} + \operatorname{grad}\gamma \cdot \mathbf{x}'_\alpha, \\
\boldsymbol{\gamma}'_\alpha(\mathbf{x},t) &= \frac{\mathrm{d}_\alpha \boldsymbol{\gamma}}{\mathrm{d}t} = \frac{\partial \boldsymbol{\gamma}}{\partial t} + \frac{\partial \boldsymbol{\gamma}}{\partial \mathbf{x}}\frac{\partial \mathbf{x}}{\partial t} = \frac{\partial \boldsymbol{\gamma}}{\partial t} + (\operatorname{grad}\boldsymbol{\gamma})\mathbf{x}'_\alpha, \\
\dot{\gamma}(\mathbf{x},t) &= \frac{\mathrm{d}\gamma}{\mathrm{d}t} = \frac{\partial \gamma}{\partial t} + \frac{\partial \gamma}{\partial \mathbf{x}}\frac{\partial \mathbf{x}}{\partial t} = \frac{\partial \gamma}{\partial t} + \operatorname{grad}\gamma \cdot \dot{\mathbf{x}}, \\
\dot{\boldsymbol{\gamma}}(\mathbf{x},t) &= \frac{\mathrm{d}\boldsymbol{\gamma}}{\mathrm{d}t} = \frac{\partial \boldsymbol{\gamma}}{\partial t} + \frac{\partial \boldsymbol{\gamma}}{\partial \mathbf{x}}\frac{\partial \mathbf{x}}{\partial t} = \frac{\partial \boldsymbol{\gamma}}{\partial t} + (\operatorname{grad}\boldsymbol{\gamma})\dot{\mathbf{x}}.
\end{aligned} \tag{2.14}$$

where $\operatorname{grad}(\cdot) = \partial(\cdot)/\partial\mathbf{x}$ is the partial derivative of the $(\cdot)$ with respect to the current position $\mathbf{x}$.

Furthermore, in TPM, the description of the coupled solid-fluid problems leads to difficulty in finding a suitable choice for the independent motions of the constituents. It is generally convenient to describe the solid matrix in the Lagrange description because the neighbouring points of the solid in the reference configuration are still close to each other in the current configuration. However, this is not true for fluids which are described in the Eulerian setting. Following this, the solid is described in the Lagrangean description using the solid displacement field $\mathbf{u}_S$. Finally, the fluid is described in the modified Eulerian setting by seepage velocity $\mathbf{w}_{FS}$, which expresses the fluid motion with respect to the deforming solid in the following way

$$\mathbf{u}_S = \mathbf{x} - \mathbf{X}_S \qquad \text{and} \qquad \mathbf{w}_{FS} = \mathbf{x}'_F - \mathbf{x}'_S. \tag{2.15}$$

2.3.3 Deformation Gradient

From equation (2.8), the material deformation gradient $\mathbf{F}_\alpha$ for each constituent φ^α is introduced as

$$\mathbf{F}_\alpha = \operatorname{Grad}_\alpha \mathbf{x} =: \frac{\partial \boldsymbol{\chi}_\alpha(\mathbf{X}_\alpha, t)}{\partial \mathbf{X}_\alpha}, \tag{2.16}$$

where $\operatorname{Grad}_\alpha(\cdot) = \partial(\cdot)/\partial \mathbf{X}_\alpha$ is the partial derivative of the $(\cdot)$ with respect to the reference position $\mathbf{X}_\alpha$. Here, $\mathbf{F}_\alpha$ can be understood as a mapping which carries the elemental line vector $\mathrm{d}\mathbf{X}_\alpha$ from the reference configuration to the $\mathrm{d}\mathbf{x}$ in the current configuration

$$\mathrm{d}\mathbf{x} = \mathbf{F}_\alpha \, \mathrm{d}\mathbf{X}_\alpha. \tag{2.17}$$

Similarly, the elemental area vector $\mathrm{d}\mathbf{A}_\alpha$ and the volume element $\mathrm{d}V_\alpha$ in the reference configuration can be mapped to the current configuration using the following relations

$$\mathrm{d}\mathbf{a} = \operatorname{cof}\mathbf{F}_\alpha \, \mathrm{d}\mathbf{A}_\alpha = (\det \mathbf{F}_\alpha)\mathbf{F}_\alpha^{-T} \, \mathrm{d}\mathbf{A}_\alpha \qquad \text{and} \qquad \mathrm{d}v = \det \mathbf{F}_\alpha \, \mathrm{d}V_\alpha, \tag{2.18}$$

where $\mathrm{d}\mathbf{a}$ and $\mathrm{d}v$ are the area and volume elements in the current configuration, respectively.

Similarly, the inverse of the deformation gradient $\mathbf{F}_\alpha^{-1}$ does the reverse mapping from the current configuration to the reference configuration. The inverse of the deformation gradient can be defined as

$$\mathbf{F}_\alpha^{-1} = \operatorname{grad} \mathbf{X}_\alpha =: \frac{\partial \boldsymbol{\chi}_\alpha^{-1}(\mathbf{x}, t)}{\partial \mathbf{x}}, \tag{2.19}$$

where $\operatorname{grad}(\cdot) = \partial(\cdot)/\partial \mathbf{x}$. The $\mathbf{F}_\alpha^{-1}$ mapping can be written as

$$\mathrm{d}\mathbf{X}_\alpha = \mathbf{F}_\alpha^{-1} \, \mathrm{d}\mathbf{x}. \tag{2.20}$$

According to equation $(2.9)_2$, a uniquely invertible motion needs a non-zero Jacobian. Starting with the undeformed state at time t_0, the condition $\mathbf{F}_\alpha(t_0) = \mathbf{I}$ holds for the deformation gradient. Here, $\mathbf{I}$ is the second-order identity tensor. Therefore, in combination with the physical constraint ($J_\alpha < 0$ meaning negative volume, cf. $(2.18)_2$), the Jacobian J_α is restricted to positive values

$$J_\alpha = \det \mathbf{F}_\alpha > 0, \qquad \text{with} \qquad \det \mathbf{F}_\alpha(t_0) = \det \mathbf{I} = 1. \tag{2.21}$$

From equation (2.15), the solid displacement vector is the primary kinematic quantity, whereas the fluid motion is represented relative to the deforming solid. Therefore, we do not need the deformation gradient for the fluids $\mathbf{F}_F$. Instead, the solid deformation gradient $\mathbf{F}_S$ serves as a primary kinematic quantity in the large strain regime. Moreover, $\mathbf{F}_S$ and $\mathbf{F}_S^{-1}$ can be expressed in terms of the solid displacement using equations $(2.15)_1$, (2.16), and (2.19)

$$\mathbf{F}_S = \mathbf{I} + \operatorname{Grad}_S \mathbf{u}_S \qquad \text{and} \qquad \mathbf{F}_S^{-1} = \mathbf{I} - \operatorname{grad} \mathbf{u}_S. \tag{2.22}$$

2.3.4 Deformation and Strain Measures

After introducing the deformation gradient, we present the deformation and strain measures. Following the framework of continuum mechanics, the deformation measure defines how a body is deformed during the motion, whereas the strain measure compares the deformed body to its undeformed state.

To define the deformation measures, we begin with the polar decomposition of the deformation gradient $\mathbf{F}_S$. We split the deformation gradient uniquely into positive definite and symmetric stretch tensors $\mathbf{U}_S$ and $\mathbf{V}_S$, and a proper orthogonal rotation tensor $\mathbf{R}_S \in \mathcal{SO}_3$ which reads as

$$\mathbf{F}_S = \underbrace{\mathbf{R}_S\mathbf{U}_S}_{\text{Right Decomposition}} = \underbrace{\mathbf{V}_S\mathbf{R}_S}_{\text{Left Decomposition}}, \tag{2.23}$$

where $\mathbf{R}_S^T = \mathbf{R}_S^{-1}$, $\det\mathbf{R}_S = 1$,$\mathbf{U}_S = \mathbf{U}_S^T$, and $\mathbf{V}_S = \mathbf{U}_S^T$. $\mathbf{R}_S\mathbf{U}_S$ is the right decomposition where $\mathbf{U}_S$ is called the right stretch tensor, and $\mathbf{V}_S\mathbf{R}_S$ is the left decomposition where $\mathbf{V}_S$ is called the left stretch tensor. Hence, in two ways, a line element $\mathrm{d}\mathbf{X}_S$ in the reference configuration can map to the line element $\mathrm{d}\mathbf{x}$ in the current configuration

$$\mathrm{d}\mathbf{x} = \mathbf{R}_S(\mathbf{U}_S\,\mathrm{d}\mathbf{X}_S) = \mathbf{V}_S(\mathbf{R}_S\,\mathrm{d}\mathbf{X}_S). \tag{2.24}$$

Together with equation (2.24) and Figure 2.3, this can be understood well. If we apply the right decomposition, the line element $\mathrm{d}\mathbf{X}_S$ is first stretched by the right stretch tensor $\mathbf{U}_S$ and gives $\mathrm{d}\tilde{\mathbf{X}}_S$ in the intermediate configuration. The rotation vector $\mathbf{R}_S$ then rotates it to give $\mathrm{d}\mathbf{x}$ in the current configuration. If we apply the left decomposition, $\mathrm{d}\mathbf{X}_S$ is first rotated by $\mathbf{R}_S$ to give $\mathrm{d}\tilde{\mathbf{x}}$ in the intermediate configuration. Then, it is stretched by $\mathbf{V}_S$ to give $\mathrm{d}\mathbf{x}$ in the current configuration. From this, it is clear that the two-field character of $\mathbf{F}_S$ is included in the rotation tensors $\mathbf{R}_S$ and not in the stretch tensors $\mathbf{U}_S$ and $\mathbf{V}_S$.

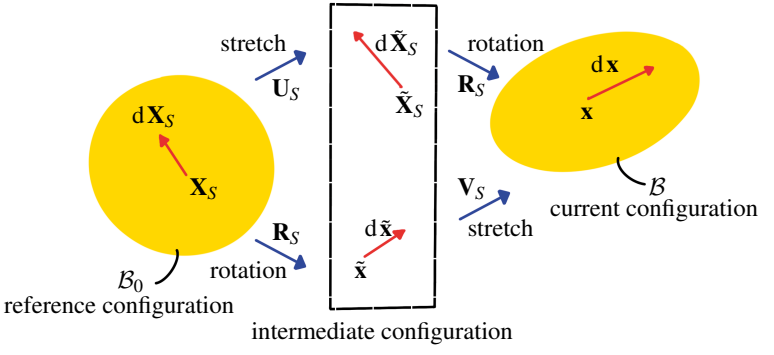

Figure 2.3: Polar Decomposition of $\mathbf{F}_S$.

Furthermore, the line elements of one configuration can be represented by the elements of the other configuration. Hence, we examine the variation in the length of the line elements in the reference configuration

$$\begin{aligned} \|\mathrm{d}\mathbf{x}\|^2 &= \mathrm{d}\mathbf{x}\cdot\mathrm{d}\mathbf{x} \\ &= (\mathbf{F}_S\,\mathrm{d}\mathbf{X}_S)\cdot(\mathbf{F}_S\,\mathrm{d}\mathbf{X}_S) \\ &= \mathrm{d}\mathbf{X}_S\cdot(\mathbf{F}_S^T\mathbf{F}_S)\,\mathrm{d}\mathbf{X}_S \\ &= \mathrm{d}\mathbf{X}_S\cdot\mathbf{C}_S\,\mathrm{d}\mathbf{X}_S. \end{aligned} \tag{2.25}$$

From the equation (2.25), one obtains the right Cauchy-Green deformation tensor $\mathbf{C}_S = \mathbf{F}_S^T\mathbf{F}_S$. Similarly, we examine the variation in the length of the line elements in the current configuration

$$\begin{aligned} \|\mathrm{d}\mathbf{X}_S\|^2 &= \mathrm{d}\mathbf{X}_S\cdot\mathrm{d}\mathbf{X}_S \\ &= (\mathbf{F}_S^{-1}\,\mathrm{d}\mathbf{x})\cdot(\mathbf{F}_S^{-1}\,\mathrm{d}\mathbf{x}) \\ &= \mathrm{d}\mathbf{x}\cdot(\underbrace{\mathbf{F}_S^{-T}\mathbf{F}_S^{-1}}_{(\mathbf{F}_S\mathbf{F}_S^T)^{-1}})\,\mathrm{d}\mathbf{x} \\ &= \mathrm{d}\mathbf{x}\cdot\mathbf{b}_S^{-1}\,\mathrm{d}\mathbf{x}. \end{aligned} \tag{2.26}$$

From the equation (2.26), one obtains the left Cauchy-Green deformation tensor $\mathbf{b}_S = \mathbf{F}_S\mathbf{F}_S^T$. Additionally, the right and the left Cauchy-Green tensors can be written in the form of stretch tensors

$$\begin{aligned} \mathbf{C}_S &= \mathbf{F}_S^T\mathbf{F}_S = (\mathbf{R}_S\mathbf{U}_S)^T(\mathbf{R}_S\mathbf{U}_S) = \mathbf{U}_S\mathbf{U}_S, \\ \mathbf{b}_S &= \mathbf{F}_S\mathbf{F}_S^T = (\mathbf{V}_S\mathbf{R}_S)(\mathbf{V}_S\mathbf{R}_S)^T = \mathbf{V}_S\mathbf{V}_S. \end{aligned} \tag{2.27}$$

Following equations (2.23) and (2.27), the right and the left Cauchy-Green tensors are related by the forward and backward rotations

$$\mathbf{C}_S = \mathbf{R}_S^T\mathbf{b}_S\mathbf{R}_S, \qquad \mathbf{b}_S = \mathbf{R}_S\mathbf{C}_S\mathbf{R}_S^T. \tag{2.28}$$

Furthermore, we introduce the strain tensors, which are dimensionless quantities and relate the state of the material in the current configuration to the reference configuration. Hence, they can capture the body's deformation at any time. Here, we introduce two nonlinear strain tensors: Green-Lagrangean $\mathbf{E}_S$ and Almansi $\mathbf{e}_S$ strain tensors. Using equation (2.25), the Green-Lagrangean strain $\mathbf{E}_S$ is derived as follows

$$\mathrm{d}\mathbf{x}\cdot\mathrm{d}\mathbf{x} - \mathrm{d}\mathbf{X}_S\cdot\mathrm{d}\mathbf{X}_S = \mathrm{d}\mathbf{X}_S\cdot\mathbf{C}_S\,\mathrm{d}\mathbf{X}_S - \mathrm{d}\mathbf{X}_S\cdot\mathrm{d}\mathbf{X}_S = \mathrm{d}\mathbf{X}_S\cdot(\underbrace{\mathbf{C}_S-\mathbf{I}}_{2\mathbf{E}_S})\,\mathrm{d}\mathbf{X}_S, \tag{2.29}$$

which gives $\mathbf{E}_S = \frac{1}{2}(\mathbf{C}_S - \mathbf{I})$. Using equation (2.26), the Almansi strain $\mathbf{e}_S$ is derived as follows

$$\mathrm{d}\mathbf{x}\cdot\mathrm{d}\mathbf{x} - \mathrm{d}\mathbf{X}_S\cdot\mathrm{d}\mathbf{X}_S = \mathrm{d}\mathbf{x}\cdot\mathrm{d}\mathbf{x} - \mathrm{d}\mathbf{x}\cdot\mathbf{b}_S^{-1}\,\mathrm{d}\mathbf{x} = \mathrm{d}\mathbf{x}\cdot(\underbrace{\mathbf{I}-\mathbf{b}_S^{-1}}_{2\mathbf{e}_S})\,\mathrm{d}\mathbf{x}, \tag{2.30}$$

which gives $\mathbf{e}_S = \frac{1}{2}(\mathbf{I} - \mathbf{b}_S^{-1})$. The Almansi strain tensor is the push-forward of the Green-Lagrangean strain tensor and is in the current configuration. The Green-Lagrangean strain is the pull-back of the Almansi strain and is present in the reference configuration, i.e.

$$\mathbf{E}_S = \frac{1}{2}(\mathbf{C}_S - \mathbf{I}) = \mathbf{F}_S^T(\mathbf{e}_S)\mathbf{F}_S, \qquad \mathbf{e}_S = \frac{1}{2}(\mathbf{I} - \mathbf{b}_S^{-1}) = \mathbf{F}_S^{-T}(\mathbf{E}_S)\mathbf{F}_S^{-1}. \tag{2.31}$$

There are further possibilities to define strain measures. For more information on the strain tensors, the reader is referred to Bonet & Wood [2] and Holzapfel [3].

2.3.5 Spectral Decomposition

We briefly overview the spectral representation in this section. For constitutive modelling, representing deformation tensors in the spectral form is often convenient. We introduce the orthogonal, and normalised eigenvectors $\hat{\mathbf{N}}_S^i \neq \mathbf{0}$ in the reference configuration and the respective eigenvalues λ_S^i for the right stretch tensor $\mathbf{U}_S$ as

$$\mathbf{U}_S\hat{\mathbf{N}}_S^i = \lambda_S^i\hat{\mathbf{N}}_S^i, \qquad \text{with} \qquad i = 1,2,3 \tag{2.32}$$

Using equations $(2.27)_1$ and (2.32), we obtain the eigenvalue problem for $\mathbf{C}_S$ as

$$\mathbf{C}_S\hat{\mathbf{N}}_S^i = \mathbf{U}_S^2\hat{\mathbf{N}}_S^i = (\lambda_S^i)^2\hat{\mathbf{N}}_S^i. \tag{2.33}$$

From the equations (2.32) and (2.33), it is clear that both $\mathbf{U}_S$ and $\mathbf{C}_S$ have the same eigenvectors $\hat{\mathbf{N}}_S^i$ but their eigenvalues differ. The eigenvalues λ_S^i of $\mathbf{U}_S$ are called principal stretches. The eigenvalues of $\mathbf{C}_S$ are the squares of the principal stretches denoted by $(\lambda_S^i)^2$.

From equation (2.23), we can get $\mathbf{V}_S = \mathbf{R}_S\mathbf{U}_S\mathbf{R}_S^T$. Using this relation and $\mathbf{R}_S^T\mathbf{R}_S = \mathbf{I}$, we obtain the eigenvalue problem for $\mathbf{V}_S$ as

$$\mathbf{V}_S(\mathbf{R}_S\hat{\mathbf{N}}_S^i) = \mathbf{R}_S\mathbf{U}_S\mathbf{R}_S^T(\mathbf{R}_S\hat{\mathbf{N}}_S^i) = \mathbf{R}_S\mathbf{U}_S\hat{\mathbf{N}}_S^i = \lambda_S^i(\mathbf{R}_S\hat{\mathbf{N}}_S^i). \tag{2.34}$$

Furthermore, we use equations $(2.27)_2$ and (2.34) to obtain the eigenvalue problem for $\mathbf{b}_S$ as

$$\mathbf{b}_S(\mathbf{R}_S\hat{\mathbf{N}}_S^i) = \mathbf{V}_S^2(\mathbf{R}_S\hat{\mathbf{N}}_S^i) = (\lambda_S^i)^2(\mathbf{R}_S\hat{\mathbf{N}}_S^i). \tag{2.35}$$

From equations (2.34) and (2.35), we can observe that both $\mathbf{V}_S$ and $\mathbf{b}_S$ have the same eigenvectors $\mathbf{R}_S\hat{\mathbf{N}}_S^i$ but their eigenvalues are λ_S^i and $(\lambda_S^i)^2$, respectively.

From the equations (2.32) - (2.35) and the section 2.3.4, we see that the eigenvectors of $\mathbf{U}_S$ and $\mathbf{C}_S$ are rotated with $\mathbf{R}_S$ to give the eigenvectors for $\mathbf{V}_S$ and $\mathbf{b}_S$. The eigenvectors $\hat{\mathbf{N}}_S^i$ in the reference configuration are rotated to give the orthogonal, and normalised eigenvectors $\hat{\mathbf{n}}_S^i \neq \mathbf{0}$ in the current configuration via

$$\hat{\mathbf{n}}_S^i = \mathbf{R}_S\hat{\mathbf{N}}_S^i. \tag{2.36}$$

As a result, the spectral decomposition of the deformation tensors can be given in the following way

$$\begin{aligned}\mathbf{U}_S^2 = \mathbf{C}_S &= \sum_{i=1}^{3} (\lambda_S^i)^2 \hat{\mathbf{N}}_S^i \otimes \hat{\mathbf{N}}_S^i, \\ \mathbf{V}_S^2 = \mathbf{b}_S &= \sum_{i=1}^{3} (\lambda_S^i)^2 \hat{\mathbf{n}}_S^i \otimes \hat{\mathbf{n}}_S^i.\end{aligned} \tag{2.37}$$

Using the equations (2.23) and (2.36), the spectral decomposition of the deformation gradient $\mathbf{F}_S$ can be given as

$$\mathbf{F}_S = \mathbf{R}_S \mathbf{U}_S = \mathbf{R}_S \sum_{i=1}^{3} \lambda_S^i \hat{\mathbf{N}}_S^i \otimes \hat{\mathbf{N}}_S^i = \sum_{i=1}^{3} \lambda_S^i (\mathbf{R}_S \hat{\mathbf{N}}_S^i) \otimes \hat{\mathbf{N}}_S^i = \sum_{i=1}^{3} \lambda_S^i \hat{\mathbf{n}}_S^i \otimes \hat{\mathbf{N}}_S^i. \tag{2.38}$$

Moreover, since unit tensor $\mathbf{I}$ can be written as $\hat{\mathbf{N}}_S \otimes \hat{\mathbf{N}}_S$, the spectral decomposition of rotation tensor $\mathbf{R}_S$ can be obtained as

$$\mathbf{R}_S = \mathbf{R}_S \mathbf{I} = (\mathbf{R}_S \hat{\mathbf{N}}_S) \otimes \hat{\mathbf{N}}_S = \sum_{i=1}^{3} \hat{\mathbf{n}}_S^i \otimes \hat{\mathbf{N}}_S^i. \tag{2.39}$$

For a non-trivial solution of eigenvalue problems in (2.33) and (2.35), the characteristic polynomial, which can be expressed using the Cayley Hamilton theorem, needs to be zero, i.e.,

$$\det(\mathbf{C}_S - (\lambda_S^i)^2 \mathbf{I}) = \det(\mathbf{b}_S - (\lambda_S^i)^2 \mathbf{I}) = III_S - (\lambda_S^i)^2 II_S + (\lambda_S^i)^4 I_S - (\lambda_S^i)^6 = 0. \tag{2.40}$$

Due to the symmetry of the deformation tensors $\mathbf{C}_S$ and $\mathbf{b}_S$, the third order characteristic polynomial, equation (2.40), yields three real-valued eigenvectors $\lambda_S^1, \lambda_S^2, \lambda_S^3$. Furthermore, we introduce the principal invariants I_S, II_S and III_S in the following way

$$\begin{aligned} I_S = I_{\mathbf{b}_S} = I_{\mathbf{C}_S} &= \operatorname{tr} \mathbf{C}_S = \mathbf{C}_S : \mathbf{I} = \mathbf{F}_S : \mathbf{F}_S, \\ II_S = II_{\mathbf{b}_S} = II_{\mathbf{C}_S} &= \operatorname{cof} \mathbf{C}_S : \mathbf{I} = \frac{1}{2}[(\operatorname{tr} \mathbf{C}_S)^2 - \operatorname{tr}(\mathbf{C}_S \cdot \mathbf{C}_S)] = \operatorname{cof} \mathbf{F}_S : \operatorname{cof} \mathbf{F}_S, \\ III_S = III_{\mathbf{b}_S} = III_{\mathbf{C}_S} &= \det \mathbf{C}_S = (\det \mathbf{F}_S)^2. \end{aligned} \tag{2.41}$$

If the eigenvalues λ_S^i are known, the principal invariants can be calculated as follows

$$\begin{aligned} I_S &= \sum_{i=1}^{3} \lambda_S^i = \lambda_S^1 + \lambda_S^2 + \lambda_S^3, \\ II_S &= \frac{1}{2} \sum_{\substack{i,j=1 \\ i \neq j}}^{3} \lambda_S^i \lambda_S^j = \lambda_S^1 \lambda_S^2 + \lambda_S^2 \lambda_S^3 + \lambda_S^3 \lambda_S^1, \\ III_S &= \prod_{i=1}^{3} \lambda_S^i = \lambda_S^1 \lambda_S^2 \lambda_S^3. \end{aligned} \tag{2.42}$$

2.3.6 Deformation and Strain Rates

In this section, we focus on the evolution of the kinematic tensor fields. We proceed with the Lagrangean representation of the velocity in equation (2.10) and obtain the material velocity gradient $\mathbf{L}_S$ as

$$\mathbf{L}_S(\mathbf{X}_S,t) = (\mathbf{F}_S)'_S(\mathbf{X}_S,t) = \frac{\partial}{\partial t}\left(\frac{\partial \boldsymbol{\chi}_S(\mathbf{X}_S,t)}{\partial \mathbf{X}_S}\right) = \frac{\partial}{\partial \mathbf{X}_S}\left(\frac{\partial \boldsymbol{\chi}_S(\mathbf{X}_S,t)}{\partial t}\right) = \mathrm{Grad}_S\,\mathbf{x}'_S. \quad (2.43)$$

Similarly, proceeding with the Eulerian description of the velocity in equation (2.11), we get the spatial velocity gradient $\boldsymbol{l}_S$ as

$$\boldsymbol{l}_S(\mathbf{x},t) = \frac{\partial \mathbf{x}'_S(\mathbf{x},t)}{\partial \mathbf{x}} = \mathrm{grad}\,\mathbf{x}'_S(\mathbf{x},t). \quad (2.44)$$

Using the equations (2.8), $(2.10)_1$, $(2.11)_1$, (2.44), and the definitions of $\mathbf{F}_S$ and $\mathbf{F}_S^{-1}$, we get

$$\boldsymbol{l}_S(\mathbf{x},t) = \frac{\partial \mathbf{x}'_S(\mathbf{x},t)}{\partial \mathbf{x}} = \underbrace{\frac{\partial}{\partial t}\left(\frac{\partial \boldsymbol{\chi}_S(\mathbf{X}_S,t)}{\partial \mathbf{X}_S}\right)}_{(\mathbf{F}_S)'_S}\underbrace{\frac{\partial \mathbf{X}_S}{\partial \mathbf{x}}}_{\mathbf{F}_S^{-1}} = (\mathbf{F}_S)'_S\mathbf{F}_S^{-1}. \quad (2.45)$$

Furthermore, we additively decompose the spatial velocity gradient $\boldsymbol{l}_S$ into the symmetric and skew-symmetric parts

$$\boldsymbol{l}_S(\mathbf{x},t) = \mathbf{d}_S(\mathbf{x},t) + \mathbf{w}_S(\mathbf{x},t), \quad (2.46)$$

where

$$\begin{aligned} \mathbf{d}_S &= \frac{1}{2}(\boldsymbol{l}_S + \boldsymbol{l}_S^T) = \frac{1}{2}(\mathrm{grad}\,\mathbf{x}'_S + \mathrm{grad}^T\,\mathbf{x}'_S) = \mathbf{d}_S^T, \\ \mathbf{w}_S &= \frac{1}{2}(\boldsymbol{l}_S - \boldsymbol{l}_S^T) = \frac{1}{2}(\mathrm{grad}\,\mathbf{x}'_S - \mathrm{grad}^T\,\mathbf{x}'_S) = -\mathbf{w}_S^T. \end{aligned} \quad (2.47)$$

$\mathbf{d}_S$ is the symmetric part and is referred to as the rate of deformation tensor (rate of strain tensor), and the skew-symmetric part $\mathbf{w}_S$ is known as the spin tensor (rate of rotation tensor or vorticity tensor). Moreover, using the equations $(2.31)_2$ and (2.44), the Green-Lagrangean strain rate can be introduced as

$$\begin{aligned} (\mathbf{E}_S)'_S &= \frac{1}{2}\big((\mathbf{F}_S^T)'_S\mathbf{F}_S + \mathbf{F}_S^T(\mathbf{F}_S)'_S\big) = \frac{1}{2}\big(\mathbf{F}_S^T\boldsymbol{l}_S^T\mathbf{F}_S + \mathbf{F}_S^T\boldsymbol{l}_S\mathbf{F}_S\big) \\ &= \mathbf{F}_S^T\frac{1}{2}\big(\boldsymbol{l}_S^T + \boldsymbol{l}_S\big)\mathbf{F}_S = \mathbf{F}_S^T\mathbf{d}_S\mathbf{F}_S. \end{aligned} \quad (2.48)$$

This gives the relation for the Cauchy-Green deformation tensor $\mathbf{C}_S$ as

$$(\mathbf{C}_S)'_S = 2(\mathbf{E}_S)'_S = 2\mathbf{F}_S^T\mathbf{d}_S\mathbf{F}_S. \quad (2.49)$$

Furthermore, the Lie time derivative for the spatial kinematic quantities can be introduced. The Lie derivative can be obtained for an arbitrary tensor field $\mathbf{h}_S$ in the current configuration via three steps using the pull-back $\mathcal{A}^*(\cdot)$ and push-forward $\mathcal{A}_*(\cdot)$ operators as

- Define the quantity in the reference configuration via pull-back operation as

$$\mathbf{H}_S = \mathcal{A}^*(\mathbf{h}). \tag{2.50}$$

- Take the time derivative in the reference configuration as

$$(\mathbf{H}_S)'_S = \frac{\mathrm{d}_S \mathbf{H}_S}{\mathrm{d}t}. \tag{2.51}$$

- Define the quantity in the current configuration via push-forward operation as

$$\mathcal{L}_{\mathbf{v}}(\mathbf{h}_S) = \mathcal{A}_*((\mathbf{H}_S)'_S). \tag{2.52}$$

The Lie derivative computes the change of $\mathbf{h}_S$ relative to the vector field $\mathbf{v}$ and is denoted by $\mathcal{L}_{\mathbf{v}}(\mathbf{h}_S)$.

Following the mentioned steps and using the equation (2.31), the Lie derivative $\mathcal{L}_{\mathbf{v}}$ for the Almansi strain $\mathbf{e}_S$ can be calculated as

- Pull-back of the Almansi strain

$$\mathbf{E}_S = \mathbf{F}_S^T(\mathbf{e}_S)\mathbf{F}_S. \tag{2.53}$$

- Time derivative in the reference configuration

$$(\mathbf{E}_S)'_S = \frac{1}{2}(\mathbf{C}_S)'_S = \frac{1}{2}(\mathbf{F}_S^T\mathbf{F}_S)'_S = \frac{1}{2}(\mathbf{F}_S^T)'_S\mathbf{F}_S + \frac{1}{2}\mathbf{F}_S^T(\mathbf{F}_S)'_S. \tag{2.54}$$

- Push-forward to the current configuration

$$\mathcal{L}_{\mathbf{v}}(\mathbf{e}_S) = \mathbf{F}_S^{-T}(\mathbf{E}_S)'_S\mathbf{F}_S^{-1} = \frac{1}{2}\left(\mathbf{F}_S^{-T}(\mathbf{F}_S^T)'_S + (\mathbf{F}_S)'_S\mathbf{F}_S^{-1}\right) = \frac{1}{2}(\boldsymbol{l}_S^T + \boldsymbol{l}_S) = \mathbf{d}_S. \tag{2.55}$$

Hence, the Lie derivative of the Almansi strain is the rate of deformation tensor $\mathbf{d}_S$.

2.3.7 Stress Measures

This section introduces the stress measures for a deformable body undergoing a finite motion. In the current configuration, the stress is defined as force per unit area. This leads to the definition of Cauchy stress, also known as true stress. Cauchy introduced it for single-phase materials, which can be directly extended to the framework of TPM.

We begin with Euler's cut principle, cf. Figure 2.4. Consider the open subdomain $\mathcal{P}_0 \subset \mathcal{B}_0$ of the reference configuration, which is deformed to $\mathcal{P}_t$ in the current configuration for a constituent φ^α. We obtain the outward normal vector $\mathbf{N}_\alpha$ and the area element $\mathrm{d}\mathbf{A}_\alpha$ on the surface of $\mathcal{P}_0$. Similarly, we get the normal vector $\mathbf{n}$ and the area element $\mathrm{d}\mathbf{a}$ on the surface of $\mathcal{P}_t$. The reference configuration is assumed to be stress-free. However, we can replace the action of the rest of the body on the subdomain $\mathcal{P}_t$ with the traction vector field defined on the surface. The traction vector $\mathbf{t}^\alpha$ is defined as the force per unit area and is assumed to be a function of the position $\mathbf{x}$, time t and a linear function of the outward normal vector $\mathbf{n}$. This is expressed by Cauchy's theorem as

$$\mathbf{t}^\alpha(\mathbf{x},t;\mathbf{n}) = \mathbf{T}^\alpha(\mathbf{x},t)\mathbf{n}, \tag{2.56}$$

where $\mathbf{T}^\alpha$ is the partial Cauchy stress tensor of a constituent φ^α in the current configuration. Following the definition of the surface traction vector and equation (2.56), for every surface element, we get

$$\mathrm{d}\mathbf{f}^\alpha = \mathbf{t}^\alpha \,\mathrm{d}a = \mathbf{T}^\alpha \mathbf{n}\,\mathrm{d}a = \mathbf{T}^\alpha \,\mathrm{d}\mathbf{a}, \tag{2.57}$$

where $\mathbf{f}^\alpha$ is the force vector in the current configuration. Hence, the Cauchy stress is called the true stress because it relates the actual force elements to the actual outward normal vector, both in the current configuration. Following this, it is convenient to introduce further stress definitions. We can define the Kirchhoff stress $\boldsymbol{\tau}^\alpha$ in the current configuration simply by scaling the Cauchy stress tensor by the Jacobian $J_\alpha = \det \mathbf{F}_\alpha$ as

$$\boldsymbol{\tau}^\alpha := J_\alpha \mathbf{T}^\alpha. \tag{2.58}$$

Furthermore, the first Piola-Kirchhoff stress $\mathbf{P}^\alpha$ can be defined. The idea is to associate the force in the current configuration with the area in the reference configuration. Using equations (2.57) and $(2.18)_1$, we get

$$\mathrm{d}\mathbf{f}^\alpha = \mathbf{T}^\alpha \,\mathrm{d}\mathbf{a} = \mathbf{T}^\alpha \operatorname{cof}\mathbf{F}_\alpha \,\mathrm{d}\mathbf{A}_\alpha = \underbrace{\mathbf{T}^\alpha \det\mathbf{F}_\alpha \mathbf{F}_\alpha^{-T}}_{\mathbf{P}^\alpha} \mathrm{d}\mathbf{A}_\alpha = \mathbf{P}^\alpha \,\mathrm{d}\mathbf{A}_\alpha, \tag{2.59}$$

where

$$\mathbf{P}^\alpha = \mathbf{T}^\alpha \det\mathbf{F}_\alpha \mathbf{F}_\alpha^{-T} = \boldsymbol{\tau}^\alpha \mathbf{F}_\alpha^{-T}. \tag{2.60}$$

The first Piola-Kirchhoff stress is significant from experiments point of view, where the forces are related to the undeformed surfaces. Since we have stress measures in the actual

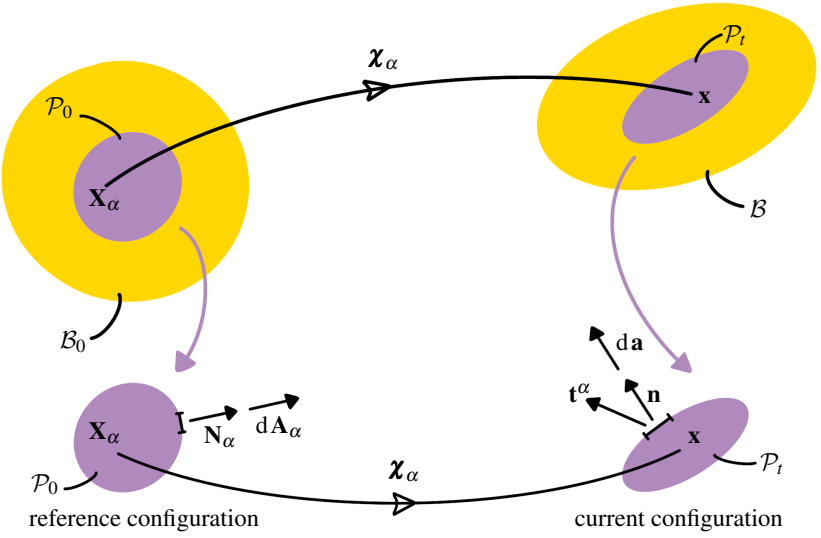

Figure 2.4: Euler's cut principle.

configuration ($\mathbf{T}^\alpha$ and $\boldsymbol{\tau}^\alpha$) and two-field stress measure ($\mathbf{P}^\alpha$), we will now introduce the second Piola-Kirchhoff stress $\mathbf{S}^\alpha$ in the reference configuration, which is a pull-back of Kirchhoff stress

$$\mathbf{S}^\alpha := \mathbf{F}_\alpha^{-1}\boldsymbol{\tau}^\alpha\mathbf{F}^{-T}. \tag{2.61}$$

2.4 Balance Relations for Porous Media

The following section briefly overviews the balance relations used in the TPM. We can write the balance relations for the multi-phase materials in analogy to the mechanics of single-phase materials. The formulation of the balance principles for the multi-phase materials is based on Truesdell's metaphysical principles [69] of mixture theories:

1. All properties of the mixture must be mathematical consequences of properties of the constituents.

2. So as to describe the motion of a constituent, we may in imagination isolate it from the rest of the mixture, provided we allow properly for the actions of the other constituents upon it.

3. The motion of the mixture is governed by the same equations as in a single body.

Following this, we must describe each constituent φ^α by individual motion functions and balance equations and account for the possible interactions between the constituents by introducing production terms. Moreover, the mixture (overall aggregate) φ balance equations are obtained by summation of the balance equations of all the constituents. Hence, they have the same structure as the balance equations of single-phase materials.

In this context, we can briefly introduce the master balance principle from the single-phase materials and extend it to the constituents as well as the overall aggregate. The reader is referred to Ehlers [39], de Boer [5], Truesdell [69], and Holzapfel [3] for more information.

2.4.1 Aggregate Balance Relations

To obtain the local balance relations for the aggregate φ, one starts with the mass balance before evaluating higher balance equations. The higher balances are simplified by inserting the lower balance equations. The balance equations can be formulated following the five-step procedure as

- Formulate the balance laws in the current configuration where the physics happens.
- Pull-back the formulation to the reference configuration to obtain the time-independent integration domain.
- Take the time derivative in the reference configuration.
- Push-forward the result to the current configuration.
- Apply the localisation theorem to obtain the local representation of the balance laws.

However, in this section, we provide the general structure of the balance laws. Proceeding from the classical continuum mechanics of single-phase materials, the integral master balance relations for aggregate body $\mathcal{B}$ can be presented as

$$\begin{aligned} \frac{\mathrm{d}}{\mathrm{d}t}\int_{\mathcal{B}} \Psi \,\mathrm{d}v &= \int_{\mathcal{S}} (\boldsymbol{\phi}\cdot\mathbf{n})\,\mathrm{d}a + \int_{\mathcal{B}} \sigma \,\mathrm{d}v + \int_{\mathcal{B}} \hat{\Psi}\,\mathrm{d}v, \\ \frac{\mathrm{d}}{\mathrm{d}t}\int_{\mathcal{B}} \boldsymbol{\Psi} \,\mathrm{d}v &= \int_{\mathcal{S}} (\boldsymbol{\Phi}\mathbf{n})\,\mathrm{d}a + \int_{\mathcal{B}} \boldsymbol{\sigma} \,\mathrm{d}v + \int_{\mathcal{B}} \hat{\boldsymbol{\Psi}}\,\mathrm{d}v. \end{aligned} \tag{2.62}$$

From the general thermodynamic framework, Ψ or $\boldsymbol{\Psi}$ are volume-specific scalar- and vector-valued densities of mechanical quantities that have to be balanced in the overall aggregate φ. These quantities are given by the mass density, the linear momentum, the moment of momentum, the total energy (internal and kinetic) and the entropy. The quantities $\boldsymbol{\phi}\cdot\mathbf{n}$ or $\boldsymbol{\Phi}\mathbf{n}$ represent the effluxes of the mechanical quantities defined per unit current

area, which directly enter the aggregate body $\mathcal{B}$ over its surface $\mathcal{S}$ from the external vicinity. $\mathbf{n}$ is the outward-oriented normal vector to the surface $\mathcal{S}$ and at point $\mathbf{x}$. σ or $\boldsymbol{\sigma}$ are the supply terms of external mechanical quantities defined per unit volume, resulting from a distance. $\hat{\Psi}$ or $\hat{\boldsymbol{\Psi}}$ are the production terms allowing for a possible coupling of φ with its surroundings.

We can now obtain the local balance relations from the master balance relations, provided the integrands are steady and steadily differentiable. On transforming the surface integrals on the right-hand side in (2.62) into the volume integrals, and applying the localisation theorem, we can obtain the local balance relations

$$\begin{aligned} \dot{\Psi} + \Psi \operatorname{div} \dot{\mathbf{x}} &= \operatorname{div} \boldsymbol{\phi} + \sigma + \hat{\Psi}, \\ \dot{\boldsymbol{\Psi}} + \boldsymbol{\Psi} \operatorname{div} \dot{\mathbf{x}} &= \operatorname{div} \boldsymbol{\Phi} + \boldsymbol{\sigma} + \hat{\boldsymbol{\Psi}}, \end{aligned} \tag{2.63}$$

where $\dot{(\cdot)}$ represents the material time derivative for the aggregate. The specific balance principles, i.e., the balance of mechanical (mass, momentum, moment of momentum) and thermodynamical quantities (energy and entropy) of the deforming body $\mathcal{B}$, which apply to any material and must be satisfied at all times, can be represented as

	$\Psi, \boldsymbol{\Psi}$	$\boldsymbol{\phi}, \boldsymbol{\Phi}$	$\sigma, \boldsymbol{\sigma}$	$\hat{\Psi}, \hat{\boldsymbol{\Psi}}$
mass	ρ	$\mathbf{0}$	0	0
momentum	$\rho \dot{\mathbf{x}}$	$\mathbf{T}$	$\rho \mathbf{b}$	0
m.o.m.	$\mathbf{x} \times (\rho \dot{\mathbf{x}})$	$\mathbf{x} \times \mathbf{T}$	$\mathbf{x} \times (\rho \mathbf{b})$	0
energy	$\rho \varepsilon + \frac{1}{2} \dot{\mathbf{x}} \cdot (\rho \dot{\mathbf{x}})$	$\mathbf{T}^T \dot{\mathbf{x}} - \mathbf{q}$	$\dot{\mathbf{x}} \cdot (\rho \mathbf{b}) + \rho r$	0
entropy	$\rho \eta$	$\boldsymbol{\phi}_\eta$	σ_η	$\hat{\eta} \geq 0$

(2.64)

Here, $\rho \dot{\mathbf{x}}$ is the momentum of the aggregate, $\mathbf{T}$ is the Cauchy stress tensor, and $\mathbf{b}$ is the external volume force per unit mass. $\mathbf{x} \times (\rho \dot{\mathbf{x}})$ yields the moment of momentum, while ε denotes the internal energy of the aggregate. Moreover, $\mathbf{q}$ is the heat influx vector, and r is the external heat supply. η is the entropy, and $\boldsymbol{\phi}_\eta$ and σ_η denote the efflux of entropy and the external entropy supply, respectively. $\hat{\eta}$ is the entropy production which can never be negative ($\hat{\eta} \geq 0$) following the second law of thermodynamics. Furthermore, we can insert the specific balance relations (2.64) in the local master balances (2.63). This gives us the standard local balance equations for the single-phase materials and the aggregate φ

in agreement with Truesdell's third metaphysical principle as

$$\begin{aligned}
\text{mass}: &\quad \dot{\rho} + \rho \operatorname{div} \dot{\mathbf{x}} = 0, \\
\text{momentum}: &\quad \rho \ddot{\mathbf{x}} = \operatorname{div} \mathbf{T} + \rho \mathbf{b}, \\
\text{m.o.m.}: &\quad \mathbf{0} = \mathbf{I} \times \mathbf{T} \quad \rightarrow \quad \mathbf{T} = \mathbf{T}^{\mathrm{T}}, \\
\text{energy}: &\quad \rho \dot{\varepsilon} = \mathbf{T} : \boldsymbol{l} - \operatorname{div} \mathbf{q} + \rho r, \\
\text{entropy}: &\quad \rho \dot{\eta} \geq \operatorname{div} \boldsymbol{\phi}_{\eta} + \sigma_{\eta}.
\end{aligned} \tag{2.65}$$

One should note that, as a result of the moment of momentum balance, we get the symmetric Cauchy stress tensor.

2.4.2 Constituent Balance Relations

We can obtain the master balance relations for the constituents φ^{α} in analogy to (2.62) following Truesdell's second metaphysical principle as

$$\begin{aligned}
\frac{\mathrm{d}_{\alpha}}{\mathrm{d}t} \int_{\mathcal{B}} \Psi^{\alpha} \, \mathrm{d}v &= \int_{\mathcal{S}} (\boldsymbol{\phi}^{\alpha} \cdot \mathbf{n}) \, \mathrm{d}a + \int_{\mathcal{B}} \sigma^{\alpha} \, \mathrm{d}v + \int_{\mathcal{B}} \hat{\Psi}^{\alpha} \, \mathrm{d}v, \\
\frac{\mathrm{d}_{\alpha}}{\mathrm{d}t} \int_{\mathcal{B}} \boldsymbol{\Psi}^{\alpha} \, \mathrm{d}v &= \int_{\mathcal{S}} (\boldsymbol{\Phi}^{\alpha} \mathbf{n}) \, \mathrm{d}a + \int_{\mathcal{B}} \boldsymbol{\sigma}^{\alpha} \, \mathrm{d}v + \int_{\mathcal{B}} \hat{\boldsymbol{\Psi}}^{\alpha} \, \mathrm{d}v.
\end{aligned} \tag{2.66}$$

Here, the partial quantities $(\cdot)^{\alpha}$ have the same physical meaning as in (2.62). The local master balance relations for the constituents can be obtained in a similar way as (2.63)

$$\begin{aligned}
(\Psi^{\alpha})'_{\alpha} + \Psi^{\alpha} \operatorname{div} \mathbf{x}'_{\alpha} &= \operatorname{div} \boldsymbol{\phi}^{\alpha} + \sigma^{\alpha} + \hat{\Psi}^{\alpha}, \\
(\boldsymbol{\Psi}^{\alpha})'_{\alpha} + \boldsymbol{\Psi}^{\alpha} \operatorname{div} \mathbf{x}'_{\alpha} &= \operatorname{div} \boldsymbol{\Phi}^{\alpha} + \boldsymbol{\sigma}^{\alpha} + \hat{\boldsymbol{\Psi}}^{\alpha}.
\end{aligned} \tag{2.67}$$

Equation (2.63) gives the balance relations for the overall aggregate following the classical continuum mechanics of single-phase materials. From Truesdell's first metaphysical principle, we can obtain these relations by the sum of the balance relations (2.67) over all the constituents φ^{α}. Therefore, this leads to the following summation constraints for scalar- and vector-valued quantities Ψ and $\boldsymbol{\Psi}$

$$\begin{aligned}
\text{quantity}: \Psi &= \sum_{\alpha} \Psi^{\alpha}, & \boldsymbol{\Psi} &= \sum_{\alpha} \boldsymbol{\Psi}^{\alpha}, \\
\text{efflux}: \boldsymbol{\phi} \cdot \mathbf{n} &= \sum_{\alpha} (\boldsymbol{\phi}^{\alpha} - \Psi^{\alpha} \mathbf{v}_{\alpha}) \cdot \mathbf{n}, & \boldsymbol{\Phi} \mathbf{n} &= \sum_{\alpha} (\boldsymbol{\Phi}^{\alpha} - \boldsymbol{\Psi}^{\alpha} \otimes \mathbf{v}_{\alpha}) \mathbf{n} \\
\text{supply}: \sigma &= \sum_{\alpha} \sigma^{\alpha}, & \boldsymbol{\sigma} &= \sum_{\alpha} \boldsymbol{\sigma}^{\alpha}, \\
\text{production}: \hat{\Psi} &= \sum_{\alpha} \hat{\Psi}^{\alpha}, & \hat{\boldsymbol{\Psi}} &= \sum_{\alpha} \hat{\boldsymbol{\Psi}}^{\alpha}.
\end{aligned} \tag{2.68}$$

On comparing the divergence terms in (2.63) and (2.67), we obtain the additional diffusion velocity term in $(2.68)_2$. We can formulate the specific balance equations for the constituents φ^α directly in analogy to the single-phase materials in (2.64) as

	$\Psi^\alpha, \boldsymbol{\Psi}^\alpha$	$\boldsymbol{\phi}^\alpha, \boldsymbol{\Phi}^\alpha$	$\sigma^\alpha, \boldsymbol{\sigma}^\alpha$	$\hat{\Psi}^\alpha, \hat{\boldsymbol{\Psi}}^\alpha$
mass	ρ^α	$\mathbf{0}$	0	$\hat{\rho}^\alpha$
momentum	$\rho^\alpha \mathbf{x}'_\alpha$	$\mathbf{T}^\alpha$	$\rho^\alpha \mathbf{b}^\alpha$	$\hat{\mathbf{s}}^\alpha$
m.o.m.	$\mathbf{x} \times (\rho^\alpha \mathbf{x}'_\alpha)$	$\mathbf{x} \times \mathbf{T}^\alpha$	$\mathbf{x} \times (\rho^\alpha \mathbf{b}^\alpha)$	$\hat{\mathbf{h}}^\alpha$
energy	$\rho^\alpha \varepsilon^\alpha + \frac{1}{2}\mathbf{x}'_\alpha \cdot (\rho^\alpha \mathbf{x}'_\alpha)$	$(\mathbf{T}^\alpha)^T \mathbf{x}'_\alpha - \mathbf{q}^\alpha$	$\mathbf{x}'_\alpha \cdot (\rho^\alpha \mathbf{b}^\alpha) + \rho^\alpha r^\alpha$	$\hat{e}^\alpha$
entropy	$\rho^\alpha \eta^\alpha$	$\boldsymbol{\phi}^\alpha_\eta$	σ^α_η	$\hat{\eta}^\alpha$

(2.69)

Here, $\hat{\rho}^\alpha$ represents the total mass production term, allowing for mass exchange or phase transition among the constituents φ^α. $\hat{\mathbf{s}}^\alpha$ is the total momentum production, and $\hat{\mathbf{h}}^\alpha$ denotes the total moment of momentum production. $\hat{e}^\alpha$ and $\hat{\eta}^\alpha$ are the total energy and entropy productions, respectively. On summing the specific balance relations of the constituents (2.69), using the equations (2.68), and comparing the results with the specific balance relations of the aggregate φ, we get the following summation constraints for the total production terms

$$\sum_\alpha \hat{\rho}^\alpha = 0, \qquad \sum_\alpha \hat{\mathbf{s}}^\alpha = \mathbf{0}, \qquad \sum_\alpha \hat{\mathbf{h}}^\alpha = \mathbf{0}, \qquad \sum_\alpha \hat{e}^\alpha = 0, \qquad \sum_\alpha \hat{\eta}^\alpha \geq 0. \tag{2.70}$$

From the framework of single-phase materials, we can write the efflux and the supply of the entropy of the constituents φ^α as

$$\boldsymbol{\phi}^\alpha_\eta = \frac{1}{\Theta^\alpha}\mathbf{q}^\alpha, \qquad \sigma^\alpha_\eta = \frac{1}{\Theta^\alpha}\rho^\alpha r^\alpha, \tag{2.71}$$

where $\Theta^\alpha > 0$ allows for different Kelvin temperatures for each constituent. Now, inserting the specific balance relations (2.69) into the local master balance relations (2.67) of the constituents φ^α and using the lower balance relations for deriving the higher balances, we obtain the following equations for non-polar constituents

$$\begin{aligned}
\text{mass :} \quad & (\rho^\alpha)'_\alpha + \rho^\alpha \operatorname{div} \mathbf{x}'_\alpha = \hat{\rho}^\alpha, \\
\text{momentum :} \quad & \rho^\alpha \mathbf{x}''_\alpha = \operatorname{div} \mathbf{T}^\alpha + \rho^\alpha \mathbf{b}^\alpha + \hat{\mathbf{p}}^\alpha, \\
\text{m.o.m. :} \quad & \mathbf{0} = \mathbf{I} \times \mathbf{T}^\alpha \quad \rightarrow \quad \mathbf{T}^\alpha = (\mathbf{T}^\alpha)^T, \\
\text{energy :} \quad & \rho^\alpha (\varepsilon^\alpha)'_\alpha = \mathbf{T}^\alpha : \boldsymbol{l}_\alpha - \operatorname{div} \mathbf{q}^\alpha + \rho^\alpha r^\alpha + \hat{\varepsilon}^\alpha, \\
\text{entropy :} \quad & \rho^\alpha (\eta^\alpha)'_\alpha = \operatorname{div}\big(-\frac{1}{\Theta}\mathbf{q}^\alpha\big) + \frac{1}{\Theta^\alpha}\rho^\alpha r^\alpha + \hat{\zeta}^\alpha.
\end{aligned} \tag{2.72}$$

In the framework of the mixture theories, the total production terms can be split into direct and additional production terms and give the following relations

$$\begin{aligned}
&\hat{\mathbf{s}}^\alpha = \hat{\mathbf{p}}^\alpha + \hat{\rho}^\alpha \mathbf{x}'_\alpha, && \hat{\mathbf{h}}^\alpha = \mathbf{x} \times \hat{\mathbf{s}}^\alpha, \\
&\hat{e}^\alpha = \hat{\varepsilon}^\alpha + \hat{\mathbf{p}}^\alpha \cdot \mathbf{x}'_\alpha + \hat{\rho}^\alpha (\varepsilon^\alpha + \frac{1}{2}\mathbf{x}'_\alpha \cdot \mathbf{x}'_\alpha), && \hat{\eta}^\alpha = \hat{\zeta}^\alpha + \hat{\rho}^\alpha \eta^\alpha.
\end{aligned} \tag{2.73}$$

The direct momentum production term $\hat{\mathbf{p}}^\alpha$ results from the interaction force between the constituents φ^α. The second part $\hat{\rho}^\alpha \mathbf{x}'_\alpha$ represents the momentum production due to the mass exchange. Furthermore, $\hat{\mathbf{h}}^\alpha$ is the total production of the moment of momentum, accounting for the production of angular momentum from the mass exchange and the direct moment production. Similarly, $\hat{e}^\alpha$ and $\hat{\xi}^\alpha$ are the direct production terms of energy and entropy, respectively. The derivations of the balance equations for non-polar constituents can be found in Appendix A.1.

2.4.3 Entropy Principle

In a thermodynamic process, the first law of thermodynamics is responsible for energy transfer. However, it has no information on the direction of the energy transfer. The entropy balance, together with the second law of thermodynamics (governs the direction of energy transfer), gives the entropy principle. The entropy principle provides us with the restriction, which plays an essential role in the constitutive modelling of a material. We get the entropy principle by restricting the total entropy production in $(2.73)_4$ via the relation $(2.70)_5$ and using the specific entropy balance of the constituents $(2.72)_5$ as

$$\hat{\eta} = \sum_\alpha \hat{\eta}^\alpha = \sum_\alpha \Big[\rho^\alpha (\eta^\alpha)'_\alpha + \hat{\rho}^\alpha \eta^\alpha + \operatorname{div}\Big(\frac{1}{\Theta^\alpha} \mathbf{q}^\alpha \Big) - \frac{1}{\Theta^\alpha} \rho^\alpha r^\alpha \Big] \geq 0. \tag{2.74}$$

Following this, we use the Legendre transformation between the entropy and its conjugate variable, the temperature and introduce the Helmholtz free energy density ψ^α as

$$\psi^\alpha := \varepsilon^\alpha - \Theta^\alpha \eta^\alpha \tag{2.75}$$

Furthermore, the lower balance relations of the constituents $(2.72)_{1-3}$ along with the equation (2.75) gives the Clausius-Duhem representation of the entropy inequality

$$\begin{aligned} \mathcal{D} = \sum_\alpha \frac{1}{\Theta^\alpha} \Big\{ \mathbf{T}^\alpha : \boldsymbol{l}_\alpha - \rho^\alpha \big[(\psi^\alpha)'_\alpha + (\Theta^\alpha)'_\alpha \eta^\alpha \big] - \hat{\mathbf{p}}^\alpha \cdot \mathbf{x}'_\alpha - \\ - \hat{\rho}^\alpha (\psi^\alpha + \frac{1}{2} \mathbf{x}'_\alpha \cdot \mathbf{x}'_\alpha) - \frac{1}{\Theta^\alpha} \mathbf{q}^\alpha \cdot \operatorname{grad} \Theta^\alpha + \hat{e}^\alpha \Big\} \geq 0. \end{aligned} \tag{2.76}$$

This equation is essential for developing a thermodynamically consistent model.

3 CONSTITUTIVE MODELLING

In the previous chapter, we presented kinematics and balance relations. However, these do not provide enough equations to determine all the unknown quantities. As a result, further constitutive equations need to be developed to close the model. Therefore, we consider the characteristics of the model and thrombosis, and consequently present the assumptions to simplify the balance equations of the constituents accordingly. Moreover, we evaluate the entropy inequality to provide the necessary restrictions to develop the missing constitutive equations for a thermodynamically consistent model.

3.1 Saturated Triphasic TPM Model

This section aims to specify the balance equations presented in Section 2.4 by giving the assumptions for the saturated triphasic porous media.

3.1.1 Preliminaries and Assumptions

At first, we introduce meaningful assumptions to be able to adapt the model according to the theoretical background. This also leads to simplifying the modelling approach to a reasonable scope. In this context, we introduce the following assumptions for the triphasic aggregate φ and its constituents φ^α.

• We assume the aggregate to be fully saturated to prevent the development of vacant space in the overall aggregate

$$n^S + \underbrace{n^L + n^N}_{n^F} = 1. \tag{3.1}$$

• The constituents are assumed to be materially incompressible. This implies that the realistic densities of the constituents $\rho^{\alpha R}$ are constant. However, material incompressibility does not lead to bulk incompressibility because the partial densities ρ^α can still change due to changes in volume fractions following the equation (2.6)

$$\rho^{\alpha R} = \text{constant}, \quad (\rho^{\alpha R})'_\alpha = 0. \tag{3.2}$$

• Quasi-static conditions (slow deformations) are assumed for the aggregate as well as the constituents

$$\mathbf{x}''_\alpha \equiv \mathbf{0}, \quad \ddot{\mathbf{x}} \equiv \mathbf{0}. \tag{3.3}$$

• A uniform temperature for all the constituents is considered. Due to isothermal conditions, the energy balance in the set of governing equations is needless and is not used explicitly

$$\Theta^\alpha \equiv \Theta = \text{constant}. \tag{3.4}$$

• We consider a uniform body force for all the constituents

$$\mathbf{b}^{\alpha} = \mathbf{b}. \tag{3.5}$$

• Non-polar constituents are considered which gives the symmetric stress tensor

$$\mathbf{T}^{\alpha} = (\mathbf{T}^{\alpha})^{T}. \tag{3.6}$$

• Both liquid and nutrients are assumed to be in the fluid phase. Therefore, we assign both phases the same velocity $\mathbf{x}'_{\alpha}$ as fluid

$$\mathbf{x}'_{N} = \mathbf{x}'_{L} = \mathbf{x}'_{F}. \tag{3.7}$$

• We assume that the liquid phase is not involved in the mass exchange. Consequently, the mass exchange occurs between the solid and the nutrient phase. This assumption, along with the equation $(2.70)_1$ gives

$$\hat{\rho}^{L} = 0 \quad \rightarrow \quad \hat{\rho}^{S} = -\hat{\rho}^{N}. \tag{3.8}$$

Furthermore, energy transfer due to chemical reactions is neglected, the diffusion velocity is neglected, and the internal structure of the thrombus is considered to be isotropic.

3.1.2 Volume Balances

Volume Balance of the Mixture

Initially, we extend the relation (2.6) to the total mass production term $\hat{\rho}^{\alpha}$ as

$$\hat{\rho}^{\alpha} = \hat{n}^{\alpha} \rho^{\alpha R}. \tag{3.9}$$

Furthermore, the local mass balance of the constituents $(2.72)_1$ can be reformulated to the local volume balance using the assumption (3.2), relation (2.6), and (3.9) as

$$(n^{\alpha})'_{\alpha} + n^{\alpha} \operatorname{div} \mathbf{x}'_{\alpha} = \hat{n}^{\alpha}. \tag{3.10}$$

Following this, we get the volume balance for each constituent φ^{α} as

$$(n^{S})'_{S} + n^{S} \operatorname{div} \mathbf{x}'_{S} = \hat{n}^{S}, \quad (n^{L})'_{L} + n^{L} \operatorname{div} \mathbf{x}'_{L} = \hat{n}^{L}, \quad (n^{N})'_{N} + n^{N} \operatorname{div} \mathbf{x}'_{N} = \hat{n}^{N}. \tag{3.11}$$

Moreover, using the material time derivative (2.14) of a scalar quantity γ, definition of the seepage velocity $(2.15)_2$, and assumption (3.7), we get

$$\left.\begin{aligned} \gamma_{S}{}' &= \frac{\partial \gamma}{\partial t} + \operatorname{grad} \gamma \cdot \mathbf{x}'_{S}, \\ \gamma_{L}{}' &= \frac{\partial \gamma}{\partial t} + \operatorname{grad} \gamma \cdot \mathbf{x}'_{L}, \end{aligned}\right\} \qquad \longrightarrow \qquad \gamma_{L}{}' = \gamma_{S}{}' + \operatorname{grad} \gamma \cdot \underbrace{(\mathbf{x}'_{L} - \mathbf{x}'_{S})}_{\mathbf{w}_{FS}}. \tag{3.12}$$

Similarly, we use the assumption $(3.7)_1$ to obtain

$$\gamma_N{}' = \gamma_S{}' + \operatorname{grad}\gamma \cdot \underbrace{(\mathbf{x}'_N - \mathbf{x}'_S)}_{\mathbf{w}_{FS}} \tag{3.13}$$

We can further get the following relation from the saturation condition (2.4)

$$n^S + n^L + n^N = 1 \qquad \longrightarrow \qquad (n^S + n^L + n^N)'_S = 0. \tag{3.14}$$

Furthermore, on summing the volume balance of all the constituents (3.11) and using relations (3.12), (3.13), and (3.14), we get

$$\operatorname{grad} n^L \cdot (\mathbf{x}'_L - \mathbf{x}'_S) + \operatorname{grad} n^N \cdot (\mathbf{x}'_N - \mathbf{x}'_S) + n^S \operatorname{div} \mathbf{x}'_S + n^L \operatorname{div} \mathbf{x}'_L + n^N \operatorname{div} \mathbf{x}'_N = \sum_\alpha \hat{n}^\alpha. \tag{3.15}$$

Now, we use the rules for gradient and divergence operators and rearrange the terms

$$\operatorname{div}(n^L \mathbf{w}_{FS}) + \operatorname{div}(n^N \mathbf{w}_{FS}) + \operatorname{div} \mathbf{x}'_S = \sum_\alpha \hat{n}^\alpha. \tag{3.16}$$

Finally, we use the equation (3.9) to get the volume balance of the mixture as

$$\operatorname{div}(\mathbf{x}'_S + n^F \mathbf{w}_{FS}) + \hat{\rho}^S \left(\frac{1}{\rho^{NR}} - \frac{1}{\rho^{SR}} \right) = 0, \tag{3.17}$$

where $n^F = n^L + n^N$.

Volume Balance of the Solid

In order to use the concept of volume fractions for identifying the regions with thrombus formation, we introduce the volume balance of solid using $(3.11)_1$ as

$$(n^S)'_S + n^S \operatorname{div} \mathbf{x}'_S = \hat{n}^S. \tag{3.18}$$

Volume Balance of the Nutrients

Similarly, we can introduce the volume balance of nutrients using the equation $(3.11)_3$

$$(n^N)'_N + n^N \operatorname{div} \mathbf{x}'_N = \hat{n}^N. \tag{3.19}$$

Now, using the equation (3.13), the above equation can be reformulated to obtain the volume balance of nutrients as

$$(n^N)'_S + \operatorname{div}(n^N \mathbf{w}_{FS}) + n^N \operatorname{div} \mathbf{x}'_S = \hat{n}^N. \tag{3.20}$$

Momentum Balance of the Mixture

The momentum balance equations for the constituents φ^α can be directly formulated from the equations (2.72) and (2.73) as

$$\rho^\alpha \mathbf{x}''_\alpha = \operatorname{div} \mathbf{T}^\alpha + \rho^\alpha \mathbf{b}^\alpha + \hat{\mathbf{p}}^\alpha. \tag{3.21}$$

Now, using the quasi-static assumptions (3.3) and (3.5), we obtain the individual momentum balance for each constituent

$$\begin{aligned} &\operatorname{div} \mathbf{T}^S + \rho^S \mathbf{b} + \hat{\mathbf{p}}^S = \mathbf{0}, \\ &\operatorname{div} \mathbf{T}^L + \rho^L \mathbf{b} + \hat{\mathbf{p}}^L = \mathbf{0}, \\ &\operatorname{div} \mathbf{T}^N + \rho^N \mathbf{b} + \hat{\mathbf{p}}^N = \mathbf{0}. \end{aligned} \tag{3.22}$$

Furthermore, we use the summation constraint for the total production of momentum $(2.70)_2$, velocity assumption (3.7), and the mass production constraint (3.8)

$$\sum_\alpha \hat{\mathbf{p}}^\alpha = \sum_\alpha (\hat{\mathbf{s}}^\alpha - \hat{\rho}^\alpha \mathbf{x}'_\alpha) = \hat{\rho}^S \mathbf{w}_{FS}. \tag{3.23}$$

We can now sum up the momentum balance of all the constituents (3.22) to obtain the momentum balance of the mixture as

$$\operatorname{div}(\mathbf{T}^S + \mathbf{T}^L + \mathbf{T}^N) + (\rho^S + \rho^L + \rho^N)\mathbf{b} + \hat{\rho}^S \mathbf{w}_{FS} = \mathbf{0}. \tag{3.24}$$

3.1.3 Entropy Inequality

We have the Clausius-Duhem representation of the entropy inequality from equation (2.76) and symmetric partial stresses (3.6)

$$\begin{aligned} \mathcal{D} = \sum_\alpha \frac{1}{\Theta^\alpha} \Big\{ &\mathbf{T}^\alpha : \mathbf{d}_\alpha - \rho^\alpha \big[(\psi^\alpha)'_\alpha + (\Theta^\alpha)'_\alpha \eta^\alpha \big] - \hat{\mathbf{p}}^\alpha \cdot \mathbf{x}'_\alpha - \\ &- \hat{\rho}^\alpha (\psi^\alpha + \frac{1}{2} \mathbf{x}'_\alpha \cdot \mathbf{x}'_\alpha) - \frac{1}{\Theta^\alpha} \mathbf{q}^\alpha \cdot \operatorname{grad} \Theta^\alpha + \hat{e}^\alpha \Big\} \geq 0. \end{aligned} \tag{3.25}$$

For the isothermal conditions (3.4), heat influx ($\mathbf{q}^\alpha = \mathbf{0}$), and the vanishing total energy production (2.70), the Clausius-Duhem inequality reduces to the local part giving the Clausius-Planck inequality as

$$\sum_\alpha \Big[\mathbf{T}^\alpha : \mathbf{d}_\alpha - \rho^\alpha (\psi^\alpha)'_\alpha - \hat{\mathbf{p}}^\alpha \cdot \mathbf{x}'_\alpha - \hat{\rho}^\alpha (\psi^\alpha + \frac{1}{2} \mathbf{x}'_\alpha \cdot \mathbf{x}'_\alpha) \Big] \geq 0. \tag{3.26}$$

3.2 Thermodynamic Principles

After introducing the adapted balance relations, we have to formulate constitutive relations to characterise the material behaviour. Therefore, we must take care that none of the constitutive relations violates these principles to develop a thermodynamically consistent model. Thus, we briefly overview the fundamental principles of determinism, local action, equipresence, material frame indifference, and universal dissipation from the work of Coleman & Noll [70], Noll [71, 72], Tuesdell [73], and Ehlers [39].

3.2.1 Determinism, Equipresence and Local Action

Following the principle of determinism, we determine the following set of response functions uniquely defined at any time

$$\mathcal{R} = \left\{ \psi^\alpha, \mathbf{T}^\alpha, \hat{\mathbf{p}}^\alpha, \hat{\rho}^\alpha \right\}. \tag{3.27}$$

According to the principle of equipresence, the response functions depend on the same set of process variables

$$\mathcal{V} = \left\{ \mathbf{F}_S,\, \mathrm{Grad}_S \mathbf{F}_S,\, n^\alpha,\, \mathrm{grad}\, n^\alpha,\, \mathbf{w}_{FS}, J_\alpha \right\}. \tag{3.28}$$

Furthermore, Ehlers [39] introduce the principle of phase separation where the free energy function ψ^α of a given constituent φ^α depends on the non-dissipative process variables of the respective constituent, i.e., the velocities are excluded. Also, according to the principle of local action, the constitutive response at a point can be formulated using first-grade, second-grade or higher-order theories. Following Bowen [48], the second-grade character applies only to the production terms eliminating $\mathrm{Grad}_S \mathbf{F}_S$. However, to restrict the complexity to a reasonable scope, the following dependencies for the Helmholtz free energy function ψ^α are chosen

$$\psi^S = \psi^S(\mathbf{F}_S, n^S), \qquad \psi^L = \psi^L(n^L), \qquad \psi^N = \psi^N(n^N). \tag{3.29}$$

3.2.2 Material Frame Indifference

The principle of material frame indifference, also known as the principle of objectivity, is an essential part of non-linear continuum mechanics. This principle means that the material properties of the body and the constitutive equations should not depend on the position of the observer and must be invariant with respect to the rigid body motion superimposed on the current configuration. In this context, we introduce $\overset{+}{\chi}_\alpha$ as the rigid body motion function and $\overset{*}{\chi}_\alpha$ as the superimposed rigid body motion function, cf. Figure 3.1, where

$$\overset{+}{\mathbf{x}} = \overset{+}{\chi}_\alpha(\mathbf{x}, t) = \mathbf{c}(t) + \mathbf{Q}(t)\mathbf{x} \qquad \text{and} \qquad \overset{*}{\chi}_\alpha = \overset{+}{\chi}_\alpha \circ \chi_\alpha, \tag{3.30}$$

where $\mathbf{c}$ is the superimposed rigid body translation for which any material point move in an identical way. Also, the orientation is preserved as $\mathbf{Q}$ is a proper orthogonal rotation tensor

$$\det \mathbf{Q} = +1, \qquad \text{and} \qquad \mathbf{Q}^{-1} = \mathbf{Q}^T \qquad \forall\, \mathbf{Q} \in \mathcal{SO}_3. \tag{3.31}$$

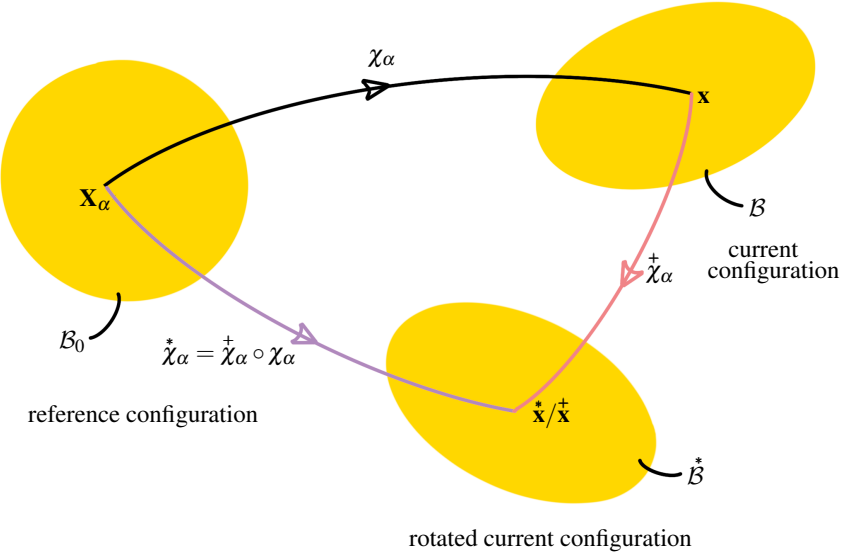

Figure 3.1: Principle of material frame indifference

Following equation $(3.30)_1$, we consider another point $\overset{+}{\mathbf{y}}$ in a similar way. This gives us the transformation rule for a spatial vector as

$$\overset{+}{\mathbf{u}} = \overset{+}{\mathbf{y}} - \overset{+}{\mathbf{x}} = \mathbf{c}(t) + \mathbf{Q}(t)(\mathbf{y} - \mathbf{x}) - \mathbf{c}(t) = \mathbf{Q}(t)\mathbf{u}, \tag{3.32}$$

where $\mathbf{u}$ and $\overset{+}{\mathbf{u}}$ are the displacement vectors in the current and rotated current configurations, respectively. On differentiating equation $(3.30)_1$, we get the relation for rotated line elements as

$$\frac{\partial \overset{+}{\mathbf{x}}}{\partial \mathbf{x}} = \frac{\partial \overset{*}{\mathbf{x}}}{\partial \mathbf{x}} = \mathbf{Q}. \tag{3.33}$$

One should note that the quantities in the reference configuration are a priori invariant for the rotations of the current configuration. Following the equation (3.33), we obtain the relationship between the deformation gradients with respect to the current and rotated configurations as

$$\overset{*}{\mathbf{F}}_\alpha = \frac{\partial \overset{*}{\mathbf{x}}}{\partial \mathbf{X}_\alpha} = \frac{\partial \overset{*}{\mathbf{x}}}{\partial \mathbf{x}} \frac{\partial \mathbf{x}}{\partial \mathbf{X}_\alpha} = \mathbf{Q}\mathbf{F}_\alpha. \tag{3.34}$$

Now, we can show that the volume element $\mathrm{d}v$ is objective using relations (2.18), $(3.31)_1$, and (3.34)

$$\mathrm{d}\overset{*}{v} = \overset{*}{J}_\alpha \,\mathrm{d}V_\alpha = \det(\mathbf{Q}\mathbf{F}_\alpha)\,\mathrm{d}V_\alpha = (\det\mathbf{Q})(\det\mathbf{F}_\alpha)\,\mathrm{d}V_\alpha = J_\alpha\,\mathrm{d}V_\alpha = \mathrm{d}v, \tag{3.35}$$

which also proves the objectivity of volume fractions n^α using its definition (2.3). Now, we introduce the objectivity condition for the solid Helmholtz energy function keeping in mind the objectivity of scalar-valued quantities, i.e., $\overset{*}{\psi}(\overset{*}{\cdot}) = \psi(\cdot)$

$$\overset{*}{\psi}{}^S(\overset{*}{\mathbf{F}}_S, \overset{*}{n}{}^S) = \psi^S(\mathbf{F}_S, n^S), \qquad \longrightarrow \qquad \psi^S(\mathbf{Q}\mathbf{F}_S, n^S) = \psi^S(\mathbf{F}_S, n^S). \tag{3.36}$$

We see that ψ^S cannot be an arbitrary function of $\mathbf{F}_S$. Therefore, we use the transpose of the orthogonal rotation tensor $\mathbf{R}_S^T = \mathbf{Q}$ and the right polar decomposition of $\mathbf{F}_S$ (cf. Section 2.3.4) to obtain

$$\psi^S(\mathbf{F}_S, n^S) = \psi^S(\mathbf{R}_S\mathbf{F}_S, n^S) = \psi^S(\mathbf{R}^T\mathbf{R}\mathbf{U}_S, n^S) = \psi^S(\mathbf{U}_S, n^S). \tag{3.37}$$

which holds for arbitrary $\mathbf{F}_S$. Since the right Cauchy-Green deformation tensor $\mathbf{C}_S$ can be expressed by the right stretch tensor $\mathbf{U}_S$ using the equation (2.27), the Helmholtz energy function can be written as

$$\overset{*}{\psi}{}^S(\mathbf{C}_S, n^S) = \psi^S(\mathbf{C}_S, n^S). \tag{3.38}$$

Therefore, ψ^S depends only on the referential stretch parts of the solid deformation tensor and the scalar objective quantity. Finally, we can show that the rest of the quantities $(\operatorname{grad} n^\alpha, \mathbf{w}_{FS})$ follow the principle of material indifference. Consider the spatial gradient of the objective scalar n^α

$$\overset{*}{\operatorname{grad}}\, n^\alpha = \frac{\partial n^\alpha}{\partial \overset{*}{\mathbf{x}}}\frac{\partial \mathbf{x}}{\partial \mathbf{x}} = \frac{\partial n^\alpha}{\partial \mathbf{x}}\mathbf{Q}^T = \operatorname{grad} n^\alpha \mathbf{Q}^T. \tag{3.39}$$

This proves the objectivity of $\operatorname{grad} n^\alpha$. Also, one should note that we can obtain the relation $\mathbf{Q}'_\alpha = \dot{\mathbf{Q}}$ from the definition of the material time derivative. Also, $\operatorname{grad}\mathbf{Q} = \mathbf{0}$ because the rotation $\mathbf{Q}$ is independent of the constituent it is applied to. We can further make use of the material time derivative to establish the objective nature of the seepage velocity

$$\left.\begin{aligned}(\overset{*}{\mathbf{x}}{}'_S) &= (\mathbf{Q}\mathbf{x})'_S = \dot{\mathbf{Q}}\mathbf{x} + \mathbf{Q}\mathbf{x}'_S,\\ (\overset{*}{\mathbf{x}}{}'_F) &= (\mathbf{Q}\mathbf{x})'_F = \dot{\mathbf{Q}}\mathbf{x} + \mathbf{Q}\mathbf{x}'_F,\end{aligned}\right\} \qquad \longrightarrow \qquad \overset{*}{\mathbf{w}}_{FS} = (\overset{*}{\mathbf{x}}{}'_S) - \overset{*}{\mathbf{x}}{}'_F = \mathbf{Q}\underbrace{(\mathbf{x}'_S - \mathbf{x}'_F)}_{\mathbf{w}_{FS}}. \tag{3.40}$$

Furthermore, the objectivity requirements for a scalar a, vector $\mathbf{a}$, and tensor $\mathbf{A}$ can be summarised as

$$\begin{aligned}\overset{*}{\mathbf{A}}(\overset{*}{\cdot}) &= \mathbf{Q}\mathbf{A}(\cdot)\mathbf{Q}^T,\\ \overset{*}{\mathbf{a}}(\overset{*}{\cdot}) &= \mathbf{Q}\mathbf{a}(\cdot),\\ \overset{*}{a}(\overset{*}{\cdot}) &= a(\cdot).\end{aligned} \tag{3.41}$$

Now, the objectivity of Cauchy stress $\mathbf{T}^S$, First Piola Kirchhoff stress $\mathbf{P}^S$, and Second Piola Kirchhoff $\mathbf{S}^S$ can be shown. The Cauchy traction vector is given by equation (2.56). The transformed Cauchy vector can be written as

$$\overset{*}{\mathbf{t}}{}^S = \overset{*}{\mathbf{T}}{}^S \overset{*}{\mathbf{n}}. \tag{3.42}$$

Using the transformation rule for vectors $(3.41)_2$, we obtain

$$\mathbf{Q}\mathbf{t} = \overset{*}{\mathbf{T}}{}^S \mathbf{Q}\mathbf{n}. \tag{3.43}$$

On comparing equations (3.43) and (2.56), we get the following relation leading to the objectivity of Cauchy stress tensor

$$\overset{*}{\mathbf{T}}{}^S = \mathbf{Q}\mathbf{T}\mathbf{Q}^T. \tag{3.44}$$

Similarly, using the relation (2.60), the transformed first Piola Kirchhoff stress tensor can be written as

$$\overset{*}{\mathbf{P}}{}^S (\overset{*}{\mathbf{F}}_S)^T = \overset{*}{J}_S \overset{*}{\mathbf{T}}{}^S. \tag{3.45}$$

We obtain the objectivity relation for the two-point first Piola Kirchhoff stress tensor by using the objectivity of J_S, (3.34), and (3.44)

$$\begin{aligned} &\overset{*}{\mathbf{P}}{}^S (\mathbf{Q}\mathbf{F}_S)^T = J_S \mathbf{Q}\mathbf{T}^S\mathbf{Q}^T, \\ &\overset{*}{\mathbf{P}}{}^S (\mathbf{F}_S^T\mathbf{Q}^T) = \mathbf{Q}J_S\mathbf{T}^S\mathbf{Q}^T = \mathbf{Q}\mathbf{P}^S(\mathbf{F}_S^T\mathbf{Q}^T), \\ &\overset{*}{\mathbf{P}}{}^S = \mathbf{Q}\mathbf{P}^S. \end{aligned} \tag{3.46}$$

Finally, the Second Piola Kirchhoff $\mathbf{S}$ is parameterised only by the material coordinates. Therefore, it does not depend on any superimposed rigid body motion leading to objectivity

$$\overset{*}{\mathbf{S}} = \mathbf{S}. \tag{3.47}$$

3.2.3 Universal Dissipation

The preceding sections lead to a reduction in the set of process variables allowing for a simplified evaluation of the entropy inequality. In constitutive modelling, the universal dissipation principle must be satisfied by the constitutive relations. Therefore, we evaluate the Clausius Plank inequality by following the procedure of Coleman & Noll [70]. For more information regarding the evaluation of the entropy principle, the reader is referred to Bowen [43] and Ehlers [39].

At first, we evaluate $\rho^\alpha(\psi^\alpha)'_\alpha$ for all the constituents φ^α knowing the Helmholtz free energy dependence following the equations (3.29) and (3.38).

$$\begin{aligned}
\rho^S(\psi^S)'_S &= 2n^S\rho^{SR}\mathbf{F}_S\frac{\partial\psi^S}{\partial\mathbf{C}_S}\mathbf{F}_S^T:\mathbf{d}_S + n^S\rho^{SR}\frac{\partial\psi^S}{\partial n^S}(n^S)'_S,\\
\rho^L(\psi^S)'_L &= n^L\rho^{LR}\frac{\partial\psi^L}{\partial n^L}(n^L)'_L,\\
\rho^N(\psi^S)'_N &= n^N\rho^{NR}\frac{\partial\psi^N}{\partial n^N}(n^N)'_N.
\end{aligned} \tag{3.48}$$

Initially, an additional saturation constraint (2.4) is added to the entropy inequality to ensure the fully saturated condition in the overall aggregate at any given time. This is done by introducing a Lagrangean multiplier p as a weight to the saturation condition as [5]

$$p(n^S+\underbrace{n^L+n^N}_{n^F})'_S = p(\operatorname{grad}n^F\cdot\mathbf{w}_{FS}-(n^S)'_S-(n^L)'_L-(n^N)'_N). \tag{3.49}$$

Moreover, we multiply the volume balance of the individual constituent φ^α with the respective Lagrangean multipliers p^α and make use of the relation $\boldsymbol{l}_\alpha:\mathbf{I}=\mathbf{d}_\alpha:\mathbf{I}=\operatorname{div}\mathbf{x}'_\alpha$ [74]

$$p^\alpha\Big[(n^\alpha)'_\alpha+n^\alpha(\mathbf{d}_\alpha:\mathbf{I})-\frac{\hat\rho^\alpha}{\rho^{\alpha R}}\Big]=0. \tag{3.50}$$

Now using the relations (3.48), (3.49), (3.50), (3.7) and the summation assumption $(2.70)_{1,2}$, we can evaluate the entropy inequality (3.26)

$$\begin{aligned}
&\mathbf{d}_S:\Big\{\mathbf{T}^S-2n^S\rho^{SR}\mathbf{F}_S\frac{\partial\psi^S}{\partial\mathbf{C}_S}\mathbf{F}_S^T+p^Sn^S\mathbf{I}\Big\}+\mathbf{d}_L:\Big\{\mathbf{T}^L+p^Ln^L\mathbf{I}\Big\}\\
&+\mathbf{d}_N:\Big\{\mathbf{T}^N+p^Nn^N\mathbf{I}\Big\}-(n^S)'_S\Big\{p-p^S+n^S\rho^{SR}\frac{\partial\psi^S}{\partial n^S}\Big\}\\
&-(n^L)'_L\Big\{p-p^L+n^L\rho^{LR}\frac{\partial\psi^L}{\partial n^L}\Big\}-(n^N)'_N\Big\{p-p^N+n^N\rho^{NR}\frac{\partial\psi^N}{\partial n^N}\Big\}\\
&-\hat\rho^L\Big\{(\psi^L-\frac{1}{2}\mathbf{x}'_L\cdot\mathbf{x}'_L+\frac{1}{\rho^{LR}}p^L)-(\psi^S-\frac{1}{2}\mathbf{x}'_S\cdot\mathbf{x}'_S+\frac{1}{\rho^{SR}}p^S)\Big\}\\
&-\hat\rho^N\Big\{(\psi^N-\frac{1}{2}\mathbf{x}'_N\cdot\mathbf{x}'_N+\frac{1}{\rho^{NR}}p^N)-(\psi^S-\frac{1}{2}\mathbf{x}'_S\cdot\mathbf{x}'_S+\frac{1}{\rho^{SR}}p^S)\Big\}\\
&-\mathbf{w}_{FS}\cdot\Big\{\hat{\mathbf{p}}^F-p\operatorname{grad}n^F+\hat\rho^S\mathbf{x}'_S\Big\}\geq 0,
\end{aligned} \tag{3.51}$$

which must hold for fixed values of the process variables and arbitrary values of free-available quantities $\mathbf{d}_\alpha,(n^\alpha)'_\alpha$ [74]. Therefore, we obtain the following structure of the

entropy inequality

$$\begin{aligned}&\mathbf{d}_S : \underbrace{\{...\}}_{=\mathbf{0}} + \mathbf{d}_L : \underbrace{\{...\}}_{=\mathbf{0}} + \mathbf{d}_N : \underbrace{\{...\}}_{=\mathbf{0}} - (n^S)'_S \underbrace{\{...\}}_{=0} \\ &- (n^L)'_L \underbrace{\{...\}}_{=0} - (n^N)'_N \underbrace{\{...\}}_{=0} + \underbrace{\mathrm{Dis}}_{\geq 0} \geq 0.\end{aligned} \tag{3.52}$$

In this context, we obtain the necessary and sufficient thermodynamic restrictions. The parts concerning $(n^\alpha)'_\alpha$ give

$$p^\alpha = p + n^\alpha \rho^{\alpha R} \frac{\partial \psi^\alpha}{\partial n^\alpha}. \tag{3.53}$$

Furthermore, we obtain the relations for the partial Cauchy stresses using (3.51) and (3.53)

$$\begin{aligned}\mathbf{T}^S &= -n^S p\mathbf{I} - (n^S)^2 \rho^{SR} \frac{\partial \psi^S}{\partial n^S}\mathbf{I} + \mathbf{T}^S_E, \quad \mathbf{T}^S_E = 2\rho^S \mathbf{F}_S \frac{\partial \psi^S}{\partial \mathbf{C}_S}\mathbf{F}_S^T, \\ \mathbf{T}^L &= -n^L p\mathbf{I} - (n^L)^2 \rho^{LR} \frac{\partial \psi^L}{\partial n^L}\mathbf{I}, \\ \mathbf{T}^N &= -n^N p\mathbf{I} - (n^N)^2 \rho^{NR} \frac{\partial \psi^N}{\partial n^N}\mathbf{I}.\end{aligned} \tag{3.54}$$

We can now introduce the chemical potentials $\overline{\Psi}^\alpha$ using (3.53) and (3.51) as

$$\overline{\Psi}^\alpha = \psi^\alpha - \frac{1}{2}\mathbf{x}'_\alpha \cdot \mathbf{x}_\alpha + n^\alpha \frac{\partial \psi^\alpha}{\partial n^\alpha} + \frac{1}{\rho^{\alpha R}} p. \tag{3.55}$$

For more information on chemical potentials, the reader is referred to Bowen [43]. Furthermore, we make use of the assumption $\hat{\rho}^L = 0$ and (3.1) which gives us the dissipative part as

$$\begin{aligned}\mathrm{Dis} = &- \hat{\rho}^N \underbrace{\left\{ (\psi^N - \frac{1}{2}\mathbf{x}'_N \cdot \mathbf{x}'_N + \frac{1}{\rho^{NR}} p^N) - (\psi^S - \frac{1}{2}\mathbf{x}'_S \cdot \mathbf{x}'_S + \frac{1}{\rho^{SR}} p^S) \right\}}_{\overline{\Psi}^N - \overline{\Psi}^S} \\ &- \mathbf{w}_{FS} \cdot \underbrace{\left\{ \hat{\mathbf{p}}^F - p\,\mathrm{grad}\, n^F + \hat{\rho}^S \mathbf{x}'_S \right\}}_{\hat{\mathbf{p}}^F_E} \geq 0,\end{aligned} \tag{3.56}$$

where the postulations for the chemical potentials have been outlined. Here, $\hat{\mathbf{p}}^F_E$ is called the extra momentum production [75]. Moreover, this gives the restrictions for the solid mass production $\hat{\rho}^S$ and momentum production $\hat{\mathbf{p}}^F$ as postulated by Ricken and Bluhm [74]

$$\begin{aligned}\hat{\rho}^S &= \delta^{NS}(\overline{\Psi}^N - \overline{\Psi}^S), \qquad \text{where} \qquad \delta^{NS} \geq 0, \\ \hat{\mathbf{p}}^F &= p\,\mathrm{grad}\, n^F - \hat{\rho}^S \mathbf{x}'_S - \mathbf{G}_F \mathbf{w}_{FS},\end{aligned} \tag{3.57}$$

where $\mathbf{G}_F = \mathbf{G}_L + \mathbf{G}_N$ is the permeability tensor between the solid and fluid phases. These restrictions give us the possibility to further formulate stresses, mass production and interaction forces.

3.2.4 Stress

The stress relations can be introduced following the restrictions from the entropy inequality (3.54) and neglecting the effective or frictional fluid stress, i.e., $\mathbf{T}_E^F \approx \mathbf{0}$. It is assumed that the fluid extra stress is much smaller in comparison with $\hat{\mathbf{p}}_E^F$ also known as the effective drag force. Therefore, assuming $\partial \psi^F / \partial n^F = 0$ where $\varphi^F = \varphi^L + \varphi^N$ yields [39, 74]

$$\begin{aligned} \mathbf{T}^S &= -n^S p\mathbf{I} - (n^S)^2 \rho^{SR} \frac{\partial \psi^S}{\partial n^S}\mathbf{I} + \mathbf{T}_E^S, \qquad \text{where} \qquad \mathbf{T}_E^S = 2\rho^S \mathbf{F}_S \frac{\partial \psi^S}{\partial \mathbf{C}_S}\mathbf{F}_S^T \\ \mathbf{T}^F &= \mathbf{T}^L + \mathbf{T}^N = -(n^L + n^N)p\mathbf{I} = -n^F p\mathbf{I}, \end{aligned} \tag{3.58}$$

where $\mathbf{T}_E^S$ is the effective or extra solid stress [75, 76]. Furthermore, p is identified as the unspecified pore pressure. The total Cauchy stress is defined as the sum of partial stresses as

$$\mathbf{T} = \mathbf{T}^S + \mathbf{T}^F = \mathbf{T}_E^S - (n^S)^2 \rho^{SR} \frac{\partial \psi^S}{\partial n^S}\mathbf{I} - p\mathbf{I}. \tag{3.59}$$

3.2.5 Filter Velocity

The seepage velocity $\mathbf{w}_{FS} = \mathbf{x}'_F - \mathbf{x}'_S$ determines the motion of the fluid in relation to the solid. For the restriction obtained from the evaluation of entropy inequality $(3.57)_2$, we make use of the permeability tensor proposed by Ricken and Bluhm [74] for anisotropic material and simplify it for the case of isotropic material to obtain

$$\mathbf{G}_F = \alpha_{FS}\mathbf{I}, \tag{3.60}$$

where α_{FS} is the material parameter which can be described either by using initial Darcy's permeability of fluid $k_{OS}^F\,[m/s]$ and effective fluid weight $\gamma^{FR}\,[N/m^3]$ or by using initial intrinsic permeability of solid $K_{OS}^S\,[m^2]$ and dynamic fluid viscosity $\mu^{FR}\,[Ns/m^2]$ [74]

$$\frac{(n^F)^2}{\alpha_{FS}} = \left(\frac{n^F}{n_{OS}^F}\right)^m \frac{k_{OS}^F}{\gamma^{FR}} = \left(\frac{n^F}{n_{OS}^F}\right)^m \frac{K_{OS}^S}{\mu^{FR}}, \tag{3.61}$$

where m is a dimensionless parameter which accounts for the change of permeability [5, 39, 58, 77]. Furthermore, we can introduce the relation for the filter velocity $n^F \mathbf{w}_{FS}$ using the fluid momentum balance $(3.22)_{2+3}$

$$\operatorname{div} \mathbf{T}^F + \rho^F \mathbf{b} + \hat{\mathbf{p}}^F = \mathbf{0}. \tag{3.62}$$

Inserting equation $(3.58)_2$ and (3.60) in (3.62) gives

$$n^F \mathbf{w}_{FS} = \frac{(n^F)^2}{\alpha_{FS}} \left(-\operatorname{grad} p + \rho^{FR}\mathbf{b} - \frac{\hat{\rho}^S}{n^F}\mathbf{x}'_S \right). \tag{3.63}$$

Using the assumption (3.8) and relation (3.61), we obtain Darcy's law for the filter velocity [74, 78]

$$n^F \mathbf{w}_{FS} = -\left(\frac{n^F}{n^F_{OS}}\right)^m \frac{K^S_{OS}}{\mu^{FR}} \left(\operatorname{grad} p - \rho^{FR}\mathbf{b} + \frac{\hat{\rho}^S}{n^F}\mathbf{x}'_S \right), \tag{3.64}$$

where $(n^F/n^F_{0S})^m K^S_{0S} = K^S_E$ is referred to as effective permeability and accounts for the permeability due to change in volume fractions. The filter law can also be written in terms of the specific permeability $K^F\,[m^4/Ns]$. These can be related to each other using the following relations

$$\begin{aligned} \text{Darcy} : k^F &:= \gamma^{FR} K^F = \frac{\gamma^{FR}}{\mu^{FR}} K^S \\ \text{Specific} : K^F &:= \frac{k^F}{\gamma^{FR}} = \frac{K^S}{\mu^{FR}} \\ \text{Intrinsic} : K^S &= \mu^{FR} K^F = \frac{\mu^{FR}}{\gamma^{FR}} k^F \end{aligned} \tag{3.65}$$

3.2.6 Mass Production

According to the assumption (3.8), the mass exchange occurs between the solid and nutrient phases $\hat{\rho}^S = -\hat{\rho}^N$. Following the evaluation of the entropy inequality and making use of the postulations proposed by Ricken et al. [57, 58, 74], the solid mass supply is defined by $(3.57)_1$. For the solid growth process, the chemical potential functions are related as

$$\hat{\rho}^S \geq 0 \quad \longrightarrow \quad \overline{\Psi}^N \geq \overline{\Psi}^S. \tag{3.66}$$

In view of the solid growth, we formulate the mass supply term of the solid phase following the description of thrombus formation and growth process. Therefore, we postulate the solid mass production $\hat{\rho}^S[kg/m^3 s]$ as a function of $\mathbf{w}_{FS}$ and n^N as

$$\begin{aligned} \hat{\rho}^S &= \hat{\rho}^S(\mathbf{w}_{FS}, n^N) = \mathcal{C}\, \hat{\rho}^S_{\mathbf{w}_{FS}}(\mathbf{w}_{FS})\, \hat{\rho}^S_{n^N}(n^N), \\ \hat{\rho}^S_{\mathbf{w}_{FS}}(\mathbf{w}_{FS}) &= exp\big\{-\|\mathbf{w}_{FS}\|^2/\beta_1\big\}, \\ \hat{\rho}^S_{n^N}(n^N) &= -exp\big\{-(n^N)^2\beta_2\big\} + 1, \end{aligned} \tag{3.67}$$

where $\mathcal{C}$ represents the maximum mass exchange, and β_1 and β_2 are the material parameters added in the respective formats for convenient formulation. β_1 and β_2 reflect the

dependence of mass exchange rate on the seepage velocity and nutrient volume fraction, cf. Figure 3.2.

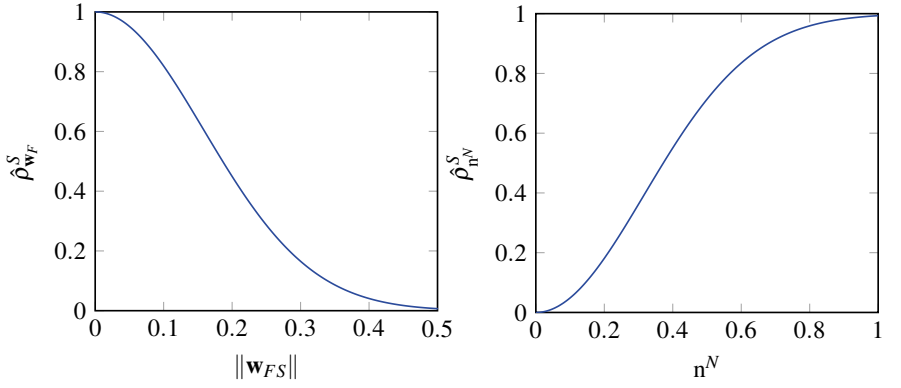

Figure 3.2: Mass exchange rate dependence on the seepage velocity $\mathbf{w}_{FS}$ and nutrient volume fraction n^N with $\beta_1 = 0.05$ and $\beta_2 = 5.0$.

Even though the effects of the blood velocity and the nutrients on thrombus growth are well-researched [64–66], the data for the parameters are difficult to obtain for this approach. Therefore, we choose the parameters that give reasonable results.

3.2.7 Isotropic Elasticity

In the presented monograph, we consider the thrombus to be an isotropic material, cf. 3.1.1. An isotropic material does not have a preferred direction. Therefore, the material response must be invariant with respect to all the rotations superimposed on the reference configuration following the principle of material symmetry. Since we know from (3.29) and Section 3.2.4 that only ψ^S remains, we formulate the following relations from the solid constituent point of view.

The rotation tensor $\mathbf{Q}$ rotates the neighbourhood of the material point $\mathbf{X}_S$ because it is a local concept, cf. Figure 3.3. This gives

$$\overline{\mathbf{X}}_S = \mathbf{c} + \mathbf{Q}\mathbf{X}_S. \tag{3.68}$$

$\bar{(\cdot)}$, in this section, denotes the quantities after rotation of the reference configuration. Here $\mathbf{Q}$ belongs to the symmetry group G_{sym}, which is the complete set of $\mathcal{SO}_3$ for an isotropic material. Now we can introduce the motion function $\overline{\chi}_S$ which maps $\overline{\mathbf{X}}_S$ to $\mathbf{x}$

$$\mathbf{x} = \chi_S(\mathbf{X}_S, t) = \overline{\chi}_S(\overline{\mathbf{X}}_S, t). \tag{3.69}$$

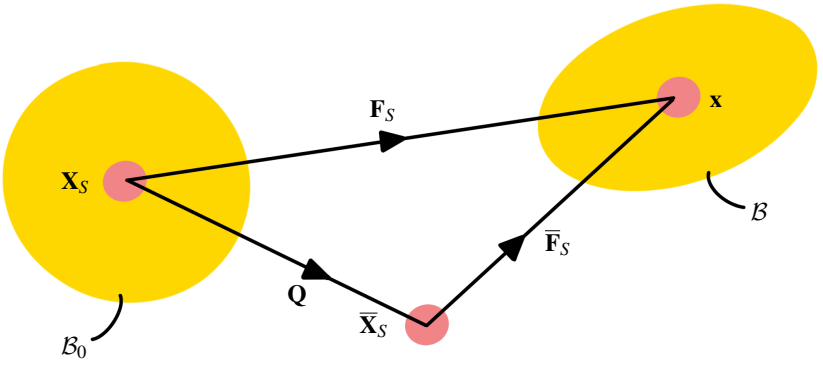

Figure 3.3: Principle of material symmetry

Using the chain rule, (3.68), and (3.69), we obtain

$$\mathbf{F}_S = \frac{\partial \mathbf{x}}{\partial \mathbf{X}_S} = \frac{\partial \mathbf{x}}{\partial \overline{\mathbf{X}}_S}\frac{\partial \overline{\mathbf{X}}_S}{\partial \mathbf{X}_S} = \overline{\mathbf{F}}_S\mathbf{Q} \quad \longrightarrow \quad \overline{\mathbf{F}}_S = \mathbf{F}\mathbf{Q}^T. \tag{3.70}$$

The position vector $\overline{\mathbf{X}}_S$ can be transformed to the current configuration using $\overline{\mathbf{F}}_S$. This means that we can arbitrarily pre-rotate the material. This gives the condition for $\mathbf{C}_S$

$$\overline{\mathbf{C}}_S = (\overline{\mathbf{F}}_S)^T\overline{\mathbf{F}}_S = \mathbf{Q}\mathbf{F}_S^T\mathbf{F}_\alpha\mathbf{Q}^T = \mathbf{Q}\mathbf{C}_S\mathbf{Q}^T. \tag{3.71}$$

In this context, the invariance requirement for the Helmholtz free energy is

$$\psi^S(\mathbf{C}_S, n^S) = \psi^S(\overline{\mathbf{C}}_S, \overline{n}^S). \tag{3.72}$$

From the definition of n^S (2.3), one can see that $\overline{n}^S = n^S$. This leaves us with

$$\psi^S(\mathbf{C}_S, n^S) = \psi^S(\overline{\mathbf{C}}_S, n^S). \tag{3.73}$$

The relation between ψ^α and $\mathbf{C}^\alpha$ must be independent of the chosen material axes. Therefore, we represent $\mathbf{C}_\alpha$ in terms of its invariants. This can be achieved by inserting the spectral decomposition of $\mathbf{C}_\alpha$ $(2.37)_1$ in (3.73) which yields

$$\begin{aligned}\psi^S(\sum_{i=1}^{3}(\lambda_S^i)^2\hat{\mathbf{N}}_S^i\otimes\hat{\mathbf{N}}_S^i, n^S) &= \psi^S(\mathbf{Q}(\sum_{i=1}^{3}(\lambda_S^i)^2\hat{\mathbf{N}}_S^i\otimes\hat{\mathbf{N}}_S^i)\mathbf{Q}^T, n^S)\\ &= \psi^S(\sum_{i=1}^{3}(\lambda_S^i)^2(\mathbf{Q}\hat{\mathbf{N}}_S^i)\otimes(\mathbf{Q}\hat{\mathbf{N}}_S^i), n^S).\end{aligned} \tag{3.74}$$

Consequently, the Helmholtz free energy function depends only on principle stretches λ_S^i and not on the eigenvectors because $\|\mathbf{N}_S^i\| = 1$ and $\|\mathbf{Q}\mathbf{N}_S^i\| = 1$, which yields the following representation for isotropy

$$\psi^S(\mathbf{C}_S, n^S) = \psi^S(\lambda_S^1, \lambda_S^2, \lambda_S^3, n^S). \tag{3.75}$$

Furthermore, following the characteristic polynomial (2.40) of the eigenvalue problem and the definition of the invariants (2.41) and (2.42), the Helmholtz free energy function can be written as a function of principal invariants and solid volume fraction

$$\psi^S = \psi^S(n^S, I_{\mathbf{C}_S}, II_{\mathbf{C}_S}, III_{\mathbf{C}_S}). \tag{3.76}$$

The structure of the equation satisfies the invariance and polyconvexity condition, which also implies quasiconvexity. That would ensure the existence of minimizers of the related variational principles in finite elasticity. For a detailed discussion on convexity conditions, the reader is referred to Dacorogna [79].

3.2.8 Material Law

The purpose of this section is to present the material law for the porous solid matrix. Following the dependency of the Helmholtz free energy function from equation (3.76), a modified neo-Hookean law is introduced as [80]

$$\psi^S = \left(\frac{n^S}{n_{OS}^S}\right)^n \frac{1}{\rho_{OS}^S}\Big\{\frac{\mu^S}{2}(I_{\mathbf{C}_S} - 3) - \mu^S ln J_S + \lambda^S \frac{1}{2}(ln J_S)^2\Big\}, \tag{3.77}$$

where the term in the front with solid volume fraction n^S accounts for the change in solid rigidity with respect to the initial volume fraction n_{OS}^S. The rest of the part is the standard Neo-Hookean material law. μ^S and λ^S are the macroscopic Lam*é* constants and $III_S = J_S^2$ $(2.41)_3$. From (3.77) and (3.58), the effective solid Cauchy stress can be obtained

$$\mathbf{T}_E^S = \left(\frac{n^S}{n_{OS}^S}\right)^{(n+1)} \Big\{\mu^S(\mathbf{b}_S - \mathbf{I}) + \lambda^S(ln J_S)\mathbf{I}\Big\}. \tag{3.78}$$

With equations (3.77), (3.58) and (3.78), total solid Cauchy stress can be written as

$$\begin{aligned}\mathbf{T}^S = &-n^S p\mathbf{I} - n\left(\frac{n^S}{n_{OS}^S}\right)^{n+1} \Big\{\frac{\mu^S}{2}(I_{\mathbf{C}_S} - 3) - \mu^S ln J_S + \frac{\lambda^S}{2}(ln J_S)^2\Big\}\mathbf{I} \\ &+ \left(\frac{n^S}{n_{OS}^S}\right)^{n+1} \Big\{\mu^S(\mathbf{b}_S - \mathbf{I}) + \lambda^S(ln J_S)\mathbf{I}\Big\}.\end{aligned} \tag{3.79}$$

The effective solid Kirchhoff stress and total solid Kirchhoff stress then reads as

$$\begin{aligned}
\tau_E^S &= J_S \mathbf{T}_E^S = J_S \left(\frac{n^S}{n_{OS}^S} \right)^{(n+1)} \left\{ \mu^S (\mathbf{b}_S - \mathbf{I}) + \lambda^S (ln J_S) \mathbf{I} \right\}, \\
\tau^S &= -J_S n^S p \mathbf{I} - J_S n \left(\frac{n^S}{n_{OS}^S} \right)^{n+1} \left\{ \frac{\mu^S}{2} (I_{\mathbf{C}_S} - 3) - \mu^S ln J_S + \lambda^S \frac{1}{2} (ln J_S)^2 \right\} \mathbf{I} \\
&\quad + J_S \left(\frac{n^S}{n_{OS}^S} \right)^{(n+1)} \left\{ \mu^S (\mathbf{b}_S - \mathbf{I}) + \lambda^S (ln J_S) \mathbf{I} \right\}.
\end{aligned} \tag{3.80}$$

4 NUMERICAL TREATMENT

The purpose of this section is to briefly introduce the numerical tools needed to treat the initial boundary value problem. At first, we obtain the weak formulation of the governing partial differential equations (PDE). Then, the equations are discretised in space using finite elements and in time using the finite difference method. Afterwards, we present a solution scheme for the unknown quantities of the discretised system.

4.1 Weak Formulation

As a first step, we need to formulate the local strong form of the governing equations into an integral weak form. This is done by the method of weighted residuals. Let us assume a boundary value problem with a differential equation

$$F(u) = 0, \tag{4.1}$$

and given boundary conditions. We can choose a linear trial function $\tilde{u}$ given by

$$\tilde{u} = \sum_{i=1}^{N} \phi_i \tilde{u}_i, \tag{4.2}$$

where ϕ_i are the set of shape functions and $\tilde{u}_i$ are free parameters. In general, the trial function will not fulfil the differential equation exactly and will lead to an error or a residual R,

$$F(\tilde{u}) = R(\tilde{u}_i) \neq 0. \tag{4.3}$$

We need to find the parameters $\tilde{u}_i$ that will minimize the residual. However, equation (4.3) gives us only one equation to determine N unknown $\tilde{u}_i$. To have more equations, we introduce a set of N distinct weight functions w_j, $j = 1, ..., N$, which needs to satisfy

$$\int_{\Omega} w_j R \, \mathrm{d}v = 0. \tag{4.4}$$

Following this, we require the integral of the residual weighted with test functions (weight functions) to vanish over the domain Ω instead of the residual vanishing everywhere. Since this is a much weaker requirement than the exact satisfaction of the differential equation, equation (4.4) is known as a weak form of the differential equation (4.1). Thereafter, we introduce the weak forms of the momentum balance of mixture, volume balance of mixture, volume balance of solid and volume balance of nutrients by multiplying them with respective test functions.

Considering the assumptions, balance equations and constitutive relations from the preceding Chapter, we have a set of six independent variables

$$\mathcal{U} = \mathcal{U}(\mathbf{x},t) = \left\{\mathbf{u}_S, \mathbf{w}_{FS}, n^S, n^N, n^L, p\right\} \tag{4.5}$$

Using Darcy's formulation for seepage velocity $\mathbf{w}_{FS}$ (3.64), the set of unknowns could be decreased to five. Furthermore, the saturation condition (3.14) ($n^L = 1 - n^S - n^N$) reduces the set of unknowns to four

$$\mathcal{U} = \mathcal{U}(\mathbf{x},t) = \left\{\mathbf{u}_S, p, n^N, n^S\right\}. \tag{4.6}$$

The strong forms of the governing equations are

• Momentum balance of mixture :

$$\operatorname{div}(\mathbf{T}^S + \mathbf{T}^L + \mathbf{T}^N) + (\rho^S + \rho^L + \rho^N)\mathbf{b} + \hat{\rho}^S \mathbf{w}_{FS} = \mathbf{0}. \tag{4.7}$$

• Volume balance of mixture :

$$\operatorname{div}(\mathbf{x}'_S + n^F \mathbf{w}_{FS}) + \hat{\rho}^S \left(\frac{1}{\rho^{NR}} - \frac{1}{\rho^{SR}}\right) = 0. \tag{4.8}$$

• Volume balance of nutrients :

$$(n^N)'_S + \operatorname{div}(n^N \mathbf{w}_{FS}) + n^N \operatorname{div} \mathbf{x}'_S = \hat{n}^N. \tag{4.9}$$

• Volume balance of solid :

$$(n^S)'_S + n^S \operatorname{div} \mathbf{x}'_S = \hat{n}^S. \tag{4.10}$$

We use the solid volume fraction n^S as an additional degree of freedom to calculate the growth process globally, with the solid volume balance as the governing equation. Here, $\mathbf{w}_{FS}$ and $\hat{\rho}^S$ can be substituted by the equations (3.64) and (3.67), respectively. To obtain the weak forms of the balance equations, we multiply the momentum balance of mixture (4.7), volume balance of mixture (4.8), volume balance of nutrients (4.9), and volume balance of solid (4.10) with the test functions $\delta\mathbf{u}_S$, δp, δn^N, and δn^S, respectively. Then we integrate the equations over the spatial domain Ω, occupied by the body B at time t. We use the integration by parts and the divergence theorem for equations (4.7) - (4.9) to introduce the Neumann (natural) boundary terms. This yields the weak formulation of the governing equations

• Momentum balance of mixture:

$$\begin{aligned} \mathcal{G}_{\mathbf{u}_S} = &\int_\Omega (\mathbf{T}) \,:\, \operatorname{grad} \delta\mathbf{u}_S \,\mathrm{d}v - \int_\Omega (\rho^S + \rho^F)\,\mathbf{b} \cdot \delta\mathbf{u}_S \,\mathrm{d}v \\ &- \int_\Omega \hat{\rho}^S \mathbf{w}_{FS} \cdot \delta\mathbf{u}_S \,\mathrm{d}v - \int_{\Gamma_\mathbf{t}} \mathbf{t} \cdot \delta\mathbf{u}_S \,\mathrm{d}a = 0. \end{aligned} \tag{4.11}$$

• Volume balance of mixture:

$$\begin{aligned}\mathcal{G}_p = &\int_\Omega \operatorname{div}\mathbf{x}'_S\,\delta p\,\mathrm{d}v - \int_\Omega n^F\mathbf{w}_{FS}\cdot\operatorname{grad}\delta p\,\mathrm{d}v \\ &+ \int_\Omega \hat{\rho}^S\left(\frac{1}{\rho^{NR}} - \frac{1}{\rho^{SR}}\right)\delta p\,\mathrm{d}v + \int_{\Gamma_q} \underbrace{n^F\mathbf{w}_{FS}\cdot\mathbf{n}}_{:=q}\,\delta p\,\mathrm{d}a = 0.\end{aligned} \tag{4.12}$$

• Volume balance of nutrients:

$$\begin{aligned}\mathcal{G}_{n^N} = &\int_\Omega \left((n^N)'_S + n^N\operatorname{div}\mathbf{x}'_S - \frac{\hat{\rho}^N}{\rho^{NR}}\right)\delta n^N\,\mathrm{d}v + \underbrace{\int_\Omega \operatorname{grad}n^N\cdot\operatorname{grad}\delta n^N\,\mathrm{d}v}_{:=r} \\ &- \int_\Omega n^N\mathbf{w}_{FS}\cdot\operatorname{grad}\delta n^N\,\mathrm{d}v + \int_{\Gamma_\upsilon} \underbrace{n^N\mathbf{w}_{FS}\cdot\mathbf{n}}_{:=\upsilon}\,\delta n^N\,\mathrm{d}a = 0.\end{aligned} \tag{4.13}$$

• Volume balance of solid:

$$\mathcal{G}_{n^S} = \int_\Omega (n^S)'_S\,\delta n^S\,\mathrm{d}v + \int_\Omega n^S\operatorname{div}\mathbf{x}'_S\,\delta n^S\,\mathrm{d}v - \int_\Omega \frac{\hat{\rho}^S}{\rho^{SR}}\,\delta n^S\,\mathrm{d}v = 0. \tag{4.14}$$

Here, the mass transport equation (4.9) consists of the general structure of an advection equation with the source term on the right-hand side. It is known that using the given approach for formulating weak forms, the equation (4.13) generates large oscillations if not properly stabilised or if the mesh size is not excessively small. Therefore, an artificial diffusion term (r) is added only to the volume balance of nutrients (4.13) to stabilise the transport equation. For more information on the mass transport equation and the stabilisation schemes, the reader is referred to Santos et al. [81] and the references therein. Furthermore, we can see from the above equations that some of the volume integrals have been transformed into surface integrals to give the Neumann boundary conditions. Therefore, the overall surface $\Gamma = \partial\Omega$ of the spatial domain Ω is decomposed in the following way

$$\begin{aligned}\Gamma = \Gamma_{\mathbf{u}_S} \cup \Gamma_{\mathbf{t}} \qquad &\text{with} \qquad \Gamma_{\mathbf{u}_S} \cap \Gamma_{\mathbf{t}} = \phi, \\ \Gamma = \Gamma_p \cup \Gamma_q \qquad &\text{with} \qquad \Gamma_p \cap \Gamma_q = \phi, \\ \Gamma = \Gamma_{n^N} \cup \Gamma_\upsilon \qquad &\text{with} \qquad \Gamma_{n^N} \cap \Gamma_\upsilon = \phi.\end{aligned} \tag{4.15}$$

Here, $\Gamma_{\mathbf{u}_S}$, Γ_p, and Γ_{n^N} are identified as the Dirichlet boundaries. $\Gamma_{\mathbf{t}}$, Γ_q, and Γ_υ are the Neumann boundaries. There is only Dirichlet boundary Γ_{n^S} for the volume balance of solid as there is no Neumann boundary condition. $\mathbf{t}$ is the external load vector acting on the Neumann boundary $\Gamma_{\mathbf{t}}$, $q = n^F\mathbf{w}_{FS}\cdot\mathbf{n}$ is the fluid volume efflux on the Neumann boundary Γ_q and $\upsilon = n^N\mathbf{w}_{FS}\cdot\mathbf{n}$ is the nutrient volume efflux on the Neumann boundary Γ_υ, where $\mathbf{n}$ is the outward-oriented unit surface normal. Here, one should notice that an application of Dirichlet and Neumann conditions simultaneously at a surface is not allowed (4.15). Also, the order of PDE (4.7) is reduced by one order in the weak form (4.11).

Furthermore, we need an appropriate ansatz for the trial functions of the primary variables $\{\mathbf{u}_S, p, n^N, n^S\}$ and the test functions $\{\delta\mathbf{u}_S, \delta p, \delta n^N, \delta n^S\}$. The respective functions are taken from the Sobolev space $\mathcal{H}^1(\Omega)$ which yields

$$\begin{aligned}
\mathcal{S}_{\mathbf{u}_S}(t) &= \{\mathbf{u}_S \in \mathcal{H}^1(\Omega)^D \quad : \quad \mathbf{u}_S(\mathbf{x}) = \bar{\mathbf{u}}_S(\mathbf{x},t) \quad \text{on} \quad \Gamma_{\mathbf{u}_S}\}, \\
\mathcal{S}_p(t) &= \{p \in \mathcal{H}^1(\Omega) \quad : \quad p(\mathbf{x}) = \bar{p}(\mathbf{x},t) \quad \text{on} \quad \Gamma_p\}, \\
\mathcal{S}_{n^N}(t) &= \{n^N \in \mathcal{H}^1(\Omega) \quad : \quad n^N(\mathbf{x}) = \bar{n}^N(\mathbf{x},t) \quad \text{on} \quad \Gamma_{n^N}\}, \\
\mathcal{S}_{n^S}(t) &= \{n^S \in \mathcal{H}^1(\Omega) \quad : \quad n^S(\mathbf{x}) = \bar{n}^S(\mathbf{x},t) \quad \text{on} \quad \Gamma_{n^S}\}, \\
\mathcal{T}_{\mathbf{u}_S} &= \{\delta\mathbf{u}_S \in \mathcal{H}^1(\Omega)^D \quad : \quad \delta\mathbf{u}_S(\mathbf{x}) = \mathbf{0} \quad \text{on} \quad \Gamma_{\mathbf{u}_S}\}, \\
\mathcal{T}_p &= \{\delta p \in \mathcal{H}^1(\Omega) \quad : \quad \delta p(\mathbf{x}) = 0 \quad \text{on} \quad \Gamma_p\}, \\
\mathcal{T}_{n^N} &= \{\delta n^N \in \mathcal{H}^1(\Omega) \quad : \quad \delta n^N(\mathbf{x}) = 0 \quad \text{on} \quad \Gamma_{n^N}\}, \\
\mathcal{T}_{n^S} &= \{\delta n^S \in \mathcal{H}^1(\Omega) \quad : \quad \delta n^S(\mathbf{x}) = 0 \quad \text{on} \quad \Gamma_{n^S}\},
\end{aligned} \tag{4.16}$$

where $D \in \{1,2\}$ (dimension in space) because we work on 2-d problems in this monograph. $\bar{\mathbf{u}}_S, \bar{p}, \bar{n}^N$, and $\bar{n}^S$ are the Dirichlet (essential) boundary conditions which are exactly fulfilled by the proper choice of the trial functions $\mathbf{u}_S \in \mathcal{S}_{\mathbf{u}_S}(t), p \in \mathcal{S}_p(t), n^N \in \mathcal{S}_{n^N}(t)$, and $n^S \in \mathcal{S}_{n^S}(t)$. Also, the test functions $\delta\mathbf{u}_S \in \mathcal{T}_{\mathbf{u}_S}, \delta p \in \mathcal{T}_p, \delta n^N \in \mathcal{T}_{n^N}$ and $\delta n^S \in \mathcal{T}_{n^S}$ vanish at the Dirichlet boundaries. For a clear and compact representation, the variational problem is summarised using the functional $\boldsymbol{\mathcal{G}}_{\mathbf{u}}$ containing weak formulations (4.11) - (4.14) and the vector of unknowns $\mathbf{u}$ containing the unknown field variables

$$\boldsymbol{\mathcal{G}}_{\mathbf{u}} = \begin{bmatrix} \mathcal{G}_{\mathbf{u}_S} \\ \mathcal{G}_p \\ \mathcal{G}_{n^N} \\ \mathcal{G}_{n^S} \end{bmatrix}, \quad \mathbf{u} = \begin{bmatrix} \mathbf{u}_S \\ p \\ n^N \\ n^S \end{bmatrix}, \quad \delta\mathbf{u} = \begin{bmatrix} \delta\mathbf{u}_S \\ \delta p \\ \delta n^N \\ \delta n^S \end{bmatrix}, \quad \mathbf{u}'_S = \begin{bmatrix} (\mathbf{u}_S)'_S \\ (p)'_S \\ (n^N)'_S \\ (n^S)'_S \end{bmatrix}, \quad \mathbf{u}_0 = \begin{bmatrix} \mathbf{u}_{S0} \\ p_0 \\ n^N_0 \\ n^S_0 \end{bmatrix}. \tag{4.17}$$

Here, vector $\delta\mathbf{u}$ consists of the test functions, vector $\mathbf{u}'_S$ represents the time derivative of the unknowns for which a suitable time integration scheme will be used, and vector $\mathbf{u}_0 = \mathbf{u}(\mathbf{x}, t_0)$ contains the initial value of the unknowns. Following this, we can write a generalised form of the variational problem (4.11) - (4.14) as

$$\text{Find} \quad \mathbf{u} \in \mathcal{S}_{\mathbf{u}}(t) \quad \text{such that} \quad \boldsymbol{\mathcal{G}}_{\mathbf{u}}(\mathbf{u}, \delta\mathbf{u}) = \mathbf{0} \quad \forall \quad \delta\mathbf{u} \in \mathcal{T}_{\mathbf{u}}, t \in \left[t_0, T\right], \tag{4.18}$$

where $\mathcal{S}_{\mathbf{u}}(t)$ is the combination of the trial spaces $\mathcal{S}_{\mathbf{u}_S}, \mathcal{S}_p, \mathcal{S}_{n^N}$, and $\mathcal{S}_{n^S}$. $\mathcal{T}_{\mathbf{u}}$ is the combination of the test spaces $\mathcal{T}_{\mathbf{u}_S}, \mathcal{T}_p, \mathcal{T}_{n^N}$, and $\mathcal{T}_{n^S}$. $\left[t_0, T\right]$ is the considered time interval. As a next step, we define the function spaces $\mathcal{S}_{\mathbf{u}}$ and $\mathcal{T}_{\mathbf{u}}$.

4.2 Bubnov-Galerkin Method and Mixed Finite Elements

For spatial discretisation, we need to partition the spatial domain Ω into smaller and non-overlapping subdomains Ω_e, which on summation, yields an approximate domain Ω^h

$$\Omega \approx \Omega^h = \bigcup_{e=1}^{N_e} \Omega_e. \tag{4.19}$$

The subdomains Ω_e are known as finite elements (FE). These N_e elements constitute the FE mesh Ω^h. Each element consists of N_n nodes leading to N_N nodes in the FE mesh, which approximates the discretised spatial domain Ω^h. Moreover, this allows replacing the continuous trial and test spaces $\mathcal{S}_\mathbf{u}$ and $\mathcal{T}_\mathbf{u}$ by the discrete N_N-dimentional spaces $\mathcal{S}^h_\mathbf{u}$ and $\mathcal{T}^h_\mathbf{u}$, respectively. We can define the discrete trial and test functions as

$$\begin{aligned}
\mathbf{u}_S(\mathbf{x},t) \approx \mathbf{u}^h_S(\mathbf{x},t) &= \sum_{j=1}^{N_{\mathbf{u}_S}} N^j_{\mathbf{u}_S}(\mathbf{x})\mathbf{u}^j_S(t) \quad \in \quad \mathcal{S}^h_{\mathbf{u}_S}(t),\\
p(\mathbf{x},t) \approx p^h(\mathbf{x},t) &= \sum_{j=1}^{N_p} N^j_p(\mathbf{x})p^j(t) \quad \in \quad \mathcal{S}^h_p(t),\\
n^N(\mathbf{x},t) \approx n^{Nh}(\mathbf{x},t) &= \sum_{j=1}^{N_{n^N}} N^j_{n^N}(\mathbf{x})n^{Nj}(t) \quad \in \quad \mathcal{S}^h_{n^N}(t),\\
n^S(\mathbf{x},t) \approx n^{Sh}(\mathbf{x},t) &= \sum_{j=1}^{N_{n^S}} N^j_{n^S}(\mathbf{x})n^{Sj}(t) \quad \in \quad \mathcal{S}^h_{n^S}(t),\\
\delta\mathbf{u}_S(\mathbf{x}) \approx \delta\mathbf{u}^h_S(\mathbf{x}) &= \sum_{j=1}^{N_{\mathbf{u}_S}} M^j_{\mathbf{u}_S}(\mathbf{x})\delta\mathbf{u}^j_S \quad \in \quad \mathcal{T}^h_{\mathbf{u}_S},\\
\delta p(\mathbf{x}) \approx \delta p^h(\mathbf{x}) &= \sum_{j=1}^{N_p} M^j_p(\mathbf{x})\delta p^j \quad \in \quad \mathcal{T}^h_p,\\
\delta n^N(\mathbf{x}) \approx \delta n^{Nh}(\mathbf{x}) &= \sum_{j=1}^{N_{n^N}} M^j_{n^N}(\mathbf{x})\delta n^{Nj} \quad \in \quad \mathcal{T}^h_{n^N},\\
\delta n^S(\mathbf{x}) \approx \delta n^{Sh}(\mathbf{x}) &= \sum_{j=1}^{N_{n^S}} M^j_{n^S}(\mathbf{x})\delta n^{Sj} \quad \in \quad \mathcal{T}^h_{n^S}.
\end{aligned} \tag{4.20}$$

Here, $\{N_{\mathbf{u}_S}, N_p, N_{n^N}, N_{n^S}\}$ denotes the number of nodes used for approximation of the fields. $\{N_\alpha\} \leq N_N$ may differ depending on the chosen accuracy of the approximation. $\{N^j_{\mathbf{u}_S}, N^j_p, N^j_{n^N}, N^j_{n^S}\}$ represent the global basis functions for the trial functions. $\{\mathbf{u}^j_S, p^j, n^{Nj}, n^{Sj}\}$ denote the time-dependent values of nodal degrees of freedom

(DOF). $\{M^j_{\mathbf{u}_S}, M^j_p, M^j_{n^N}, M^j_{n^S}\}$ denotes the global basis functions for the test functions and $\{\delta\mathbf{u}_S{}^j, \delta p^j, \delta n^{Nj}, \delta n^{Sj}\}$ are the nodal values of the test functions. We apply the standard Bubnov-Galerkin procedure where the basis functions of the trial and test functions are the same $N^j_{(\cdot)} \equiv M^j_{(\cdot)} = \phi^j_{(\cdot)}$. The test functions $\delta(\cdot)$ naturally vanish at the homogeneous Dirichlet boundaries where discrete values are prescribed. Here, one should note that the basis functions $\{\phi^j_{\mathbf{u}_S}, \phi^j_p, \phi^j_{n^N}, \phi^j_{n^S}\}$ depend on the position $\mathbf{x}$ whereas the unknown nodal quantities $\{\mathbf{u}^j_S, p^j, n^{Nj}, n^{Sj}\}$ are a function of time. Using the discrete trial and test functions (4.20), the discretised variational problem (4.18) can be summarised as

$$\text{Find} \quad \mathbf{u}^h \in \mathcal{S}^h_{\mathbf{u}}(t) \quad \text{such that} \quad \mathcal{G}^h_{\mathbf{u}}(\mathbf{u}^h, \delta\mathbf{u}^h) = \mathbf{0} \quad \forall \quad \delta\mathbf{u}^h \in \mathcal{T}^h_{\mathbf{u}}, t \in \left[t_0, T\right]. \tag{4.21}$$

The discretised variational problem (4.21) gives a system of $D \cdot N_{\mathbf{u}_S} + N_p + N_{n^N} + N_{n^S}$ linearly independent equations which is obtained by setting one test function at a given node to unity and rest of them to zero, e.g., $\delta p^1 = 1$, while $\delta p^j = 0$ for $j = 2, ..., N_p$, $\delta\mathbf{u}^j_{SD} = 0$ for $j = 1, ..., N_{\mathbf{u}_S}$, δn^{Nj} for $j = 1, ..., N_{n^N}$, and $\delta n^{Sj} = 0$ for $j = 1, ..., N_{n^S}$.

During the spatial discretisation of the triphasic model within the FEM framework, we need to use mixed formulation because the unknowns have to be approximated simultaneously. Special care must be taken during the choice of shape functions as the governing equations are highly coupled, and the shape functions must satisfy the so-called inf-sup condition, often known as Ladyzhenskaya-Babuška-Brezzi (LLB) condition, for a stable formulation. The reader is referred to Wieners [82], Langtangen & Tveito [83], Brezzi & Fortin [84], and Braess [85].

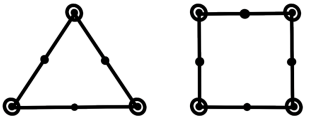

- solid displacement $\mathbf{u}_S$
- solid displacement $\mathbf{u}_S$, pressure p, nutrient volume fraction n^N, and solid volume fraction n^S

Figure 4.1: Two-dimensional Taylor-Hood elements.

In the presented monograph, we choose quadratic shape functions for the solid displacement $\mathbf{u}_S$ and linear shape functions for the pressure p, nutrient volume fraction n^N, and solid volume fraction n^S. This combination of the shape functions leads to the choice of mixed finite elements, also known as the Taylor-Hood elements, as suggested by Taylor & Hood [86]. The examples of two-dimensional Taylor-Hood elements are shown in Figure 4.1.

4.3 Geometry Transformation and Numerical Integration

Moreover, the trial and test functions are expressed in terms of the reference element leading to the introduction of the geometry transformation and local coordinates ξ. Considering a reference element E_r, the relation between the local coordinates ξ and the global coordinates $\mathbf{x}$ is given as

$$\mathbf{x}(\xi) = \sum_{i=1}^{N_n} \phi^i_{\text{geo}}(\xi)\mathbf{x}_i, \tag{4.22}$$

where $\mathbf{x}(\xi)$ is the position depending on the local coordinates ξ and ϕ^i_{geo} are the basis functions of the geometry transformation. Furthermore, we use the same quadratic basis functions for the geometry transformation as for the solid displacements $\mathbf{u}_S$. Therefore, we use isoparametric mapping with respect to the solid displacement and superparametric (ansatz for geometry transformation higher than primary variables) mapping with respect to the other primary variables. For evaluation within a reference element E_r, we reformulate the integrals with respect to the local coordinates ξ, which yields

$$\int_{\Omega_e} f(\mathbf{x})\,\mathrm{d}v = \int_{E_r} f(\mathbf{x}(\xi))J_r(\xi)\,\mathrm{d}v_r, \tag{4.23}$$

where $\mathrm{d}v_r$ is the volume element of the reference element E_r. J_r is the Jacobin determinant of the reference element given by

$$J_r(\xi) = \det\left(\frac{\mathrm{d}\mathbf{x}(\xi)}{\mathrm{d}\xi}\right). \tag{4.24}$$

We obtain the following relation for the quantities involving derivatives with respect to the global coordinates like a gradient or divergence

$$\frac{\mathrm{d}f(\mathbf{x})}{\mathrm{d}\mathbf{x}} = J_r^{-1}\frac{\mathrm{d}f(\mathbf{x}(\xi))}{\mathrm{d}\xi}. \tag{4.25}$$

Moreover, we use numerical integration schemes like Gauss quadrature for the numerical integration of the weak forms. The integral is evaluated depending on the total number $\tilde{k}$ of integration points ξ_k and the weights w_k as

$$\int f(\mathbf{x})\,\mathrm{d}v \approx \sum_{k=1}^{\tilde{k}} f(\mathbf{x}(\xi_k))J_r(\xi_k)w_k. \tag{4.26}$$

The Gauss quadrature can evaluate an integral containing the polynomials of order $(2\tilde{k}-1)$ with $\tilde{k}$ integration points exactly. For the number of integration points and the weights for different reference elements, the reader is referred to Stroud [87] and Zienkiewicz & Taylor [88].

4.4 Time Discretisation

After the spatial discretisation, the semi-discrete system can be formulated in an abstract manner. Therefore, all the degrees of freedom (nodal values) of each primary variable are gathered in the vector $\mathbf{u}$ yielding

$$\mathbf{u} = \left[\left(\mathbf{u}_S^1, p^1, n^{N1}, n^{S1} \right), ..., \left(\mathbf{u}_S^{N_N}, p^{N_N}, n^{NN_N}, n^{SN_N} \right) \right]^T. \tag{4.27}$$

Now, we make use of the abbreviation $(\cdot)' = (\cdot)'_S$ to obtain the semi-discrete initial-value problem of differential algebraic equations (DAE) in time

$$\boldsymbol{\mathcal{F}}(t, \mathbf{u}, \mathbf{u}') \quad \equiv \quad \mathbf{M}\mathbf{u}' + \mathbf{k}\mathbf{u} - \mathbf{f} \quad \stackrel{!}{=} \quad \mathbf{0}, \tag{4.28}$$

where $\boldsymbol{\mathcal{F}} = \mathbf{0}$ denotes the discretisation of the governing equations, $\mathbf{M}$ is the generalised mass matrix, $\mathbf{k}$ is the generalised stiffness matrix, and $\mathbf{f}$ is the external force vector. The initial conditions are given by $\mathbf{u}(t_0) = \mathbf{u}_0$, where t_0 is initial time. However, this semi-discrete system is still continuous in time and needs to be discretised in the time domain. We need a stable time integration scheme for the problem (4.28). An explicit time integration scheme will result in unstable solutions unless the time interval is quite small. Therefore, an implicit time integration scheme would be a more suitable choice. We choose the implicit (backward) Euler scheme included in the general class of Runge-Kutta methods, which is suitable for the solution of index-1 systems of DAE. We can now briefly review the implicit (backward) Euler scheme, which is based on the backward Taylor-series expansion. The time interval $\left[t_0, T\right]$ is divided into a finite number of sub-intervals $\left[t_{n-1}, t_n\right]$. An implicit Euler scheme discretise $\mathbf{u}'(t_n)$ as

$$\mathbf{u}'_n = \mathbf{u}'(t_n) = \frac{\mathbf{u}_n - \mathbf{u}_{n-1}}{\Delta t_n} = \frac{\Delta \mathbf{u}_n}{\Delta t_n} \quad \text{with} \quad \mathbf{u}_n = \mathbf{u}_{n-1} + \Delta \mathbf{u}_n, \tag{4.29}$$

where $\Delta t_n = t_n - t_{n-1}$. Inserting (4.29) in (4.28), we get a nonlinear system of equations because of $\mathbf{k}$ containing nonlinear dependencies on $\mathbf{u}$ where $\Delta \mathbf{u}_n$ appears in an implicit manner as

$$\boldsymbol{\mathcal{F}}(t, \mathbf{u}, \mathbf{u}') = \mathbf{0} \quad \longrightarrow \quad \boldsymbol{\mathcal{F}}(t_n, \mathbf{u}_{n-1} + \Delta \mathbf{u}_n, \frac{\Delta \mathbf{u}_n}{\Delta t_n}) =: \mathbf{R}_n(\Delta \mathbf{u}_n) = \mathbf{0}. \tag{4.30}$$

The non-linear functional $\mathbf{R}_n(\Delta \mathbf{u}_n)$ is solved using the Newton-Raphson scheme [2]. Therefore, the Jacobian (tangent) matrix is needed

$$\mathbf{J}_n = \frac{\mathrm{d}\,\mathbf{R}_n}{\mathrm{d}\,\Delta \mathbf{u}_n} = \left. \frac{\partial \boldsymbol{\mathcal{F}}}{\partial \mathbf{u}} \right|_z + \frac{1}{\Delta t_n} \left. \frac{\partial \boldsymbol{\mathcal{F}}}{\partial \mathbf{u}'} \right|_z, \tag{4.31}$$

where $z = (t_n, \mathbf{u}_n, \mathbf{u}'_n)$ represent the current set of arguments of $\boldsymbol{\mathcal{F}}$ in $\mathbf{R}_n$. Once the Jacobian is calculated, the current stage increment can be calculated as

$$\Delta \mathbf{u}_n^{k+1} = -(\mathbf{J}_n^k)^{-1} \mathbf{R}_n^k, \tag{4.32}$$

where k is the Newton iteration step. The solution vector $\mathbf{u}_n^{k+1}$ is then updated using

$$\mathbf{u}_n^{k+1} = \mathbf{u}_n^k + \Delta\mathbf{u}_n^{k+1}. \tag{4.33}$$

Newton iteration procedure can be applied at the current time step n until a convergence criterion like

$$\|\mathbf{R}_n^{k+1}\| < TOL_{\mathbf{R}} \tag{4.34}$$

is met.

4.5 Verification of Implementation

Initially, we implement a biphasic model to test the correct implementation and compare the results against the consolidation problem given in the PANDAS manual [89]. A similar example is also given in the book by Ehlers [39]. In this problem of water-saturated soil, cf. Figure 4.2, the load $\mathbf{q}(t)$ is increased to the maximum value of 15000 N/m for up to 20 seconds. Then, the load is kept constant at this value until the end of the simulation (t = 2000s).

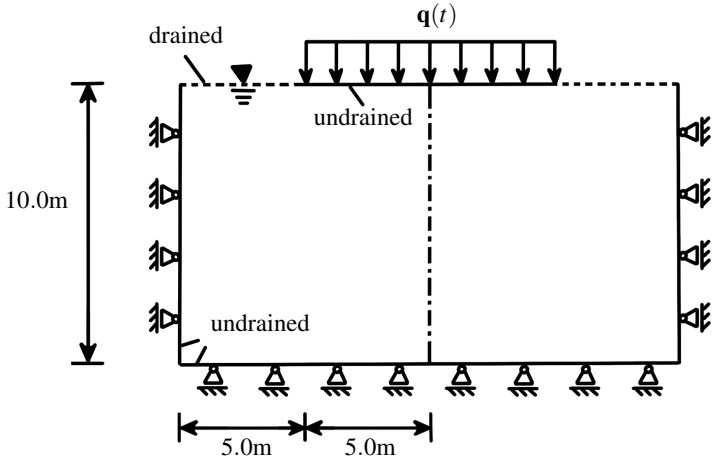

Figure 4.2: Geometry and boundary conditions for the consolidation problem.

The boundary conditions for the problem can be seen in Figure 4.2. The top edge has drained and undrained surfaces, and all the other surfaces are undrained. The left/right and the bottom edges are fixed in the x and y directions, respectively. The governing equations for the biphasic model can be obtained by considering only the solid and fluid phases and mass exchange $\hat{\rho}^S = 0$. Therefore, the momentum balance and volume balance of the mixture are used. The analytical integration of the solid volume balance (3.18) gives the

relation (4.39). The nutrient volume balance and the stabilisation scheme are not needed. Furthermore, we use simplified Darcy's law and Cauchy stress. The governing equations for the biphasic consolidation are summarised as

• Momentum balance of mixture:

$$\mathcal{G}_{\mathbf{u}_S} = \int_\Omega (\mathbf{T}) : \operatorname{grad} \delta\mathbf{u}_S \,\mathrm{d}v - \int_\Omega (\rho^S + \rho^F)\,\mathbf{b} \cdot \delta\mathbf{u}_S \,\mathrm{d}v - \int_{\Gamma_\mathbf{t}} \mathbf{t} \cdot \delta\mathbf{u}_S \,\mathrm{d}a = 0. \tag{4.35}$$

• Volume balance of mixture:

$$\mathcal{G}_p = \int_\Omega \operatorname{div} \mathbf{x}'_S \,\delta p \,\mathrm{d}v - \int_\Omega n^F \mathbf{w}_{FS} \cdot \operatorname{grad} \delta p \,\mathrm{d}v + \int_{\Gamma_q} \underbrace{n^F \mathbf{w}_{FS} \cdot \mathbf{n}}_{:=q} \,\delta p \,\mathrm{d}a = 0. \tag{4.36}$$

• Darcy's filter law

$$n^F \mathbf{w}_{FS} = -\frac{k^F_{OS}}{\gamma^{FR}} \left(\operatorname{grad} p - \rho^{FR}\mathbf{b}\right). \tag{4.37}$$

• Cauchy stress

$$\mathbf{T} = \mathbf{T}^S_E - p\mathbf{I}, \quad \text{where} \quad \mathbf{T}^S_E = \frac{1}{J_S}\Big\{\mu^S(\mathbf{b}_S - \mathbf{I}) + \lambda^S (ln J_S)\mathbf{I}\Big\}. \tag{4.38}$$

• Solid volume fraction

$$n^S = n^S_{OS} J_S^{-1} \quad \rightarrow \quad n^F = 1 - n^S. \tag{4.39}$$

Parameter	Symbol	Value	Unit
Lam*é* constant	μ^S	5.58×10^6	N/m^2
Lam*é* constant	λ^S	8.38×10^6	N/m^2
Darcy's permeability fluid	k^F_{OS}	1×10^{-4}	m/s
Effective fluid weight	γ^{FR}	1×10^4	N/m^3
Realistic density solid	ρ^{SR}	2×10^3	kg/m^3
Realistic density fluid	ρ^{FR}	1×10^3	kg/m^3
Initial solid volume fraction	n^S_{OS}	0.67	–

Table 4.1: Parameters for consolidation problem.

Due to the symmetry, only the left half of the geometry is discretised. A quadratic approximation is chosen for the solid displacements and a linear approximation for the pressure. The geometry is prepared and discretised in the program package CUBIT [90] and can be imported to PANDAS [89], cf. Figure 4.3. The material parameters used for the consolidation problem are given in Table 4.1. As the pressure profile is given in the PANDAS

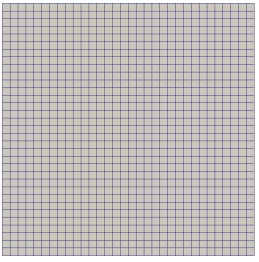

Figure 4.3: Discretisation of left half of the geometry with 1056 elements.

manual, we compare the results to confirm the correct implementation of the biphasic model. Due to the load on the soil, the pressure builds up in the soil. However, this pressure decreases to the value of $p = 0$ with the time approaching infinity ($t \to \infty$). This is because of the outflow of the water through the drained surface at the top, cf. Figure 4.4.

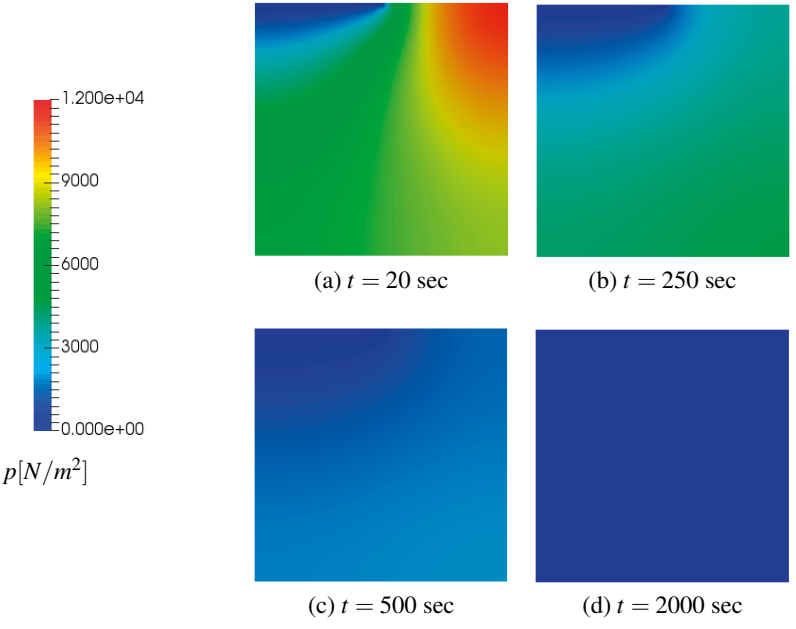

Figure 4.4: Pressure profiles in the water-saturated soil at the time (a) 20 sec, (b) 250 sec, (d) 500 sec and (c) 2000 sec.

Furthermore, we implement a triphasic growth model presented by Ricken & Bluhm [56] and compare the results for verification. This example presents the characteristic of adaptation of internal structure. The structures are formed where it is necessary for stability. Figure 4.5 represents a cantilever beam fixed on the left side in the x and y directions. A load of 4N is applied at the bottom right edge of the beam. The governing equations (4.11) - (4.14), stress equation (3.79), and Darcy's law (3.64) for the triphasic model are used. Furthermore, we use the equation (4.40) for the solid mass production as a function of nutrient volume fraction n^N and solid Jacobian J_S. We focus on case three presented in [56], where the solid mass production does not depend on the von Mises or Rankine stress measures.

• Solid mass production:

$$\begin{aligned} \hat{\rho}^S &= \hat{\rho}^S(n^N, J_S) = \mathcal{C}\, \hat{\rho}^S_{n^N}(n^N)\, \hat{\rho}^S_{J_S}(J_S), \\ \hat{\rho}^S_{n^N}(n^N) &= -exp\{-\kappa_{n^N}(n^N)^2\} + 1, \\ \hat{\rho}^S_{J_S}(J_S) &= -exp\{-\kappa_{J_S}(J_S - 1)^2\} + 1, \end{aligned} \tag{4.40}$$

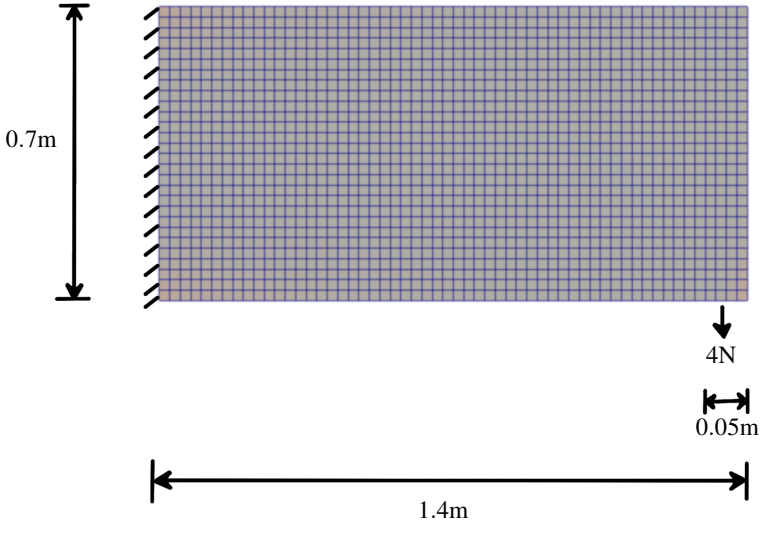

Figure 4.5: Geometry and boundary conditions for the triphasic problem.

Parameter	Symbol	Value	Unit
Lam*é* constant	μ^S	1.0×10^4	N/m^2
Lam*é* constant	λ^S	2.0×10^3	N/m^2
Darcy's permeability fluid	k_{OS}^F	8.3×10^5	m/d
Effective fluid weight	γ^{FR}	1×10^4	N/m^3
Realistic density solid	ρ^{SR}	2.0	kg/m^3
Realistic density liquid	ρ^{LR}	1.0	kg/m^3
Realistic density nutrient	ρ^{NR}	2.0	kg/m^3
Initial solid volume fraction	n_{OS}^S	0.5	–
Initial nutrient volume fraction	n_{OS}^N	0.4	–
Maximum mass exchange	$\mathcal{C}$	10	kg/dm^3
Material paramaeter	κ_{n^N}	5.0	–
Material paramaeter	κ_{J_S}	2.0×10^{-6}	–
Material paramaeter	n	2.0	–
Material paramaeter	m	0.0	–

Table 4.2: Parameters for triphasic problem.

A quadratic approximation is chosen for the solid displacements and a linear approximation for the pressure, nutrient volume fractions, and solid volume fractions. The geometry is discretised in CUBIT (1568 elements), which is then imported to PANDAS. The parameters used for the simulation are mentioned in Table 4.2 where d represents days. Now, we compare the solid volume fraction plots to confirm the correct implementation of the triphasic growth model. The increase in solid volume fraction depends on the availability of the nutrients, cf. (3.8), and the volumetric deformation. It can be seen that the inner structure adjusts itself to form an optimal structure in response to the given load, cf. Figure 4.6.

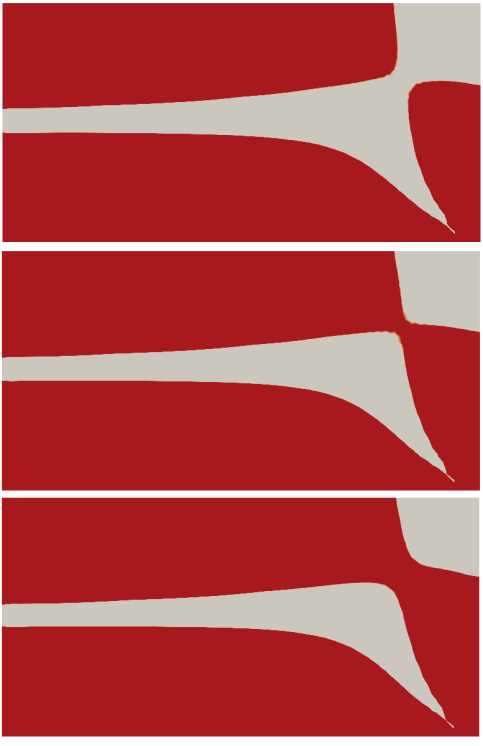

Figure 4.6: Structure optimisation: red and white areas represent high and low mass content, respectively.

5 MODELLING OF THROMBOSIS

In this chapter, we present the application of the developed model for thrombosis using two-dimensional geometries. The constitutive equations for the solid stress $\mathbf{T}^S$, the mass production term $\hat{\rho}^S$, and the seepage velocity $\mathbf{w}_{FS}$ provide the thrombus-specific material laws. In addition, the coupled set of governing equations presents the capabilities of the model. The model is implemented in the FE code PANDAS, a finite element package designed to solve strongly coupled multiphase porous media problems. However, modelling the growth of living tissues has its challenges. In the case of thrombosis, it is not straightforward to obtain the data and perform experiments on living tissues. Therefore, the parameters are chosen that give reasonable results.

Although the preceding chapters deal with the triphasic model, we first implement a biphasic model by introducing the growth in the model. We test it for the case of type B Aortic Dissection (AD) using an idealised 2-d rectangular geometry. Furthermore, considering the crucial role nutrients play in the growth and formation of thrombus, we implement the triphasic model presented in this monograph for the idealised geometry. We study the effects of various parameters on mass exchange and then give a numerical example using the chosen parameters. Finally, the model is applied to a realistic 2-d cross-section of a false lumen obtained from a 3-d model of an aorta to present the model's usefulness in actual cases while drawing an analogy to thrombosis.

5.1 Biphasic Model

In this section, we expand the biphasic model presented in Section 4.5 for the application of thrombus formation and growth in type B AD. For the presented numerical example, we replace the geometry of the false lumen with an idealised rectangular 2-d geometry. It consists of a solid matrix saturated with fluid. The dimensions of the false lumen are considered in the physiological range, and the boundary conditions can be seen in Figure 5.1 [91–94]. The right and bottom walls are fixed in the x and y directions, respectively. There is an entry tear at the top left wall from where the fluid enters the false lumen. We apply a Neumann boundary condition for fluid volume efflux $q = 0.1$ m/s. The dotted line (drained surface) at the bottom left wall represents the exit tear from where the fluid is allowed to exit ($p = 0.0$ N/m^2), which is the only drained surface. All the other boundaries are undrained surfaces.

For the presented problem with only solid and liquid phases ($n^F = 1 - n^S$), we want to measure the growth of the thrombus. As mentioned in the preceding chapter, we can introduce solid volume fraction n^S as an additional field variable to calculate the growth process globally, and the solid volume balance can be used as the governing

equation for n^S. Therefore, the set of equations includes the balance equations (4.11), (4.12), and (4.14), Cauchy stress (3.79), and Darcy's filter law (3.64) for the thrombus growth model. In addition, we need to reformulate the mass exchange rate $\hat{\rho}^S$ (3.67) to allow growth in the biphasic model as

$$\hat{\rho}^S = \hat{\rho}^S(\mathbf{w}_{FS}) = \mathcal{C}\, exp\{-\|\mathbf{w}_{FS}\|^2/\beta_1\}. \tag{5.1}$$

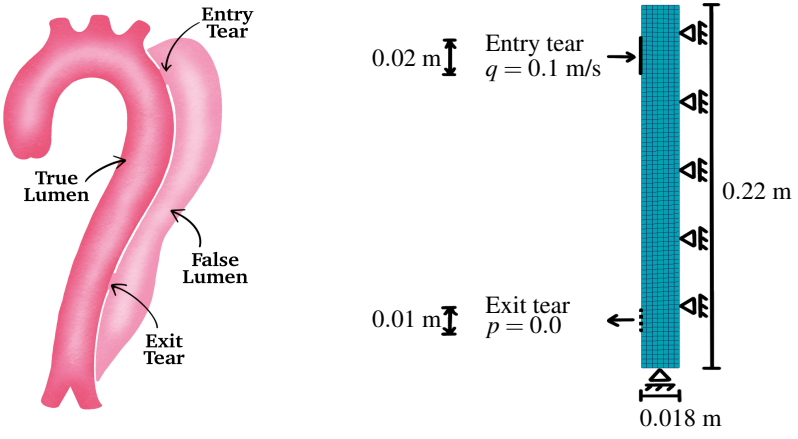

Figure 5.1: Illustration of type B AD (left), boundary conditions and discretization of false lumen for biphasic model (right).

Parameter	Symbol	Value	Unit
Lamé constant	μ^S	1×10^5	N/m^2
Lamé constant	λ^S	0.0	N/m^2
Dynamic fluid viscosity	μ^{FR}	1×10^{-3}	Ns/m^2
Initial darcy permeability fluid	k^F_{OS}	1×10^{-6}	m/s
Maximum mass exchange	$\mathcal{C}$	5×10^{-2}	kg/sm^3
Realistic density solid	ρ^{SR}	2×10^3	kg/m^3
Realistic density fluid	ρ^{FR}	1×10^3	kg/m^3
Initial solid volume fraction	n^S_{OS}	0.2	-
Material parameter	β_1	0.05	-
Material paramaeter	n	3.0	–
Material paramaeter	m	3.0	–

Table 5.1: Parameters for thrombus growth.

We discretized the geometry using CUBIT and implemented the equations in PANDAS. The mesh consists of 560 elements. A quadratic approximation is used for the solid displacements $\mathbf{u}_S$ and linear approximation for the pressure p and solid volume fraction n^S. Furthermore, we assume zero Poisson's ratio ($\lambda^S = 0$) for the solid skeleton. The simulation is performed using the parameters mentioned in Table 5.1 [57, 58, 95–97] with a time step size of 100 seconds. Due to the fluid entering through the entry tear and exiting through the exit tear, there are high seepage velocity regions in the middle and low velocity regions at the top and bottom, cf. Figure 5.3. The mass exchange formulation (5.1) leads to high growth of thrombus in the regions with low seepage velocity (top and bottom) and vice versa, following the Figure 3.2 (left). This can be seen in Figure 5.2, where the false lumen has an initial solid volume fraction of 0.2 at time $t = 0$ hours. The thrombus grows more in the top and bottom regions with time, cf. Figure 5.2.

(a) $t = 0$ hours (b) $t = 41$ hours (c) $t = 83$ hours

Figure 5.2: Solid volume fraction n^S (right) at different times for the biphasic model.

In Figure 5.3, we can see that the norm of the seepage velocity increases with time. This is because as the solid volume fraction increases, there is less space available (decrease in pore area) for the fluid to flow. This also leads to an increase in the pressure gradient. Consequently, there is an increase in the velocity following Darcy's filter law and the continuity of the flow. Moreover, we observe a singularity at the exit tear due to the sharp edges, which is a numerical artefact [98–100]. We zoom in on the exit tear in Figure 5.3 (b) and observe what happens in the case of coarse mesh (285 elements), fine mesh (560 elements) and finest mesh (1035 elements). Figure 5.4 represents the seepage velocity, and the black line represents the exit tear. Here, we can see that the sharp edge at the exit tear results in singularity where the peak in the values is localised. The smaller the size of the element, the higher the seepage velocity value. The results will not converge if the element

size is extremely small, as the solution tends toward an infinite value.

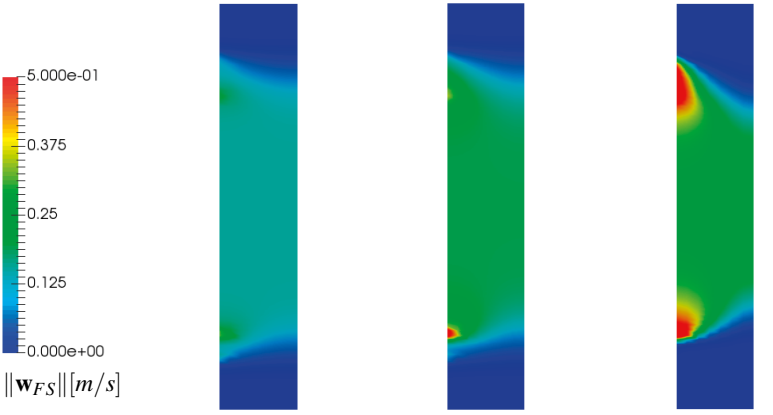

(a) $t = 0$ hours (b) $t = 41$ hours (c) $t = 83$ hours

Figure 5.3: Norm of the seepage velocity at different times for the biphasic model.

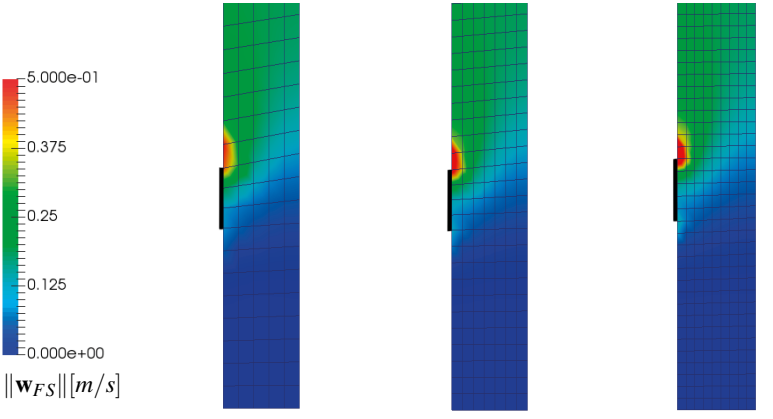

(a) coarse mesh (b) fine mesh (c) finest mesh

Figure 5.4: Singularity at the exit tear at time $t = 41$ hours for the seepage velocity.

Moreover, we know from the literature that poor mass conservation creates numerical and stabilisation issues [101, 102]. Therefore, we test the mass conservation in a closed initial boundary value problem (IBVP) with the mass exchange between the solid and fluid

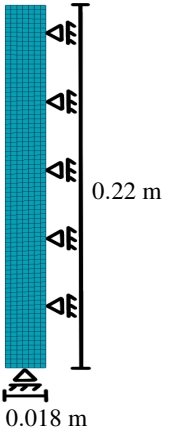

Figure 5.5: Boundary conditions and discretisation of closed IBVP.

phases. The boundary conditions and discretisation (560 elements) for the problem are shown in Figure 5.5. We perform the simulations for three different cases of $\rho^{\alpha R}[kg/m^3]$: (a) $\rho^{SR} = 2000 > \rho^{FR} = 1000$, (b) $\rho^{SR} = 1000 < \rho^{FR} = 2000$, and (c) $\rho^{SR} = \rho^{FR} = 1000$. The rest of the material parameters are taken from Table 5.1. Looking at the mass plots over the time 60,000 seconds, cf. Figure 5.6, we observe that the mass $(n^S \rho^{SR} + n^F \rho^{FR}) J_S$ over the domain remains approximately constant. There are deviations of 0.11%, 0.09%, and 0% in cases (a), (b), and (c), respectively. However, these errors can be reduced by refining the mesh further.

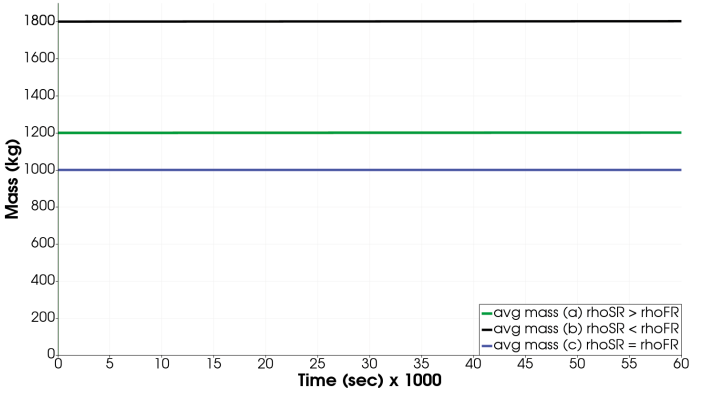

Figure 5.6: Average mass over the whole domain.

5.2 Triphasic Model

In this section, we expand the biphasic model to the triphasic model for thrombosis, discussed in previous chapters. We use the idealised rectangular 2-d geometry for the numerical example, cf. Figure 5.7. It consists of a solid matrix saturated with fluid, consisting of liquid and nutrient phases. The boundary conditions can be seen in Figure 5.7. The dotted line at the bottom left wall represents the exit tear. The exit tear is a drained surface ($p = 0$) from where the fluid is allowed to exit. The rest of the boundaries are undrained surfaces. We apply boundary condition for the fluid volume efflux $q = n^F \mathbf{w}_{FS} \cdot \mathbf{n}$ at the Neumann boundary Γ_q at the entry tear. Also, the nutrient volume fraction n^N is fixed at the entry tear. The right and bottom walls are fixed in the x and y directions, respectively. For the presented problem with solid, liquid and nutrient phases, we want to measure the growth of the thrombus. Therefore, we have solid volume fraction n^S as the primary variable. Furthermore, we consider the nutrient phase to include the influence of the nutrients in the growth process, as discussed in this monograph. Therefore, the set of equations consists of balance equations (4.11) - (4.14), Cauchy stress (3.79), Darcy's filter law (3.64), and mass exchange formulation (3.67).

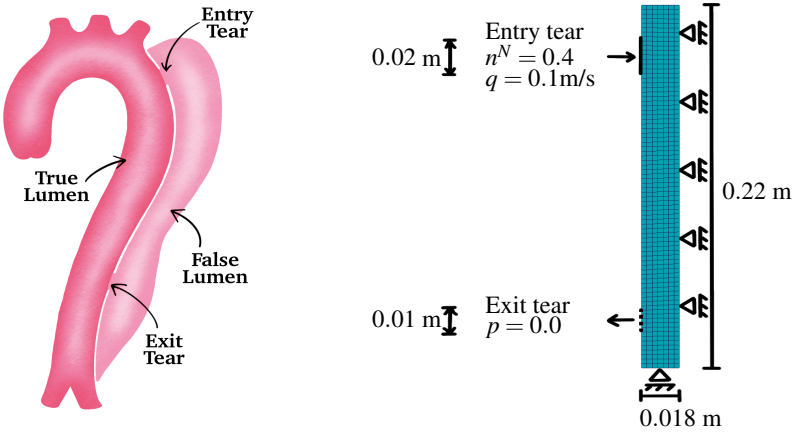

Figure 5.7: Illustration of type B AD (left), boundary conditions and discretization of false lumen (right).

We discretize the geometry using CUBIT and implement the equations in PANDAS. A quadratic approximation is used for the solid displacements $\mathbf{u}_S$ and linear approximation for the pressure p, solid volume fraction n^S, and nutrient volume fraction n^N. We assume zero Poisson's ratio ($\lambda^S = 0$) for the solid skeleton. The simulations are performed using the material parameters given in Table 5.2 [57, 58, 95–97] with a time step size of 100 seconds.

Parameter	Symbol	Value	Unit
Lam*é* constant	μ^S	1×10^5	N/m^2
Lam*é* constant	λ^S	0.0	N/m^2
Dynamic fluid viscosity	μ^{FR}	1×10^{-3}	Ns/m^2
Initial darcy permeability fluid	k^F_{OS}	1×10^{-6}	m/s
Maximum mass exchange	$\mathcal{C}$	5×10^{-2}	kg/sm^3
Realistic density solid	ρ^{SR}	2×10^3	kg/m^3
Realistic density fluid	ρ^{FR}	1×10^3	kg/m^3
Realistic density nutrients	ρ^{NR}	2×10^3	kg/m^3
Initial solid volume fraction	n^S_{OS}	0.2	-
Initial nutrient volume fraction	n^N_{OS}	0.4	-
Material paramaeter	n	3.0	–
Material paramaeter	m	3.0	–

Table 5.2: Parameters for thrombus growth.

Now, we want to analyse the quality of spatial discretisation. Therefore, we discretise the geometry with (a) 111, (b) 285, (c) 560, and (d) 1035 elements, cf. Figure 5.8. Firstly, we plot the average value of solid volume fraction n^S in the whole domain and compare the results. We can observe that the average solid volume fraction converges to the values between 0.71 and 0.72 in Figure 5.9 (left). In the zoomed-in version of the plot, we can see that the values for meshes (a) and (b) are further away compared to meshes (c) and (d).

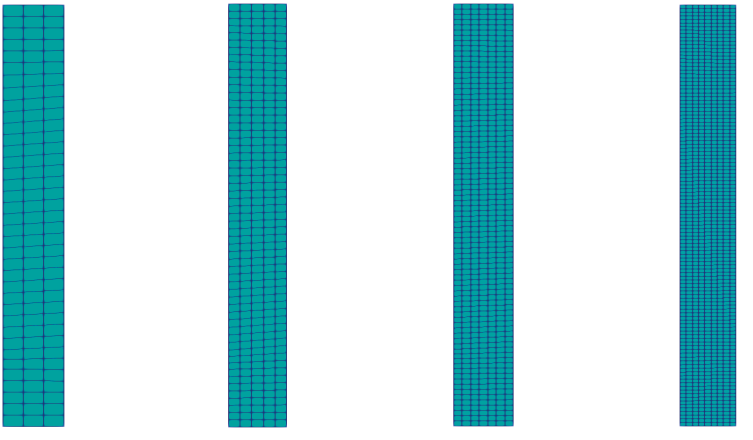

(a) 111 elements (b) 285 elements (c) 560 elements (d) 1035 elements

Figure 5.8: Discretisation of geometry with different mesh sizes.

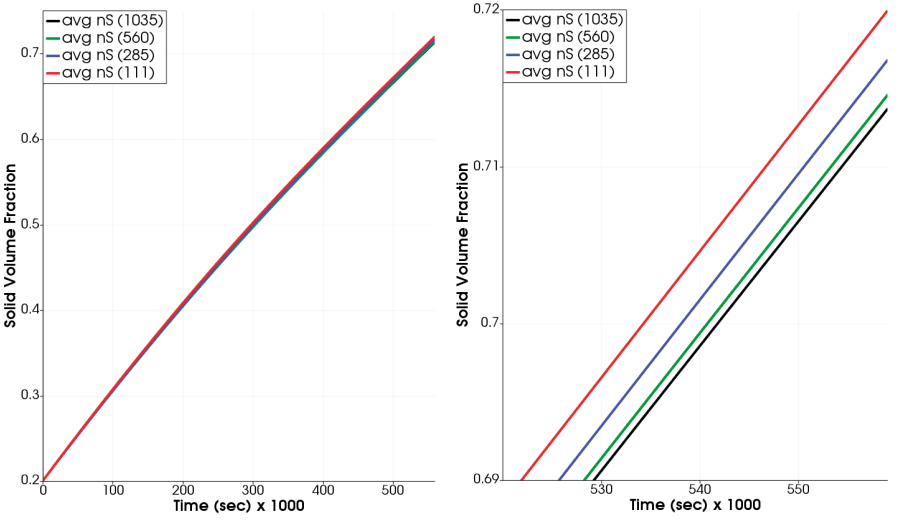

Figure 5.9: Convergence study of the average solid volume fraction over the whole domain with complete (left) and zoomed-in (right) plots.

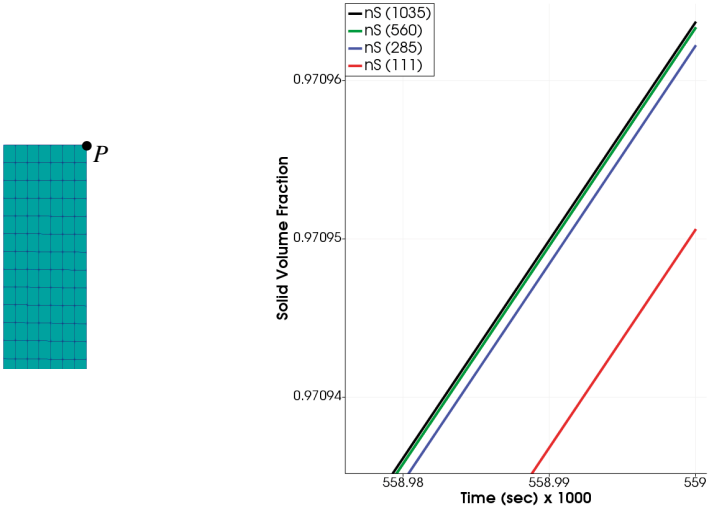

Figure 5.10: Convergence study of the solid volume fraction at point P (left) with zoomed-in plot (right).

Furthermore, we analyse the point P at the top right corner of the domain. It is one of the most critical points with the highest volume fraction, cf. Figure 5.10 (left). We can observe from the plot, cf. Figure 5.10 (right), that the values of the solid volume fraction at point P converge for meshes (c) and (d). Therefore, from the analysis of the whole domain and the point P, we conclude that the solution converges for the meshes (c) and (d) with 560 and 1035 elements, respectively, very well. In order to keep the size of the system reasonable, we choose the mesh (c) with 560 elements for further simulations. Moreover, the set of equations is solved in a monolithic manner with an implicit Euler time-integration scheme. This implicit time integration scheme has been tested from the time step size of 10 seconds up to 100,000 seconds, which gives us a stable and robust simulation tool [103].

Now, we need to study the influence of material parameters β_1 and β_2 in the growth dependencies $\hat{\rho}^S_{\mathbf{w}_{FS}}$ and $\hat{\rho}^S_{n^N}$ (3.67) and the Neumann boundary condition q in order to choose the appropriate values of these parameters.

5.2.1 Influence of Material Parameters in Mass Exchange

We can vary the material parameters β_1 and β_2 in $\hat{\rho}^S(\mathbf{w}_{FS}, n^N)$ (3.67) to change the dependence of mass exchange rate $\hat{\rho}^S$ on the seepage velocity and the nutrient volume fraction. At first, we vary the values of β_1 as shown in Figure 5.11. By varying the values of β_1, we change the range of the seepage velocity for which the growth happens. Now, we use the material parameters mentioned in Table 5.2, $\beta_2 = 5.0$, and the boundary condition $q = 0.1$ m/s to perform the simulation for thrombosis in the false lumen. Due to the fluid volume efflux, the fluid enters from the entry tear and is allowed to leave from the exit tear. This results in high velocities in the middle regions and low velocities at the top and the bottom sections, cf. Figure 5.16. Because of this, we can see in Figure 5.12 that the middle sections are the most difficult to form the thrombus. Therefore, as we increase the value of β_1, forming a thrombus is easier due to growth happening for the wider range of seepage velocities. This presents the influence of changing the dependence of seepage velocity $\mathbf{w}_{FS}$ on growth.

Furthermore, we can vary the material parameter β_2 and change the dependence of the mass exchange rate on the nutrient volume fraction as shown in Figure 5.13. We perform the simulation using the material parameters given in the table 5.2, $\beta_1 = 0.05$, and the Neumann boundary condition $q = 0.1$ m/s. As we change the value of β_2, we allow the thrombus growth for a more extensive range of nutrient volume fraction n^N. This leads to faster growth of the thrombus, cf. Figure 5.14. However, due to low velocities at the top and bottom, the growth remains higher in these sections. This presents the influence of changing the dependence of nutrient volume fraction on growth.

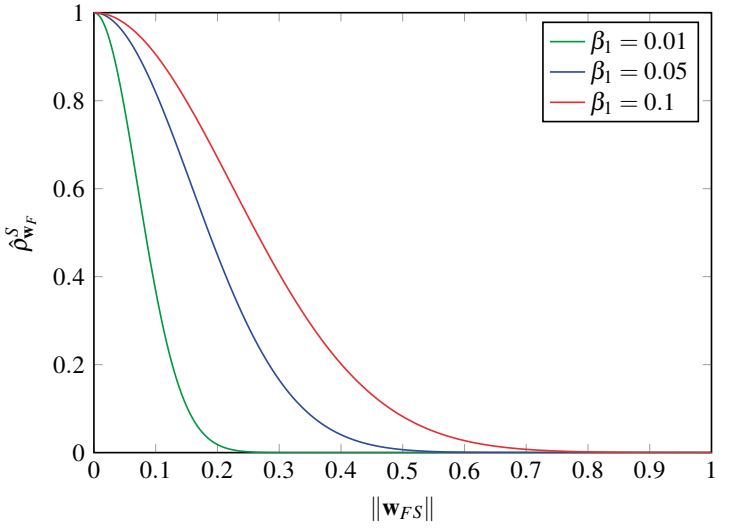

Figure 5.11: Variation in mass exchange rate dependence $\hat{\rho}^S_{\mathbf{w}_{FS}}$ on the seepage velocity $\mathbf{w}_{FS}$.

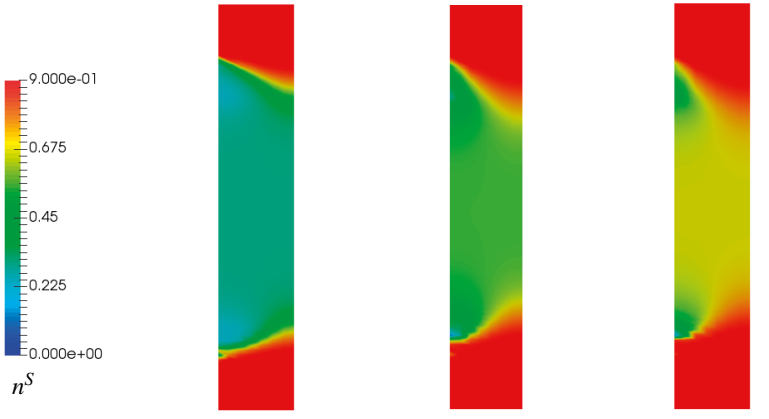

(a) $\beta_1 = 0.01$ (b) $\beta_1 = 0.05$ (c) $\beta_1 = 0.1$

Figure 5.12: Change in solid volume fractions n^S for different values of β_1 at 168 hours.

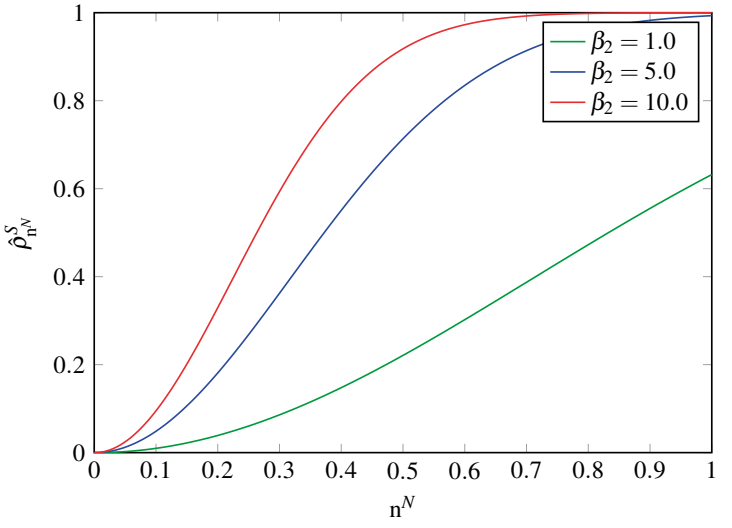

Figure 5.13: Variation in mass exchange rate dependence $\hat{\rho}^S_{n^N}$ on the nutrient volume fraction n^N.

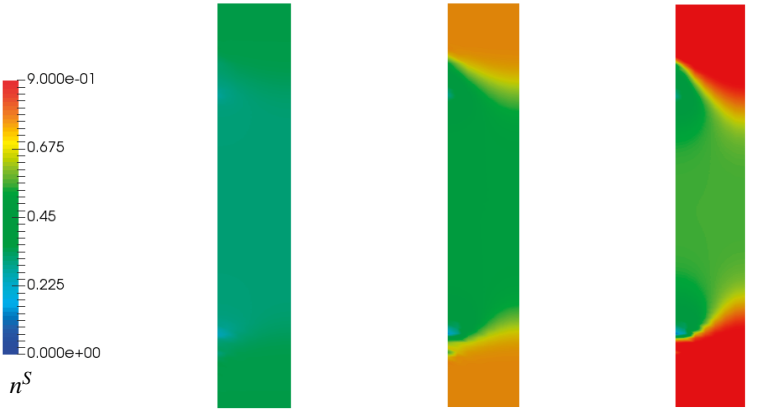

(a) $\beta_2 = 1.0$ (b) $\beta_2 = 5.0$ (c) $\beta_2 = 10$

Figure 5.14: Change in solid volume fractions n^S for different values of β_2 at 120 hours.

5.2.2 Effect of Neumann Boundary Condition

Moreover, we can see the effects due to variation in the fluid volume efflux $q = n^F \mathbf{w}_{FS} \cdot \mathbf{n}$ on the Neumann boundary Γ_q. The simulation is performed using the parameters given in Table 5.2, $\beta_1 = 0.05$, and $\beta_2 = 5.0$. An increase in the fluid volume efflux q at the entry tear results in higher seepage velocity in a wider region. Therefore, it is challenging to form a thrombus in the false lumen because of the mass exchange rate dependence on the seepage velocity $\mathbf{w}_{FS}$, cf. Figure 5.15. A low value of q results in lower velocities leading to the easier formation of a thrombus. This also fits well with the physiological understanding of thrombosis and the Virchow triad, where it is challenging to form blood clots when the blood velocity is high [14].

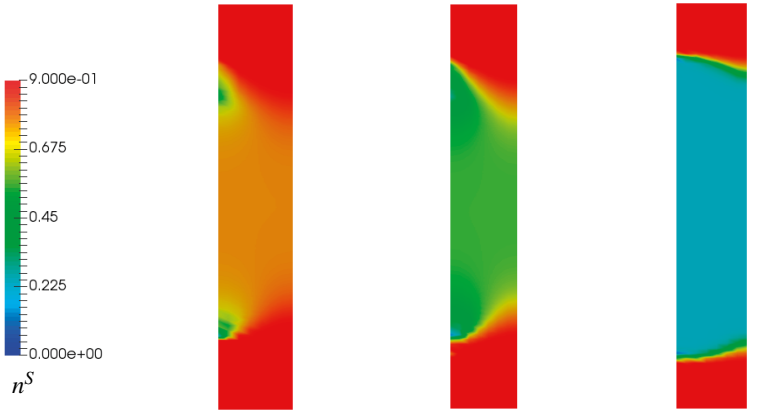

(a) $q = 0.05$ m/s (b) $q = 0.1$ m/s (c) $q = 0.5$ m/s

Figure 5.15: Change in solid volume fractions n^S for different values of q at 168 hours.

The above studies show that different results can be achieved by varying the parameters. The values of the parameters can be changed depending on the specific case. However, we choose the intermediate values of the parameters for performing further simulations to avoid extreme cases.

Numerical Example with chosen Parameters

All the foundations for the triphasic thrombus growth model are laid in Section 5.2. We use the same problem description (cf. Figure 5.7) and governing equations for the 2-d numerical example. We use the material parameters given in Table 5.2, $\beta_1 = 0.05$, $\beta_2 = 5.0$, and Neumann boundary condition $q = 0.1$ m/s to perform the simulation using PANDAS with a time step size of 100 seconds.

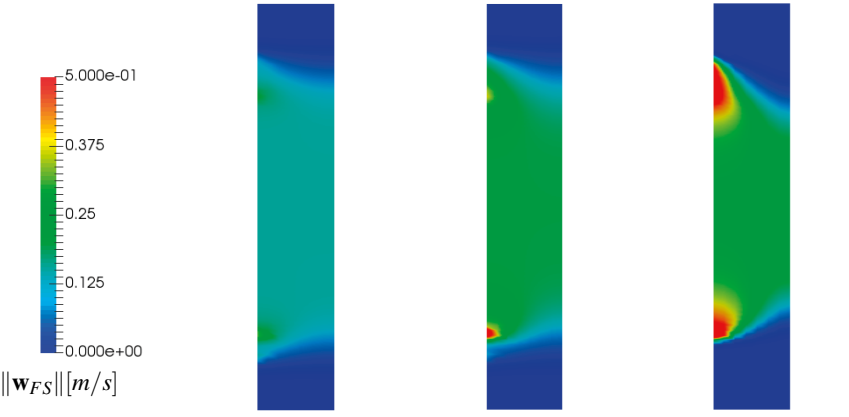

(a) t = 0 hours (b) t = 84 hours (c) t = 168 hours

Figure 5.16: Norm of the seepage velocity at different stages in time.

(a) t = 0 hours (b) t = 84 hours (c) t = 168 hours

Figure 5.17: Change in solid volume fractions n^S at different stages in time.

Because the fluid enters through the entry tear and exits through the exit tear, there are high seepage velocity regions in the middle and low velocity regions at the top and bottom, cf. Figure 5.16. This leads to an increase in solid volume fraction because of different velocity profiles and the availability of nutrients, cf. Figure 5.17. Moreover, we can see how the effective permeability changes as the thrombus grow. The effective permeability

$K_E^S = (n^F/n_{0S}^F)^m K_{0S}^S$ accounts for the permeability due to change in volume fractions (cf. Section 3.2.5). This means that with the increase in solid volume fraction $n^F = 1 - n^S$, i.e., thrombus growth, there is more solid, and the ability of the fluid to move through the porous media decreases, cf. Figure 5.18.

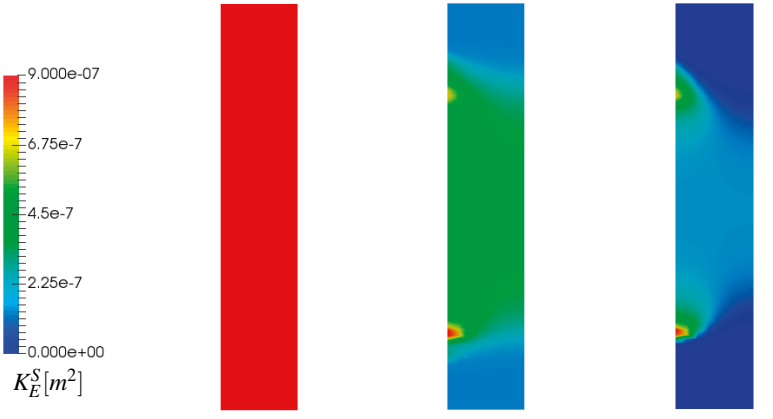

(a) t = 0 hours (b) t = 84 hours (c) t = 168 hours

Figure 5.18: Effective permeability at the time (a) 0 hours, (b) 84 hours, and (c) 168 hours

5.2.3 Realistic Geometry

After choosing the parameters for the triphasic model, we want to use a 2-d cross-section of a realistic geometry to model thrombosis. To obtain the cross-section, we use a 3-d model of an aorta consisting of a true and false lumen [104], cf. Figure 5.19 (left). We cut this model in the x-y plane represented as the cutting plane in Figure 5.19 (top right). This gives us the 2-d geometry in the x-y plane, cf. Figure 5.19 (bottom right).

However, because we are modelling thrombosis in the false lumen, the geometry of the false lumen is of interest to us. Therefore, we create and discretise the false lumen's geometry using CUBIT, consisting of 1063 elements, cf. Figure 5.20. The geometry consists of a solid matrix saturated with fluid, consisting of liquid and nutrient phases. Furthermore, we arbitrarily chose the entry and exit tears position. The boundary conditions at the entry tear include $n^S = 0.4$ and $q = 0.1$ m/s. The bottom exit tear (dotted line) is the drained surface with $p = 0.0$ N/m^2. The rest of the boundaries are undrained surfaces, cf. Figure 5.20. Also, the right side of the false lumen is fixed in both the x and y directions. There are no other displacement or traction boundary conditions. Furthermore, we use the balance equations (4.11) - (4.14), Cauchy stress (3.79), Darcy's filter law (3.64), and mass exchange formulation (3.67), discussed for the triphasic model. A

quadratic approximation is used for the solid displacements $\mathbf{u}_S$ and linear approximation for the pressure p, solid volume fraction n^S, and nutrient volume fraction n^N. The simulation is performed using the parameters given in Table 5.2 along with $\beta_1 = 0.05$ and $\beta_2 = 5.0$ and with a time step size of 100 seconds.

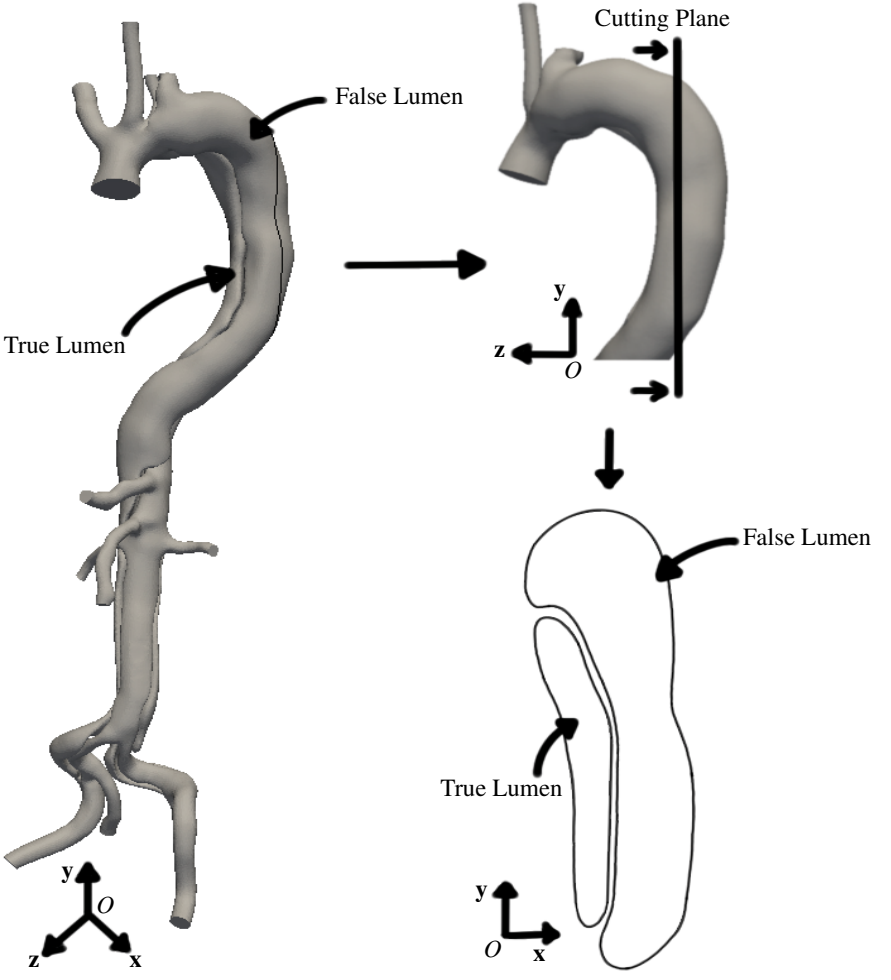

3-d Geometry 2-d cross-section

Figure 5.19: 3-d model of the aorta with a true and false lumen (left) [104]. Cutting plane and the resulting 2-d cross-section of the lumens (right).

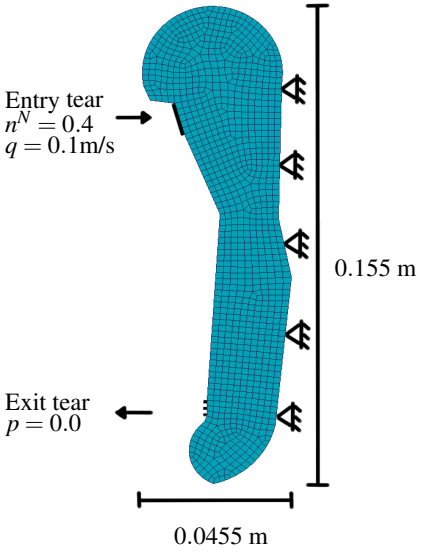

Figure 5.20: Discretisation and boundary conditions of the false lumen.

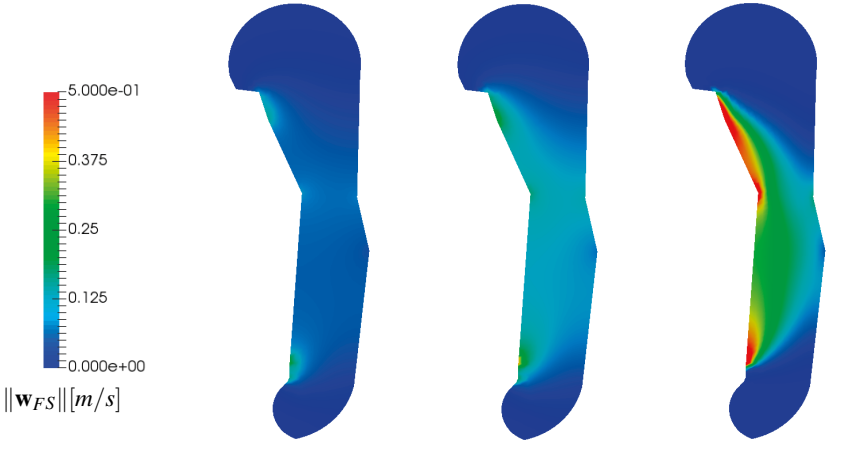

(a) t = 0 hours (b) t = 41 hours (c) t = 83 hours

Figure 5.21: Norm of the seepage velocity at different stages in time.

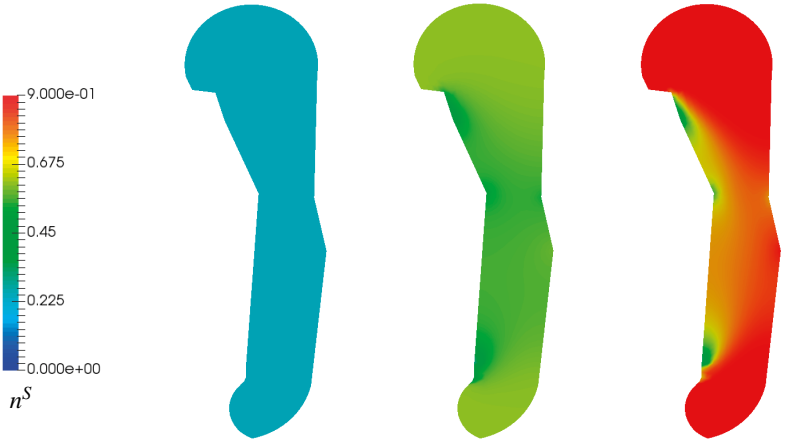

(a) t = 0 hours (b) t = 41 hours (c) t = 83 hours

Figure 5.22: Change in solid volume fractions n^S at different stages in time.

We can now discuss the results while drawing an analogy with the process of thrombosis. At time $t = 0$ hours, the initial solid volume fraction n^S is 0.2 because of the presence of subendothelial collagen, wall cells and activated platelets on the formation of the false lumen. As the fluid enters via the entry tear, it creates high and low-velocity regions, cf. Figure 5.21. Because of different velocity profiles and the availability of nutrients, the process of thrombus begins, and the solid volume fractions start increasing, cf. Figure 5.22. This can be compared to primary haemostasis, where the platelets accumulate at the injury site, they form a platelet plug. The solid volume fraction n^S increases further due to the mass exchange rate (3.67) dependence on seepage velocity $\mathbf{w}_{FS}$ and nutrient volume fraction n^N, which can be compared to secondary haemostasis. During secondary haemostasis, the clotting factors interact in a complicated series of chemical reactions leading to the formation of fibrin fibre. The platelets and the fibrin fibre form a mesh leading to the development of a stable plug. This process continues further to form a permanent solid plug called a thrombus. Furthermore, on comparing the results in Figure 5.17 and Figure 5.22, we see that a much fuller growth of thrombus, also along the left wall, is obtained using the realistic geometry proving the usefulness of the model in real cases. However, the singularity still exists at the exit tear.

Furthermore, we can see that the triphasic model accommodates the well-known Virchow triad, which describes three physiological factors that can result in thrombosis. The first one, endothelial injury, is included in the form of the presence of a false lumen. On the formation of a false lumen, the endothelium is damaged, which lines the inner layer of the blood vessels. The endothelial injury stimulates the platelets and coagulation

process. The second factor is hypercoagulability, which is an increased tendency of coagulation in the body due to inherited or acquired disorders. The material parameter C (maximum mass exchange) can be used to adapt the model for such a scenario. Also, the material parameter β_2 can be used to include this increased tendency of coagulation. The third factor, the stasis of blood, is present in the form of mass exchange dependency on the seepage velocity. Here, the material parameter β_1 can be used to adapt the model for the specific case. Section 5.2.1 shows the influence of the parameters β_1 and β_2 in the model. Finally, the fluid mass efflux q boundary condition can be used to incorporate the factor of high blood pressure, which is known to be the major cause of Aortic Dissection.

6 SUMMARY AND OUTLOOK

6.1 Summary

The goal of this monograph was to develop a model capable of describing the growth of the thrombus and its non-linear behaviour. A brief overview of thrombosis is presented in Section 1.1 to understand the process from the biological point of view. The subendothelial collagen, activated platelets, fibrin, blood, deactivated platelets and the clotting factors play a significant role in thrombosis. Virchow's triad describes the physiological factors that can result in thrombosis.

It was necessary to consider the multiphasic nature of the thrombus to model its growth because of the complex microscopic composition. However, a highly complicated microscopic model would prevent us from establishing a usable computational model. Therefore, we used a macroscopic continuum-mechanical approach of the Theory of Porous Media (TPM) to develop a thermodynamically consistent model. TPM provides an excellent framework to describe the aggregate as a combination of solid and fluid phases. The fluid phase further consists of liquid and nutrient phases, which gives us a triphasic aggregate.

We presented the general approach of TPM, including the kinematic relations and the balance principles for the multi-phase materials based on Truesdell's metaphysical principles. Furthermore, we needed constitutive relations to characterise the behaviour of the thrombus growth. Consequently, we introduced the necessary assumptions and adapted the balance equations accordingly. To characterise the material behaviour, we introduced the missing constitutive relations by evaluating the entropy inequality and obtaining the required restrictions. In this regard, the solid part was modelled using a modified Neo-Hookean model. Darcy's law describes the flow of fluids. Furthermore, we obtained the restrictions for the total mass production term and formulated the mass exchange rate.

We reformulated the governing equations to their weak forms for the numerical treatment of the coupled system of partial differential equations using the Finite Element Method (FEM). Moreover, we carried out spatial discretisation using the Taylor-Hood elements, where different orders of approximations can be chosen for different primary variables. The implicit Euler integration scheme was used for the time discretisation, which finally gave the discretised system of non-linear equations. This was further implemented in the FE code PANDAS.

In the last part of the thesis, we presented numerical examples to demonstrate the capabilities of the given model for thrombosis in type B Aortic Dissection (AD). Fur-

thermore, chemical, mechanical, and metabolic factors drive the growth process of the thrombus. Due to the need for more detailed knowledge and parameters to quantify the influence of different factors, the model description is even more challenging. However, the effects of the blood velocity and the nutrients on the growth of thrombus are well-researched. Therefore, we present a velocity- and nutrient-concentration-induced growth model.

At first, we introduced the less expensive biphasic model with only solid and fluid phases. Here, velocity-induced growth is introduced, where the mass exchange takes place between the solid and fluid phases. Furthermore, a triphasic model is presented with solid, liquid and nutrient phases, where the mass exchange occurs between the solid and nutrient phases. The growth in the triphasic model depends on the velocity and nutrient concentration. Therefore, we study the influence of the parameters and effects of different Neumann boundary conditions on growth. Finally, we modelled thrombosis using a realistic 2-d cross-section of the false lumen and drew an analogy between the results and the process of thrombosis.

6.2 Outlook

The proposed model provides a reasonable approach for the numerical simulation of thrombosis. The biphasic model is cheaper and considers the effect of velocity on growth in agreement with Virchow triad. Furthermore, it can include high blood pressure, which is known to be the major cause of Aortic Dissection. However, the triphasic model is more detailed. The nutrients play a significant role in thrombosis following the complex chain reactions of the coagulation cascade (clotting factors). Therefore, it is necessary to include nutrients in the modelling approach to obtain a realistic model.

The growth depends on the velocity and nutrient concentration in the triphasic model. We first modelled thrombosis using the triphasic model for an idealised 2-d rectangular geometry and, after that, for a realistic 2-d geometry of the false lumen. Here, we see that the material parameters play an important role in incorporating the physiological factors that can result in thrombosis, according to the Virchow triad. We have an additional parameter to incorporate the factor of inherited or acquired disorders leading to hypercoagulability. The stasis of blood and endothelial injury, along with hypertension, are also incorporated into the model. Moreover, the triphasic model gives the advantage of including the mass exchange between the nutrient and solid phases without altering the amount of liquid which fits well with the physiological understanding of thrombosis. The model also proves its usefulness in actual cases.

However, biological modelling is challenging. Therefore, although extensive theoretical approaches have been used in this monograph, various possible improvements and

extensions are possible to describe thrombosis more accurately. Firstly, the 2-d model can be extended to a 3-d model. Also, blood is considered to be a Newtonian fluid in the presented monograph. However, it is known to be a Non-Newtonian fluid, and this should be included in the model. Additionally, there is a need for medical and experimental data. With enough medical data (CT/MRI scans) taken at different stages of thrombosis, it would be possible to validate the model. Furthermore, there is a need to quantify the different factors responsible for thrombus growth and determine the material parameters from additional experiments. This would also give us more accurate boundary conditions and possibilities to guide the growth process in a much more accurate way. This would also lead to the potential splitting of the mass production formulation into two approaches: primary and secondary hemostasis. These two processes consist of the major part of thrombus formation.

Moreover, the model can be extended to different cases of AD, such as type A AD or false lumen with multiple tears. A larger set of medical and experimental data can aid in developing, validating, and training such models and performing patient-focused simulations. Additionally, because the short-term and long-term diagnosis of AD, especially type B AD, is unclear, all the models for different AD cases can be combined to develop a numerical laboratory and help in decision-making. Furthermore, the model of thrombosis could be extended to conditions where the formation of the blood clot is critical, such as deep venous thrombosis, hypercoagulability disorders and disseminated intravascular coagulation (DIC). Understanding the mechanics of growth in such chronic conditions can open new directions in medical device design, personalised medicine, prognosis, and controlling disease progression.

A APPENDIX

A.1 Derivations of Constituent Balance Relations

In this section, we introduce the constituent balance relations. Following Truesdell's second metaphysical principle, the balance relations can be formulated by considering the interaction effects of the constituents φ^α. Therefore, we introduce the production terms $\hat{(\cdot)}$ to allow such interactions.

A.1.1 Balance of Mass

The balance of mass requires the rate of mass M^α of each constituent φ^α to be equal to the mass supplied. Therefore, the following should hold

$$(M^\alpha)'_\alpha = \int_{\mathcal{B}} \hat{\rho}^\alpha \, \mathrm{d}v, \tag{A.1}$$

where $\hat{\rho}^\alpha$ is the mass supply term. We can evaluate the left side of (A.1) using $(2.18)_2$ as

$$\begin{aligned}(M^\alpha)'_\alpha = \frac{\mathrm{d}_\alpha}{\mathrm{d}t} \int_{\mathcal{B}} \rho^\alpha \, \mathrm{d}v = \int_{\mathcal{B}} (\rho^\alpha J_\alpha)'_\alpha \, \mathrm{d}V_\alpha = \int_{\mathcal{B}} (\rho^\alpha)'_\alpha J_\alpha \, \mathrm{d}V_\alpha + \rho^\alpha \operatorname{div} \mathbf{x}'_\alpha J_\alpha \, \mathrm{d}V_\alpha \\ = \int_{\mathcal{B}} \left[(\rho^\alpha)'_\alpha + \rho^\alpha \operatorname{div} \mathbf{x}'_\alpha \right] \mathrm{d}v,\end{aligned} \tag{A.2}$$

where $(J_\alpha)'_\alpha = J \operatorname{div} \mathbf{x}'_\alpha$. Using (A.1) and (A.2), we get the balance of mass

$$\int_{\mathcal{B}} \left[(\rho^\alpha)'_\alpha + \rho^\alpha \operatorname{div} \mathbf{x}'_\alpha \right] \mathrm{d}v = \int_{\mathcal{B}} \hat{\rho}^\alpha \, \mathrm{d}v. \tag{A.3}$$

On applying the localisation theorem, we obtain the local form of the balance of mass

$$(\rho^\alpha)'_\alpha + \rho^\alpha \operatorname{div} \mathbf{x}'_\alpha = \hat{\rho}^\alpha. \tag{A.4}$$

According to Truesdell's first metaphysical principle, all properties of the mixture must be mathematical consequences of the properties of the constituents. Therefore, we sum the balance of mass of all the constituents φ^α and use Truesdell's third metaphysical principle to get the following constraint

$$\sum_\alpha (\rho^\alpha)'_\alpha + \rho^\alpha \operatorname{div} \mathbf{x}'_\alpha = \sum_\alpha \hat{\rho}^\alpha \stackrel{!}{=} 0. \tag{A.5}$$

Here, $\hat{\rho^\alpha}$ represents the total mass production term, allowing for mass exchange or phase transition among the constituents.

A.1.2 Balance of Momentum

The balance of momentum states that the temporal change of the momentum should be equal to the sum of the forces acting in the vicinity and from a distance, which gives

$$(\mathbf{I}^\alpha)'_\alpha = \int_{\mathcal{B}} \rho^\alpha \mathbf{b}^\alpha \,\mathrm{d}v + \int_{\mathcal{S}} \mathbf{t}^\alpha \,\mathrm{d}a + \int_{\mathcal{B}} \hat{\mathbf{s}}^\alpha \,\mathrm{d}v, \tag{A.6}$$

where $\mathbf{I}^\alpha$ is the momentum of φ^α and $\hat{\mathbf{p}}$ is the total momentum production. Firstly, we evaluate the left side of (A.6) using equations $(2.18)_2$, (A.4), and relation $(J_\alpha)'_\alpha = J \operatorname{div} \mathbf{x}'_\alpha$

$$\begin{aligned}(\mathbf{I}^\alpha)'_\alpha &= \frac{\mathrm{d}_\alpha}{\mathrm{d}t} \int_{\mathcal{B}} \rho^\alpha \mathbf{x}'_\alpha \,\mathrm{d}v = \int_{\mathcal{B}} (\rho^\alpha \mathbf{x}'_\alpha J_\alpha)'_\alpha \,\mathrm{d}V_\alpha \\ &= \int_{\mathcal{B}} \left[(\rho^\alpha)'_\alpha \mathbf{x}'_\alpha J_\alpha + \rho^\alpha \mathbf{x}''_\alpha J_\alpha + \rho^\alpha \mathbf{x}'_\alpha (J_\alpha)'_\alpha \right] \mathrm{d}V_\alpha \\ &= \int_{\mathcal{B}} (\rho^\alpha \mathbf{x}'' + \hat{\rho}^\alpha \mathbf{x}'_\alpha) \,\mathrm{d}v.\end{aligned} \tag{A.7}$$

Furthermore, using (2.57) and converting surface integral into the volume integral, we obtain

$$\int_{\mathcal{S}} \mathbf{t}^\alpha \,\mathrm{d}a = \int_{\mathcal{S}} \mathbf{T}^\alpha \,\mathrm{d}\mathbf{a} = \int_{\mathcal{B}} \operatorname{div} \mathbf{T}^\alpha \,\mathrm{d}v. \tag{A.8}$$

Substituting the equations (A.7) and (A.8) in (A.6), we get the momentum balance

$$\int_{\mathcal{B}} (\rho^\alpha \mathbf{x}''_\alpha + \hat{\rho}^\alpha \mathbf{x}'_\alpha) \,\mathrm{d}v = \int_{\mathcal{B}} (\operatorname{div} \mathbf{T}^\alpha + \rho^\alpha \mathbf{b}^\alpha) \,\mathrm{d}v + \int_{\mathcal{B}} \hat{\mathbf{s}}^\alpha \,\mathrm{d}v, \tag{A.9}$$

which, in the local form, gives

$$\rho^\alpha \mathbf{x}''_\alpha = \operatorname{div} \mathbf{T}^\alpha + \rho^\alpha \mathbf{b}^\alpha - \hat{\rho}^\alpha \mathbf{x}'_\alpha + \hat{\mathbf{s}}^\alpha. \tag{A.10}$$

The summation of the local form of the balance of momentum results in

$$\sum_\alpha \rho^\alpha \mathbf{x}''_\alpha = \sum_\alpha \big[\operatorname{div} \mathbf{T}^\alpha + \rho^\alpha \mathbf{b}^\alpha \underbrace{- \hat{\rho}^\alpha \mathbf{x}'_\alpha + \hat{\mathbf{s}}^\alpha}_{\hat{\mathbf{p}}^\alpha} \big]. \tag{A.11}$$

Here, $\hat{\rho}^\alpha \mathbf{x}'_\alpha$ represents the momentum production due to the mass exchange and $\hat{\mathbf{p}}^\alpha$ results from the interaction force between the constituents and represents the direct momentum production. $\hat{\mathbf{s}}^\alpha$ represents the total momentum production. The local conservation law for one component body leads to the constraint

$$\sum_\alpha \hat{\mathbf{s}}^\alpha \stackrel{!}{=} \mathbf{0}. \tag{A.12}$$

For the slow growth and remodelling processes in biological tissues, $\hat{\rho}^\alpha \mathbf{x}'_\alpha$ can be neglected leading to the constraint

$$\sum_\alpha \hat{\mathbf{p}}^\alpha \stackrel{!}{=} \mathbf{0}. \tag{A.13}$$

A.1.3 Balance of Moment of Momentum

The balance of the moment of momentum states that the temporal change of the moment of momentum should be equal to the sum of moments of all forces acting on the body with respect to the same arbitrary point. For non-polar constituents, it can be written as

$$(\mathbf{h}^\alpha)'_\alpha = \int_{\mathcal{B}} \mathbf{x} \times \rho^\alpha \mathbf{b}^\alpha \, \mathrm{d}v + \int_{\mathcal{S}} \mathbf{x} \times \mathbf{T}^\alpha \, \mathrm{d}\mathbf{a} + \int_{\mathcal{B}} \mathbf{x} \times \hat{\mathbf{p}}^\alpha \, \mathrm{d}v, \tag{A.14}$$

where $\mathbf{h}^\alpha$ is the angular momentum. Firstly, we calculate the material time derivative of $\mathbf{h}^\alpha$ using (A.4)

$$(\mathbf{h}^\alpha)'_\alpha = \frac{\mathrm{d}\alpha}{\mathrm{d}t} \int_{\mathcal{B}} \mathbf{x} \times \rho^\alpha \mathbf{x}'_\alpha \, \mathrm{d}v = \int_{\mathcal{B}} \mathbf{x} \times (\rho^\alpha \mathbf{x}''_\alpha + \hat{\rho}^\alpha \mathbf{x}'_\alpha) \, \mathrm{d}v. \tag{A.15}$$

Combining the equations (A.14) and (A.15), we obtain

$$\int_{\mathcal{B}} \mathbf{x} \times (\rho^\alpha \mathbf{x}''_\alpha + \hat{\rho}^\alpha \mathbf{x}'_\alpha) = \int_{\mathcal{B}} \left[\mathbf{x} \times (\operatorname{div} \mathbf{T}^\alpha + \rho^\alpha \mathbf{b}^\alpha) + \mathbf{I} \times \mathbf{T}^\alpha\right] \mathrm{d}v + \int_{\mathcal{B}} \mathbf{x} \times \hat{\mathbf{p}}^\alpha \, \mathrm{d}v, \tag{A.16}$$

which, in the local form, would give

$$\mathbf{x} \times \left[\operatorname{div} \mathbf{T}^\alpha + \rho^\alpha \mathbf{b}^\alpha - \rho^\alpha \mathbf{x}''_\alpha - \hat{\rho}^\alpha \mathbf{x}'_\alpha + \hat{\mathbf{p}}^\alpha\right] + \mathbf{I} \times \mathbf{T}^\alpha = \mathbf{0}. \tag{A.17}$$

Substituting the balance of momentum (A.10) in the above equation, we obtain

$$\mathbf{I} \times \mathbf{T}^\alpha = \mathbf{0}, \tag{A.18}$$

which is fulfilled if the partial Cauchy stress tensor is symmetric

$$\mathbf{T}^\alpha = (\mathbf{T}^\alpha)^T. \tag{A.19}$$

A.1.4 Balance of Energy

The balance of energy states that the sum of the temporal changes of the internal and kinetic energy should be equal to the sum of the external mechanical and non-mechanical power (First law of thermodynamics), which can be written as

$$\begin{aligned}(W^\alpha)'_\alpha + (Q^\alpha)'_\alpha = &\int_{\mathcal{B}} \mathbf{x}'_\alpha \cdot \rho^\alpha \mathbf{b}^\alpha \, \mathrm{d}v + \int_{\mathcal{S}} \mathbf{x}'_\alpha \cdot \mathbf{T}^\alpha \, \mathrm{d}\mathbf{a} \\ &+ \int_{\mathcal{B}} \rho^\alpha r^\alpha \, \mathrm{d}v + \int_{\mathcal{S}} \mathbf{q}^\alpha \cdot \mathrm{d}\mathbf{a} + \int_{\mathcal{B}} \hat{e}^\alpha \, \mathrm{d}v,\end{aligned} \tag{A.20}$$

where r^α is the mass-specific external heat supply, $\mathbf{q}^\alpha$ is the heat influx, and $\hat{e}^\alpha$ is the total energy production of φ^α. Now, we evaluate the left side of the equation (A.20) and using the mass balance (A.4)

$$\begin{aligned}(W^\alpha)'_\alpha &= \frac{\mathrm{d}_\alpha}{\mathrm{d}t}\int_{\mathcal{B}} \rho^\alpha \varepsilon^\alpha \,\mathrm{d}v = \int_{\mathcal{B}} \left[\rho^\alpha (\varepsilon^\alpha)'_\alpha + \hat{\rho}^\alpha \varepsilon^\alpha\right] \mathrm{d}v,\\ (Q^\alpha)'_\alpha &= \frac{\mathrm{d}_\alpha}{\mathrm{d}t}\int_{\mathcal{B}} \frac{1}{2}\rho^\alpha \mathbf{x}'_\alpha \cdot \mathbf{x}'_\alpha \,\mathrm{d}v = \int_{\mathcal{B}} (\rho^\alpha \mathbf{x}''_\alpha + \frac{1}{2}\hat{\rho}^\alpha \mathbf{x}'_\alpha)\cdot \mathbf{x}'_\alpha \,\mathrm{d}v,\end{aligned} \tag{A.21}$$

where W^α is the internal energy and ε^α is the mass-specific internal energy of φ^α. Q^α is the kinetic energy. Further, by using the relations from Integral theorems, we obtain

$$\begin{aligned}&\int_{\mathcal{B}} \left[\rho^\alpha (\varepsilon^\alpha)'_\alpha + \hat{\rho}^\alpha \varepsilon^\alpha\right] \mathrm{d}v + \int_{\mathcal{B}} (\rho^\alpha \mathbf{x}''_\alpha + \frac{1}{2}\hat{\rho^\alpha \mathbf{x}'_\alpha})\cdot \mathbf{x}'_\alpha \,\mathrm{d}v =\\ &= \int_{\mathcal{B}} \left[(\operatorname{div}\mathbf{T}^\alpha + \rho^\alpha \mathbf{b}^\alpha)\cdot \mathbf{x}'_\alpha + \mathbf{T}^\alpha : \boldsymbol{l}_\alpha\right] \mathrm{d}v + \int_{\mathcal{B}} (\rho^\alpha r^\alpha - \operatorname{div}\mathbf{q}^\alpha)\,\mathrm{d}v + \int_{\mathcal{B}} \hat{e}^\alpha \,\mathrm{d}v,\end{aligned} \tag{A.22}$$

On applying the localisation theorem, we get the local form as

$$\begin{aligned}\rho^\alpha (\varepsilon^\alpha)'_\alpha + \hat{\rho}^\alpha(\varepsilon^\alpha + \frac{1}{2}\mathbf{x}'_\alpha \cdot \mathbf{x}'_\alpha) = \left[\operatorname{div}\mathbf{T}^\alpha + \rho^\alpha(\mathbf{b}^\alpha - \mathbf{x}''_\alpha)\right]\cdot \mathbf{x}'_\alpha +\\ + \mathbf{T}^\alpha : \boldsymbol{l}_\alpha - \operatorname{div}\mathbf{q}^\alpha + \rho^\alpha r^\alpha + \hat{e}^\alpha.\end{aligned} \tag{A.23}$$

Further, we can use the balance of momentum (A.10) to obtain

$$\rho^\alpha(\varepsilon^\alpha)'_\alpha = \mathbf{T}^\alpha : \boldsymbol{l}_\alpha - \operatorname{div}\mathbf{q}^\alpha + \rho^\alpha r^\alpha + \hat{e}^\alpha - \hat{\mathbf{p}}^\alpha \cdot \mathbf{x}'_\alpha - \hat{\rho}^\alpha(\varepsilon^\alpha - \frac{1}{2}\mathbf{x}'_\alpha \cdot \mathbf{x}'_\alpha). \tag{A.24}$$

On summing the equation over all the constituents,

$$\sum_\alpha \left[\rho^\alpha (\varepsilon^\alpha)'_\alpha\right] = \sum_\alpha \big[\mathbf{T}^\alpha : \boldsymbol{l}_\alpha - \operatorname{div}\mathbf{q}^\alpha + \rho^\alpha r^\alpha + \underbrace{\hat{e}^\alpha - \hat{\mathbf{p}}^\alpha \cdot \mathbf{x}'_\alpha - \hat{\rho}^\alpha(\varepsilon^\alpha - \frac{1}{2}\mathbf{x}'_\alpha \cdot \mathbf{x}'_\alpha)}_{\hat{\varepsilon}^\alpha}\big], \tag{A.25}$$

where $\hat{\varepsilon}^\alpha$ is the direct energy production. On comparing with the local energy conservation law of one component body, we get the following constraint for the total energy production

$$\sum_\alpha \hat{e}^\alpha \stackrel{!}{=} 0. \tag{A.26}$$

A.1.5 Entropy Inequality

The entropy balance governs the direction of energy transfer. The entropy principle provides us with the restriction, which plays an essential role in the constitutive modelling of

a material. The entropy inequality states that the temporal change of entropy should be equal to the sum of the external change of entropy and the internal entropy production, and the entropy production is never negative, which is defined as

$$(H^\alpha)'_\alpha \geq \int\limits_{\mathcal{B}} \frac{1}{\Theta^\alpha}\rho^\alpha r^\alpha \,\mathrm{d}v - \int\limits_{\mathcal{S}} \frac{1}{\Theta^\alpha}\mathbf{q}^\alpha \cdot \mathrm{d}\mathbf{a}, \tag{A.27}$$

where H^α is the entropy of φ^α and Θ^α is the absolute Kelvin's temperature of φ^α. Firstly, we calculate the left side of the above equation using the local form of the balance of mass (A.4)

$$\begin{aligned}(H^\alpha)'_\alpha &= \frac{\mathrm{d}_\alpha}{\mathrm{d}t}\int\limits_{\mathcal{B}} \rho^\alpha\eta^\alpha \,\mathrm{d}v = \int\limits_{\mathcal{B}} (\rho^\alpha\eta^\alpha J_\alpha)'_\alpha \,\mathrm{d}V_\alpha \\ &= \int\limits_{\mathcal{B}} (\rho^\alpha)'_\alpha\eta^\alpha \,\mathrm{d}v + \rho^\alpha(\eta^\alpha)'_\alpha \,\mathrm{d}v + \rho^\alpha\eta^\alpha \operatorname{div}\mathbf{x}'_\alpha \,\mathrm{d}v \\ &= \int\limits_{\mathcal{B}} \left[\rho^\alpha(\eta^\alpha)'_\alpha + \hat{\rho}^\alpha\eta^\alpha\right]\mathrm{d}v.\end{aligned} \tag{A.28}$$

We can reformulate (A.27) as

$$\int\limits_{\mathcal{B}} \left[\rho^\alpha(\eta^\alpha)'_\alpha + \hat{\rho}^\alpha\eta^\alpha\right]\mathrm{d}v \geq \int\limits_{\mathcal{B}} \left[\frac{1}{\Theta^\alpha}\rho^\alpha r^\alpha - \operatorname{div}\left(\frac{1}{\Theta^\alpha}\mathbf{q}^\alpha\right)\right]\mathrm{d}v. \tag{A.29}$$

On applying the localisation theorem, we get the local form of entropy inequality

$$\hat{\eta}^\alpha = \rho^\alpha(\eta^\alpha)'_\alpha + \hat{\rho}^\alpha\eta^\alpha + \operatorname{div}\left(\frac{1}{\Theta^\alpha}\mathbf{q}^\alpha\right) - \frac{1}{\Theta^\alpha}\rho^\alpha r^\alpha \geq 0, \tag{A.30}$$

where $\hat{\eta}^\alpha$ is the total entropy production of φ^α. Following this, we use the Legendre transformation between the entropy and its conjugate variable, the temperature and introduce the Helmholtz free energy density ψ^α as

$$\psi^\alpha := \varepsilon^\alpha - \Theta^\alpha\eta^\alpha. \tag{A.31}$$

Furthermore, the lower balance relations of the constituents along with the equation (2.75) gives the Clausius-Duhem representation $\mathcal{D}$ of the entropy inequality

$$\begin{aligned}\mathcal{D} = \sum_\alpha \frac{1}{\Theta^\alpha}\Big\{&\mathbf{T}^\alpha : \mathbf{d}_\alpha - \rho^\alpha\left[(\psi^\alpha)'_\alpha + (\Theta^\alpha)'_\alpha\eta^\alpha\right] - \hat{\mathbf{p}}^\alpha \cdot \mathbf{x}'_\alpha - \\ &- \hat{\rho}^\alpha(\psi^\alpha + \frac{1}{2}\mathbf{x}'_\alpha \cdot \mathbf{x}'_\alpha) - \frac{1}{\Theta^\alpha}\mathbf{q}^\alpha \cdot \operatorname{grad}\Theta^\alpha + \hat{e}^\alpha\Big\} \geq 0.\end{aligned} \tag{A.32}$$

REFERENCES

[1] W. Ehlers, "Vector and tensor calculus: An introduction," *Lecture notes, Institute of Applied Mechanics (Chair of Continuum Mechanics), Universität Stuttgart*, 2017.

[2] J. Bonet and R. D. Wood, *Nonlinear continuum mechanics for finite element analysis*. Cambridge university press, 1997.

[3] G. A. Holzapfel, "Nonlinear solid mechanics: a continuum approach for engineering science," *Meccanica*, vol. 37, pp. 489–490, 2002.

[4] W. Ehlers and J. Bluhm, *Porous media: theory, experiments and numerical applications*. Springer Science Business Media, 2002.

[5] R. de Boer, "Theory of porous media : Highlights in historical development and current state," *Theory of Porous Media*, 2000.

[6] V. Kumar, A. K. Abbas, and J. C. Aster, *Robbins basic pathology e-book*. Elsevier Health Sciences, 2017.

[7] C. G. Harris, B. Croce, and D. H. Tian, "Type b aortic dissection," *Annals of Cardiothoracic Surgery*, vol. 3, p. 339, 2014.

[8] C. A. Nienaber, S. Kische, H. Rousseau, H. Eggebrecht, T. C. Rehders, G. Kundt, A. Glass, D. Scheinert, M. Czerny, T. Kleinfeldt, B. Zipfel, L. Labrousse, R. Fattori, and H. Ince, "Endovascular repair of type b aortic dissection: Long-term results of the randomized investigation of stent grafts in aortic dissection trial," *Circulation: Cardiovascular Interventions*, vol. 6, pp. 407–416, 8 2013.

[9] S. Trimarchi, J. L. Tolenaar, F. H. Jonker, B. Murray, T. T. Tsai, K. A. Eagle, V. Rampoldi, H. J. Verhagen, J. A. V. Herwaarden, F. L. Moll, B. E. Muhs, and J. A. Elefteriades, "Importance of false lumen thrombosis in type b aortic dissection prognosis," *The Journal of thoracic and cardiovascular surgery*, vol. 145, 3 2013.

[10] C. Menichini, Z. Cheng, R. G. Gibbs, and X. Y. Xu, "Predicting false lumen thrombosis in patient-specific models of aortic dissection," *Journal of the Royal Society Interface*, vol. 13, 11 2016.

[11] H. Mohan, *Textbook of pathology*. Jaypee Brothers Medical Publishers, 2018.

[12] A. LaPelusa and H. D. Dave, "Physiology, hemostasis," *StatPearls*, 5 2022.

[13] R. Chaudhry, S. M. Usama, and H. M. Babiker, "Physiology, coagulation pathways," *StatPearls Publishing, Treasure Island (FL)*, 2018.

[14] D. R. Kumar, E. R. Hanlin, I. Glurich, J. J. Mazza, and S. H. Yale, "Virchow's contribution to the understanding of thrombosis and cellular biology," *Clinical Medicine Research*, vol. 8, p. 168, 12 2010.

[15] A. Kushner, D. O. West, and L. S. Pillarisetty, "Virchow triad," *StatPearls Publishing, Treasure Island (FL)*, 2019.

[16] J. Stone, P. Hangge, H. Albadawi, A. Wallace, F. Shamoun, M. G. Knuttien, S. Naidu, and R. Oklu, "Deep vein thrombosis: pathogenesis, diagnosis, and medical management," *Cardiovascular Diagnosis and Therapy*, vol. 7, 2017.

[17] K. J. Cherry and M. D. Dake, "Aortic dissection," *Comprehensive Vascular and Endovascular Surgery*, pp. 517–531, 1 2009.

[18] M. Hibino, Y. Otaki, E. Kobeissi, H. Pan, H. Hibino, H. Taddese, A. Majeed, S. Verma, T. Konta, K. Yamagata, *et al.*, "Blood pressure, hypertension, and the risk of aortic dissection incidence and mortality: results from the j-sch study, the uk biobank study, and a meta-analysis of cohort studies," *Circulation*, vol. 145, pp. 633–644, 2022.

[19] A. Kumar and R. M. Allain, "Aortic dissection," *Critical Care Secrets: Fifth Edition*, pp. 204–211, 2012.

[20] T. T. Tsai, S. Trimarchi, and C. A. Nienaber, "Acute aortic dissection: Perspectives from the international registry of acute aortic dissection (irad)," *European Journal of Vascular and Endovascular Surgery*, vol. 37, pp. 149–159, 2009.

[21] F. Terzi, S. Gianstefani, and R. Fattori, "Type b aortic dissection," *Journal of Cardiovascular Medicine*, vol. 19, 2018.

[22] T. Luebke and J. Brunkwall, "Type b aortic dissection: A review of prognostic factors and meta-analysis of treatment options," *AORTA Journal*, vol. 2, p. 265, 2014.

[23] M. A. Schepens, "Type b aortic dissection: new perspectives," *Journal of visualized surgery*, vol. 4, pp. 75–75, 4 2018.

[24] T. T. Tsai, R. Fattori, S. Trimarchi, E. Isselbacher, T. Myrmel, A. Evangelista, S. Hutchison, U. Sechtem, J. V. Cooper, D. E. Smith, L. Pape, J. Froehlich, A. Raghupathy, J. L. Januzzi, K. A. Eagle, and C. A. Nienaber, "Long-term survival in patients presenting with type b acute aortic dissection," *Circulation*, vol. 114, pp. 2226–2231, 11 2006.

[25] J. I. Fann, J. A. Smith, D. C. Miller, R. S. Mitchell, K. A. Moore, G. Grunkemeier, E. B. Stinson, P. E. Oyer, B. A. Reitz, and N. E. Shumway, "Surgical management of aortic dissection during a 30-year period," *Circulation*, vol. 92, 11 1995.

[26] E. Kuhl, "Growing matter: a review of growth in living systems," *Journal of the Mechanical Behavior of Biomedical Materials*, vol. 29, pp. 529–543, 2014.

[27] L. A. Taber, "Biomechanics of growth, remodeling, and morphogenesis," *Applied Mechanics Reviews*, vol. 48, pp. 487–545, 1995.

[28] Y.-C. Fung and R. Skalak, "Biomechanics. mechanical properties of living tissues," *Journal of Applied Mechanics*, vol. 49, p. 464, 1982.

[29] Y. C. Fung, "Motion, flow, stress and growth," *Biomechanics. Springer–Verlag*, 1990.

[30] J. D. Humphrey, "Continuum biomechanics of soft biological tissues," *Proceedings of the Royal Society of London. Series A: Mathematical, Physical and Engineering Sciences*, vol. 459, pp. 3–46, 2003.

[31] S. C. Cowin and D. Hegedus, "Bone remodeling i : theory of adaptive elasticity," *Journal of Elasticity*, vol. 6, pp. 313–326, 1976.

[32] U. Nackenhorst, "Numerical simulation of stress stimulated bone remodeling," *Technische Mechanik*, vol. 17, pp. 31–40, 1997.

[33] E. Kuhl, A. Menzel, and P. Steinmann, "Computational modeling of growth," *Computational Mechanics*, vol. 32, pp. 71–88, 2003.

[34] E. Kuhl and P. Steinmann, "On spatial and material settings of thermo-hyperelastodynamics for open systems," *Acta Mechanica*, vol. 160, pp. 179–217, 2003.

[35] M. Epstein and G. A. Maugin, "Thermomechanics of volumetric growth in uniform bodies," *International Journal of Plasticity*, vol. 16, pp. 951–978, 2000.

[36] D. Ambrosi and F. Mollica, "On the mechanics of a growing tumor," *International journal of engineering science*, vol. 40, pp. 1297–1316, 2002.

[37] D. Ambrosi and F. Mollica, "The role of stress in the growth of a multicell spheroid," *Journal of mathematical biology*, vol. 48, pp. 477–499, 2004.

[38] S. C. Cowin, "How is a tissue built?," *J. Biomech. Eng.*, vol. 122, pp. 553–569, 2000.

[39] W. Ehlers, "Foundations of multiphasic and porous materials," *Porous Media: Theory, Experiments and Numerical Applications*, pp. 3–86, 2002.

[40] R. Woltmann, *Beyträge zur Hydraulischen Architectur*, vol. 3. bey Johann Christian Dieterich, 1794.

[41] M. A. Biot, "General theory of three-dimensional consolidation," *Journal of Applied Physics*, vol. 12, pp. 155–164, 1941.

[42] G. von Heinrich and K. Desoyer, "Theorie dreidimensionaler Setzungsvorgänge in Tonschichten," *Ingenieur-Archiv*, vol. 30, pp. 225–253, 1961.

[43] R. M. Bowen, *Theory of Mixtures, vol. III*, vol. 3. Academic Press, New York, 1976.

[44] C. Truesdell and R. Toupin, "The classical field theories," *Principles of Classical Mechanics and Field Theory*, pp. 226–858, 1960.

[45] C. Truesdell and W. Noll, *The non-linear field theories of mechanics*, vol. 3. Springer, 2004.

[46] C. Truesdell, *Rational Thermodynamics*, vol. 2. Springer New York, 1984.

[47] R. M. Bowen, "Compressible porous media models by use of the theory of mixtures," *International Journal of Engineering Science*, vol. 20, pp. 697–735, 1 1982.

[48] R. M. Bowen, "Incompressible porous media models by use of the theory of mixtures," *International Journal of Engineering Science*, vol. 18, pp. 1129–1148, 1 1980.

[49] R. D. Boer, *Trends in continuum mechanics of porous media*, vol. 18. Springer Science Business Media, 2005.

[50] R. de Boer and W. Ehlers, "Theory of multicomponent continua and its application to problems of soil mechanics. pt. 1.," 1986.

[51] W. Ehlers, "Constitutive equations for granular materials in geomechanical context," *Continuum Mechanics in Environmental Sciences and Geophysics*, pp. 313–402, 1993.

[52] W. Ehlers and B. Markert, "A linear viscoelastic biphasic model for soft tissues based on the theory of porous media," *Journal of biomechanical engineering*, vol. 123, pp. 418–424, 2001.

[53] A. Wagner and W. Ehlers, "A porous media model to describe the behaviour of brain tissue," *PAMM*, vol. 8, pp. 10201–10202, 2008.

[54] N. Karajan, "Multiphasic intervertebral disc mechanics: theory and application," *Archives of computational methods in engineering*, vol. 19, pp. 261–339, 2012.

[55] T. Ricken, U. Dahmen, O. Dirsch, T. Ricken, and O. Dirsch, "A biphasic model for sinusoidal liver perfusion remodeling after outflow obstruction," *Biomech Model Mechanobiol*, vol. 9, pp. 435–450, 2010.

[56] T. Ricken and J. Bluhm, "Evolutional growth and remodeling in multiphase living tissue," *Computational Materials Science*, vol. 45, pp. 806–811, 5 2009.

[57] T. Ricken, A. Schwarz, and J. Bluhm, "A triphasic model of transversely isotropic biological tissue with applications to stress and biologically induced growth," *Computational Materials Science*, vol. 39, pp. 124–136, 2007.

[58] T. Ricken and J. Bluhm, "Remodeling and growth of living tissue: a multiphase theory," *Arch Appl Mech*, vol. 80, pp. 453–465, 2010.

[59] L. Preziosi and A. Tosin, "Multiphase modelling of tumour growth and extracellular matrix interaction: mathematical tools and applications," *Journal of mathematical biology*, vol. 58, pp. 625–656, 2009.

[60] R. F. Krause, "Growth, modelling and remodelling of biological tissue," 2014.

[61] R. Krause, B. Markert, and W. Ehlers, "A porous media model for the description of adaptive bone remodelling," *PAMM*, vol. 10, pp. 79–80, 2010.

[62] G. A. Ateshian and J. D. Humphrey, "Continuum mixture models of biological growth and remodeling: Past successes and future opportunities," *Annual Review of Biomedical Engineering*, 2012.

[63] D. Ambrosi, M. B. Amar, C. J. Cyron, A. DeSimone, A. Goriely, J. D. Humphrey, and E. Kuhl, "Growth and remodelling of living tissues: perspectives, challenges and opportunities," *Journal of the Royal Society Interface*, vol. 16, 2019.

[64] M. B. Zucker, "Platelet aggregation measured photometric method," *Methods in Enzymology*, vol. 169, pp. 117–133, 1 1989.

[65] I. V. Pivkin, P. D. Richardson, and G. Karniadakis, "Blood flow velocity effects and role of activation delay time on growth and form of platelet thrombi," *Proceedings of the National Academy of Sciences of the United States of America*, vol. 103, p. 17164, 2006.

[66] N. Begent and G. V. Born, "Growth rate in vivo of platelet thrombi, produced by iontophoresis of adp, as a function of mean blood flow velocity," *Nature 1970*, vol. 227, pp. 926–930, 1970.

[67] B. Markert, "Porous media viscoelasticity with application to polymeric foams," *Institut für Mechanik (Bauwesen), Universität Stuttgart*, vol. II-12, 2005.

[68] W. Ehlers, B. Markert, and O. Röhrle, "Computational continuum biomechanics with application to swelling media and growth phenomena," *GAMM-Mitteilungen*, vol. 32, no. 2, pp. 135–156, 2009.

[69] C. Truesdell, "Thermodynamics of diffusion," *Rational thermodynamics*, pp. 219–236, 1984.

[70] B. D. Coleman and W. Noll, "The thermodynamics of elastic materials with heat conduction and viscosity," *The Foundations of Mechanics and Thermodynamics*, pp. 145–156, 1974.

[71] W. Noll, "A mathematical theory of the mechanical behavior of continuous media," *Archive for Rational Mechanics and Analysis 1958*, vol. 2, pp. 197–226, 1958.

[72] W. Noll, "On the continuity of the solid and fluid states," *Journal of Rational Mechanics and Analysis*, vol. 4, pp. 3–81, 8 1955.

[73] C. Truesdell, *A new definition of a fluid*, vol. I. Naval Research Laboratory, 1949.

[74] T. Ricken and J. Bluhm, "Remodeling and growth of living tissue: a multiphase theory," *Archive of Applied Mechanics 2009 80:5*, vol. 80, pp. 453–465, 11 2009.

[75] A. W. Bishop, "The principle of effective stress," *Teknisk Ukeblad*, vol. 39, pp. 859–863, 1959.

[76] R. de Boer and W. Ehlers, "The development of the concept of effective stresses," *Acta Mechanica*, vol. 83, pp. 77–92, 3 1990.

[77] T. Ricken and R. de Boer, "Multiphase flow in a capillary porous medium," *Computational Materials Science*, vol. 28, pp. 704–713, 2003. Twelfth International Workshop on Computational Mechanics of Materials.

[78] A. Atangana, "Principle of groundwater flow," *Fractional Operators with Constant and Variable Order with Application to Geo-Hydrology*, pp. 15–47, 1 2018.

[79] B. Dacorogna, *Direct Methods in the Calculus of Variations*, vol. II. Springer New York, 2007.

[80] T. Ricken, A. Schwarz, and J. Bluhm, "A triphasic theory for growth in biological tissue-basics and applications," *Materialwissenschaft und Werkstofftechnik: Entwicklung, Fertigung, Prüfung, Eigenschaften und Anwendungen technischer Werkstoffe*, vol. 37, pp. 446–456, 2006.

[81] T. D. D. Santos, M. Morlighem, and H. Seroussi, "Assessment of numerical schemes for transient, finite-element ice flow models using issm v4.18," *Geoscientific Model Development*, vol. 14, pp. 2545–2573, 5 2021.

[82] C. Wieners, "Taylor-Hood elements in 3d," *Analysis and Simulation of Multifield Problems*, pp. 189–196, 2003.

[83] H. P. Langtangen and A. Tveito, *Advanced topics in computational partial differential equations: numerical methods and diffpack programming*, vol. 33. Springer Science Business Media, 2012.

[84] F. Brezzi and M. Fortin, *Mixed and hybrid finite element methods*, vol. 15. Springer Science Business Media, 2012.

[85] D. Braess, *Finite elements: Theory, fast solvers, and applications in solid mechanics*. Cambridge University Press, 2007.

[86] C. Taylor and P. Hood, "A numerical solution of the navier-stokes equations using the finite element technique," *Computers and Fluids*, vol. 1, pp. 73–100, 1973.

[87] A. H. Stroud, "Approximate calculation of multiple integrals. prentice-hall series in automatic computation," *Prentice-Hall series in automatic computation*, vol. 1, 1971.

[88] O. C. Zienkiewicz and R. L. Taylor, *The finite element method for solid and structural mechanics*, vol. 6. Elsevier, 2005.

[89] *PANDAS: A coupled FEM solver. https://sciengine.de/index.php*. 2009. Accessed: 2022-11-21.

[90] *CUBIT – Sandia National Laboratories. https://cubit.sandia.gov/.*

[91] C. Menichini and X. Y. Xu, "Mathematical modeling of thrombus formation in idealized models of aortic dissection: initial findings and potential applications," *Journal of mathematical biology*, vol. 73, pp. 1205–1226, 2016.

[92] Z. Cheng, N. B. Wood, R. G. J. Gibbs, and X. Y. Xu, "Geometric and flow features of type b aortic dissection: initial findings and comparison of medically treated and stented cases," *Annals of biomedical engineering*, vol. 43, pp. 177–189, 2015.

[93] T. T. Tsai, A. Evangelista, C. A. Nienaber, T. Myrmel, G. Meinhardt, J. V. Cooper, D. E. Smith, T. Suzuki, R. Fattori, A. Llovet, *et al.*, "Partial thrombosis of the false lumen in patients with acute type b aortic dissection," *New England Journal of Medicine*, vol. 357, pp. 349–359, 2007.

[94] S. B. Ahmed, D. Dillon-Murphy, and C. A. Figueroa, "Computational study of anatomical risk factors in idealized models of type b aortic dissection," *European Journal of Vascular and Endovascular Surgery*, vol. 52, pp. 736–745, 2016.

[95] X. Zheng, A. Yazdani, H. Li, J. D. Humphrey, and G. E. Karniadakis, "A three-dimensional phase-field model for multiscale modeling of thrombus biomechanics in blood vessels," *PLOS Computational Biology*, vol. 16, 4 2020.

[96] J. O. Taylor, K. P. Witmer, T. Neuberger, B. A. Craven, R. S. Meyer, S. Deutsch, and K. B. Manning, "In vitro quantification of time dependent thrombus size using magnetic resonance imaging and computational simulations of thrombus surface shear stresses," *Journal of biomechanical engineering*, vol. 136, p. 71012, 2014.

[97] L. Yang, T. Neuberger, and K. B. Manning, "In vitro real-time magnetic resonance imaging for quantification of thrombosis," *Magnetic Resonance Materials in Physics, Biology and Medicine*, vol. 34, pp. 285–295, 2021.

[98] H. Sönnerlind, "Singularities in finite element models: Dealing with red spots | comsol blog," 2015.

[99] M. L. Williams, "Stress singularities resulting from various boundary conditions in angular corners of plates in extension," *Journal of Applied Mechanics*, pp. 526–528, 1952.

[100] A. Kotousov and Y. T. Lew, "Stress singularities resulting from various boundary conditions in angular corners of plates of arbitrary thickness in extension," *International Journal of Solids and Structures*, vol. 43, pp. 5100–5109, 2006.

[101] K. J. Galvin, A. Linke, L. G. Rebholz, and N. E. Wilson, "Stabilizing poor mass conservation in incompressible flow problems with large irrotational forcing and application to thermal convection," *Computer Methods in Applied Mechanics and Engineering*, vol. 237, pp. 166–176, 2012.

[102] S. Chippada, C. N. Dawson, M. L. Martinez, and M. F. Wheeler, "A projection method for constructing a mass conservative velocity field," *Computer Methods in Applied Mechanics and Engineering*, vol. 157, no. 1-2, pp. 1–10, 1998.

[103] W. Ehlers, S. Zinatbakhsh, and B. Markert, "Stability analysis of finite difference schemes revisited: A study of decoupled solution strategies for coupled multifield problems," *International Journal for Numerical Methods in Engineering*, vol. 94, no. 8, pp. 758–786, 2013.

[104] K. Bäumler, V. Vedula, A. M. Sailer, J. Seo, P. Chiu, G. Mistelbauer, F. P. Chan, M. P. Fischbein, A. L. Marsden, and D. Fleischmann, "Fluid–structure interaction simulations of patient-specific aortic dissection," *Biomechanics and Modeling in Mechanobiology*, vol. 19, pp. 1607–1628, 10 2020.

Monographic Series TU Graz

Computation in Engineering and Science

Vol. 1 Steffen Alvermann

Effective Viscoelastic Behavior of Cellular Auxetic Materials
2008
ISBN 978-3-902465-92-4

Vol. 2 Sendy Fransiscus Tantono

The Mechanical Behaviour of a Soilbag under Vertical Compression
2008
ISBN 978-3-902465-97-9

Vol. 3 Thomas Rüberg

Non-conforming FEM/BEM Coupling in Time Domain
2008
ISBN 978-3-902465-98-6

Vol. 4 Dimitrios E. Kiousis

Biomechanical and Computational Modeling of Atherosclerotic Arteries
2008
ISBN 978-3-85125-023-7

Vol. 5 Lars Kielhorn

A Time-Domain Symmetric Galerkin BEM for Viscoelastodynamics
2009
ISBN 978-3-85125-042-8

Vol. 6 Gerhard Unger

Analysis of Boundary Element Methods for Laplacian Eigenvalue Problems
2009
ISBN 978-3-85125-081-7

Monographic Series TU Graz

Computation in Engineering and Science

Vol. 7 Gerhard Sommer

Mechanical Properties of Healthy and Diseased Human Arteries
2010
ISBN 978-3-85125-111-1

Vol. 8 Mathias Nenning

Infinite Elements for Elasto- and Poroelastodynamics
2010
ISBN 978-3-85125-130-2

Vol. 9 Thanh Xuan Phan

Boundary Element Methods for Boundary Control Problems
2011
ISBN 978-3-85125-149-4

Vol. 10 Loris Nagler

Simulation of Sound Transmission through Poroelastic Plate-like Structures
2011
ISBN 978-3-85125-153-1

Vol. 11 Markus Windisch

Boundary Element Tearing and Interconnecting Methods for Acoustic and Electromagnetic Scattering
2011
ISBN 978-3-85125-152-4

Monographic Series TU Graz

Computation in Engineering and Science

Vol. 12 Christian Walchshofer

Analysis of the Dynamics at the Base of a Lifted Strongly Buoyant Jet Flame Using Direct Numerical Simulation
2011
ISBN 978-3-85125-185-2

Vol. 13 Matthias Messner

Fast Boundary Element Methods in Acoustics
2012
ISBN 978-3-85125-202-6

Vol. 14 Peter Urthaler

Analysis of Boundary Element Methods for Wave Propagation in Porous Media
2012
ISBN 978-3-85125-216-3

Vol. 15 Peng Li

Boundary Element Method for Wave Propagation in Partially Saturated Poroelastic Continua
2012
ISBN 978-3-85125-236-1

Vol. 16 Andreas Jörg Schriefl

Quantification of Collagen Fiber Morphologies in Human Arterial Walls
2013
ISBN 978-3-85125-238-5

Vol. 17 Thomas S. E. Eriksson

Cardiovascular Mechanics
2013
ISBN 978-3-85125-277-4

Monographic Series TU Graz

Computation in Engineering and Science

Vol. 18 Jianhua Tong

Biomechanics of Abdominal Aortic Aneurysms
2013
ISBN 978-3-85125-279-8

Vol. 19 Jonathan Rohleder

Titchmarsh–Weyl Theory and Inverse Problems for Elliptic Differential Operators
2013
ISBN 978-3-85125-283-5

Vol. 20 Martin Neumüller

Space-Time Methods
2013
ISBN 978-3-85125-290-3

Vol. 21 Michael J. Unterberger

Microstructurally-Motivated Constitutive Modeling of Cross-Linked Filamentous Actin Networks
2013
ISBN 978-3-85125-303-0

Vol. 22 Vladimir Lotoreichik

Singular Values and Trace Formulae for Resolvent Power Differences of Self-Adjoint Elliptic Operators
2013
ISBN 978-3-85125-304-7

Vol. 23 Michael Meßner

A Fast Multipole Galerkin Boundary Element Method for the Transient Heat Equation
2014
ISBN 978-3-85125-350-4

Monographic Series TU Graz

Computation in Engineering and Science

Vol. 24 Lorenz Johannes John

Optimal Boundary Control in Energy Spaces
2014
ISBN 978-3-85125-373-3

Vol. 25 Hannah Weisbecker

Softening and Damage Behavior of Human Arteries
2014
ISBN 978-3-85125-370-2

Vol. 26 Bernhard Kager

Efficient Convolution Quadrature based Boundary Element Formulation for Time-Domain Elastodynamics
2015
ISBN 978-3-85125-382-5

Vol. 27 Christoph M. Augustin

Classical and All-floating FETI Methods with Applications to Biomechanical Models
2015
ISBN 978-3-85125-418-1

Vol. 28 Elias Karabelas

Space-Time Discontinuous Galerkin Methods for Cardiac Electromechanics
2016
ISBN 978-3-85125-461-7

Vol. 29 Thomas Traub

A Kernel Interpolation Based Fast Multipole Method for Elastodynamic Problems
2016
ISBN 978-3-85125-465-5

Monographic Series TU Graz

Computation in Engineering and Science

Vol. 30 Matthias Gsell

Mortar Domain Decomposition Methods for Quasilinear Problems and Applications
2017
ISBN 978-3-85125-522-5

Vol. 31 Christian Kühn

Schrödinger operators and singular infinite rank perturbations
2017
ISBN 978-3-85125-551-5

Vol. 32 Michael H. Gfrerer

Vibro-Acoustic Simulation of Poroelastic Shell Structures
2018
ISBN 978-3-85125-573-7

Vol. 33 Markus Holzmann

Spectral Analysis of Transmission and Boundary Value Problems for Dirac Operators
2018
ISBN 978-3-85125-642-0

Vol. 34 Osman Gültekin

Computational Inelasticity of Fibrous Biological Tissues with a Focus on Viscoelasticity, Damage and Rupture
2019
ISBN 978-3-85125-655-0

Monographic Series TU Graz

Computation in Engineering and Science

Vol. 35 Justyna Anna Niestrawska

Experimental and Computational Analyses of Pathological Soft Tissues – Towards a Better Understanding of the Pathogenesis of AAA
2019
ISBN 978-3-85125-678-9

Vol. 36 Marco Zank

Inf-Sup Stable Space-Time Methods for Time-Dependent Partial Differential Equations
2020
ISBN 978-3-85125-721-2

Vol. 37 Christoph Irrenfried

Convective turbulent near wall heat transfer at high Prandtl numbers
2020
ISBN 978-3-85125-724-3

Vol. 38 Christopher Albert

Hamiltonian Theory of Resonant Transport Regimes in Tokamaks with Perturbed Axisymmetry
2020
ISBN 978-3-85125-746-5

Vol. 39 Daniel Christopher Haspinger

Material Modeling and Simulation of Phenomena at the Nano, Micro and Macro Levels in Fibrous Soft Tissues of the Cardiovascular System
2021
ISBN 978-3-85125-802-8

Monographic Series TU Graz

Computation in Engineering and Science

Vol. 40 Markus Alfons Geith

Percutaneous Coronary Intervention
2021
ISBN 978-3-85125-801-1

Vol. 41 Dominik Pölz

Space-Time Boundary Elements for Retarded Potential Integral Equations
2021
ISBN 978-3-85125-811-0

Vol. 42 Douglas Ramalho Queiroz Pacheco

Stable and stabilised finite element methods for incompressible flows of generalised Newtonian fluids
2021
ISBN 978-3-85125-856-1

Vol. 43 Peter Schlosser

Superoscillations and their Schrödinger time evolution
2022
ISBN 978-3-85125-930-8

Vol. 44 Raphael Watschinger

Fast space-time boundary element methods for the heat equation
2023
ISBN 978-3-85125-949-0

Vol. 45 Ishan Gupta

Modelling Growth and Formation of Thrombus: A Multiphasic Approach
2023
ISBN 978-3-85125-964-3